Fakultät für Mathematik, Informatik und Naturwissenschaften | RWTH AACHEN UNIVERSITY

Controlling structural and physical properties of epitaxial transition metal oxide films through oxygen stoichiometry

Von der Fakultät für Mathematik, Informatik und Naturwissenschaften der RWTH Aachen University zur Erlangung des akademischen Grades eines Doktors der Naturwissenschaften genehmigte Dissertation

vorgelegt von

Master of Science

Lei Cao

aus

Daqing, China

Berichter: Univ.-Prof. Dr. rer. nat. Thomas Brückel

Univ.-Prof. Dr. rer. nat. Matthias Wuttig

Tag der mündlichen Prüfung: 19. December 2019

Zusammenfassung

Komplexe Oxide weisen eine Vielfalt von physikalischen Phänomenen auf, wie z.B. Magnetismus, Supraleitung, kollosaler Magnetowiderstand, Ferroelektrizität und darüber hinaus auch Kopplungen zwischen diesen einzelnen Phänomenen. Während der Einfluß der Kationen-Konzentration auf die physikalischen Eigenschaften der komplexen Oxide eingehend untersucht wurde, hat die Sauerstoff-Stöchiometrie als Kontrollparameter für die Eigenschaften, und insbesondere nach der Herstellung der Proben, bis vor kurzem relativ wenig Beachtung gefunden. In dieser Arbeit wurden $La_{0.7}Sr_{0.3}MnO_{3-\delta}$ Schichten mittels Hochdruck-Sauerstoffsputtern bei verschiedenen Sauerstoff-Partialdrücken hergestellt. Es wird der Einfluß der Sauerstoff-Stöchiometrie auf die physikalischen Eigenschaften untersucht. Im Fokus stehen hierbei die magnetischen und elektrischen Transporteigenschaften. Nach der Herstellung der Schichten, wurde mittels eines Postannealing-Prozesses eine Sauerstofffehlstellen-induzierte topotaktische Phasenumwandlung von der ursprünglichen Perowskit- in eine Brownmillerit-Phase erreicht. Die strukturelle Phasenumwandlung wurde hierbei in-situ durch Röntgenbeugung in Realzeit beobachtet. Daraus konnte ein Phasendiagramm, Annealing-Zeit vs. Temperatur, dieser topotaktischen Umwandlung erstellt werden. Es wurde ferner eine neuartige strukturelle Zwischenphase mit einer nicht-zentrosymmetrischen Kristallstruktur gefunden. Mittels polarisierter Neutronenreflektometrie kann in dieser Zwischenphase eine Oberflächenschicht mit stark verringertem nuklearen Streuquerschnitt beobachtet und gleichzeitig die Sauerstoff-Stöchiometrie der gesamten Schicht quantitativ ($La_{0.7}Sr_{0.3}MnO_{2.65}$) bestimmt werden. Die physikalischen Eigenschaften der einzelnen topotaktischen Phasen (ferromagnetisch metallisch bzw. antiferromagnetisch isolierend) können über die Sauerstoff-Absorption bzw. -Desorption reversibel geschaltet werden. Darüber hinaus konnte eine signifikante Verringerung der notwendigen Bedingungen für den Sauerstoff-Absorptionsprozess erzielt werden (Temperaturen unterhalb 100°C sowie Umwandlungszeiten kleiner als 30 min). Somit wurde für jeden Zustand ein eingehendes Verständnis für die Struktur-Eigenschafts-Beziehung in Abhängigkeit des Sauerstoffgehaltes, nicht nur qualitativ sondern auch quantitativ bzgl. der Stöchiometrie,

erarbeitet. Ferner wurde eine in-situ Röntgenbeugungskammer konstruiert, die einen alternativen Zugang zu der exakten Bestimmung des Sauerstoffgehalts in Proben ermöglicht. Die Ergebnisse insgesamt zeigen das technologische Potential auf, welches in der gezielten Kontrolle von Sauerstoff-Fehlstellen in Perowskit-basierten funktionalen Materialien liegt.

Abstract

Complex oxides display a multitude of unique phenomena, such as various forms of magnetism, superconductivity, colossal magnetoresistance, ferroelectricity, and couplings between these states. While the effect of cation concentration on functionalities has been intensely studied, the possibility of tuning the properties through oxygen stoichiometry, in particular after preparation, has received less attention. In this thesis, epitaxial $La_{0.7}Sr_{0.3}MnO_{3-\delta}$ thin films were prepared by High Oxygen Pressure Sputter Deposition at various oxygen partial pressures. The influence of the oxygen stoichiometry onto physical properties is investigated with regard to magnetic and electric properties. After preparation, an oxygen vacancy induced topotactic transition from perovskite to brownmillerite and vice versa is achieved by a post-annealing treatment. Using in-situ X-ray diffraction, the structural evolution is monitored in real-time, and an annealing time vs. temperature phase diagram of the topotactic transformation is constructed. A novel intermediate phase with a non-centered crystal structure is observed for the first time during the topotactic phase conversion which indicates a distinctive transition route. Polarized neutron reflectometry confirms an oxygen deficient interfacial layer with drastically reduced nuclear scattering length density, further enabling a quantitative determination of the oxygen stoichiometry ($La_{0.7}Sr_{0.3}MnO_{2.65}$) for the intermediate state. Associated physical properties of distinct topotactic phases (i.e. ferromagnetic metallic and antiferromagnetic insulating) can be reversibly switched by an oxygen absorption/desorption cycling process. Importantly, a significant lowering of necessary conditions (temperatures below 100 °C and a conversion time less than 30 min) for the oxygen absorption process is found. Thus a comprehensive understanding of the structure-property relationship in dependence of the oxygen content is established at each state not only qualitatively but also at a quantified stoichiometry. In addition, an in-situ x-ray diffraction chamber is constructed to provide an alternative approach for the precise determination of oxygen content variation. These results demonstrate the technological potential of oxygen defect engineering in the design of perovskite-based functional materials.

Content

Chapter 1

Introduction

Oxygen stoichiometry plays a crucial role for the physical functionalities of complex oxides. For instance, the presence of oxygen vacancies can induce a large ionic conductivity, which is related to several practical applications including solid oxide fuel cells, rechargeable batteries, catalysts, and gas sensors [1–5]. Moreover, the migration of oxygen vacancies provides a viable mechanism for the resistance switching characteristics, promoting the emergence of novel resistive switching devices [6–9]. In particular, among multivalent transition metal oxides, the oxygen stoichiometry can alter the valence state of the transition metal, which drastically affects a multitude of intrinsic properties, such as magnetism, superconductivity, magnetoresistance, and multiferroics [10,11]. Due to the profound effect of oxygen deficiency, the study of the dynamics of oxygen vacancies has attracted increasing attention.

A recent development in these studies is the realization of a layered vacancy ordered brownmillerite (BM) structure, which has similar structural framework and topotactic relationship as perovskite (PV) oxides [12–14]. A special feature of this structure type is that it provides additional mechanisms for proton and oxide-ion conduction [15–17]. However, the oxygen stoichiometry of complex oxide thin films is a parameter being hard to determine precisely and to control dynamically. A systematic study on the influence of the variation of oxygen content and the ordering of oxygen vacancies are still lacking. A greater understanding and the manipulation of the interplay between oxygen stoichiometry, lattice structure, and atomic/electronic configurations will not only aid the fundamental understanding of oxygen vacancy physics, but also enable the full potential of functional oxides.

In particular $La_{1-x}Sr_xMnO_3$ (LSMO) exhibits a variety of physical properties such as colossal magnetoresistance, half-metallicity and ferromagnetism above room temperature [18,19]. It is known for its strong coupling between structural properties and

functionalities. It can be considered as a novel system for studying the topotactic phase transition among perovskite-related structures and the effect of oxygen stoichiometry on physical properties.

In this work, epitaxial LSMO thin films were fabricated by High Oxygen Pressure Sputter deposition (HOPSD). An oxygen-vacancy induced topotactic transformation from PV to BM and vice versa is achieved by post-annealing treatments. By means of in situ x-ray diffraction, the structural evolution from PV to BM was directly monitored in real-time. The transition is accompanied by drastic changes in the physical properties from a ferromagnetic metal to an antiferromagnetic insulator. The reverse switching from BM to PV is achieved at remarkably reduced temperatures (<100 °C). In addition, polarized neutron reflectometry was employed to probe the depth profile of both the nuclear and magnetic scattering length density. This approach not only reveals a region with drastically reduced nuclear scattering length density due to oxygen deficiency, but also provides a quantitative analysis of oxygen loss in the film, which is a large step forward to overcome the challenge of precise determination of the oxygen content in oxide thin films.

Outline of the thesis

A short introduction in the theoretical background of the properties of complex oxides is given in Chapter 2. Various types of magnetic interactions and magnetic orders are introduced, followed by the structural variants of perovskite oxides. Since the X-ray and neutron scattering methods are used extensively for the investigation of the LSMO samples, the theoretical basics of scattering theory are described in detail as well. The experimental methods and instruments used for the characterization of the LSMO thin films are described in Chapter 3. The sample preparation and the change of physical properties tuned via oxygen stoichiometry during preparation are discussed in Chapter 4. Chapter 5 focuses on the reversible control of physical properties via the oxygen vacancy-driven topotactic transition during a post-annealing process. Chapter 6 introduces the construction and test of the self-build oxide chamber, which is designed for in-situ measurements attached to a 4-circle X-ray diffractometer. The summary of the main results and an outlook for future research are presented in Chapter 7.

Chapter 2

Theoretical Background

In this chapter the theoretical background on the structure of transition metal oxides and their physical properties is illustrated in detail. First, it starts with an introduction to the magnetic structure, exchange interactions and magnetic anisotropy in perovskite oxides, followed by the film magnetism. Then the description of perovskite structure is extended to deal with more chemically complex phases, in which the materials may contain the ordering of substituted cations or chemical defects. The third and fourth section gives a short overview of growth modes in thin film synthesis and the theory of scattering techniques.

2.1 Magnetism in transition metal oxides

Functional oxides constitute one of the most interesting classes of solid materials, exhibiting a diverse family of structures and rich physics. In particular, transition-metal oxides adopting the perovskite crystal structure (or one of its relatives) have attracted worldwide interest owing to their potential as next-generation nano-, micro-, and macroelectronic materials. Perovskite is a mineral of formula $CaTiO_3$, which was first discovered in 1839 by the Prussian mineralogist Gustav Rose in mineral deposits and named after the Russian mineralogist Count Lev Aleksevich von Petrovski [20,21]. The ideal perovskite structure is cubic and adopted by $SrTiO_3$, as shown in **Figure 2.1**. As with many minerals, perovskite has given its name to a family of compounds called perovskites, with the general chemical stoichiometry of ABO_3. The B-site 3d-transition metal cation with a smaller ionic radius is located at the center of the cubic unit cell, surrounded by an octahedron of oxygen anions. The larger A-site alkaline earth metal or rare earth cations sit at the eight corners of the unit cell. The standard crystallographic description of $SrTiO_3$ is cubic: a = 0.3905 nm; space group: $Pm\bar{3}m$ (No. 221).

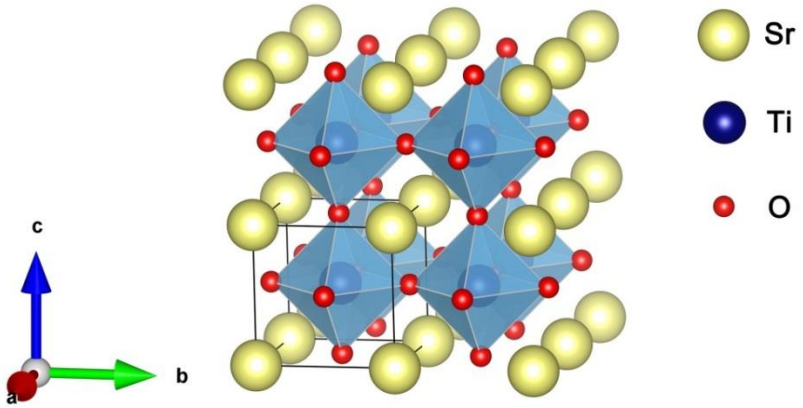

Figure 2.1: Crystal structure of cubic perovskite $SrTiO_3$. The A-sites and B-sites are occupied by Sr and Ti atoms, respectively. The oxygen environment around B-site atoms are denoted with light blue octahedrons, which are characteristic for the perovskite structure. The figure is drawn using the VESTA software [22,23].

The perovskite phases are well known also for their flexibility in terms of A and B cation substitutions. In this case, the conventional view of the ideal perovskites is deviated from the perfect cubic structure due to different effects: i) a cation displacement of A or B -site, ii) a rotation of the surrounding polyhedra around one axis, iii) a deformation of the surrounding polyhedra, iv) a distortion of the entire unit-cell e.g. by elongation in particular directions[3]. **Figure 2.2** shows the unit cell of $La_{0.7}Sr_{0.3}MnO_3$ which crystallizes in the space group $R\bar{3}c$ (No. 167). In $L_{1-x}Sr_xMnO_3$ (L=La, Pr, Sm, Nd, Gd) and $La_{1-x}M_xMnO_3$ (M= Sr, Ca, Ba, Pb) systems which have an A-site or B-site doping element, structural deviations to a rhombohedral phase ($R\bar{3}c$), orthorhombic phase (Pnma), or tetragonal phase (I4/mcm) are observed, but the unit cell can still be described as a pseudocubic unit cell. The corresponding pseudocubic unit cell is depicted within the hexagonal unit cell, as shown at the right hand side of the figure. The distance between two adjacent La atoms in the pseudocubic unit cell is 3.8741(3) Å. The lattice direction [111] in the pseudocubic cell is parallel to the hexagonal c-axis.

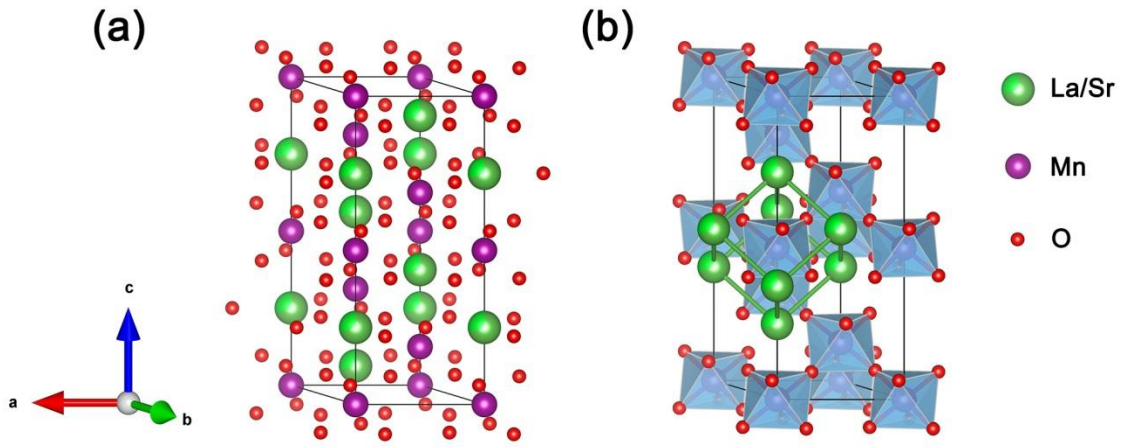

Figure 2.2: Crystal structure of pseudocubic perovskite $La_{0.7}Sr_{0.3}MnO_3$. a) Hexagonal unit cell with symmetry description $R\bar{3}c$ (No. 167). The A-site is occupied by Lanthanum (70%) and Strontium (30%), and the B-site is occupied Manganese. b) Extracted pseudocubic structure with lattice direction [111] in the pseudocubic cell parallel to the hexagonal c-axis. The corresponding oxygen environment around the B-site atoms is denoted with blue octahedrons, which are distorted from the ideal cubic perovskite structure. Both figures are drawn using the VESTA software [22,23].

Moreover, the BO_6 octahedra are the root of many of the intriguing physical properties, such as magnetic and ferroelectric responses to external fields [24–26]. In these materials, the physical properties are often mediated by the electron configurations of the B cations, which themselves are modified by the surrounding six anions. Distinct phenomena and novel functionalities have been discovered in such systems during the past decades [27–29]. Some of the examples of the exotic properties and emergent phenomena are: i) high temperature superconductivity, ii) colossal magnetoresistance, iii) the magnetocaloric effect, iv) metal-insulator-transitions, v) multiferroicity, vi) negative thermal expansion. In this study, we will focus on the electronic and magnetic properties in the following parts.

2.1.1 Electronic structure

Neutral Manganese atoms have an electron configuration of $[Ar]3d^5 4s^2$. The electronic and magnetic properties of the manganites depend on the behavior of the outermost or valence electrons of Mn ions. For an isolated 3d ion, five orbital states are available in a symmetric ligand environment, as shown in **Figure 2.3**.

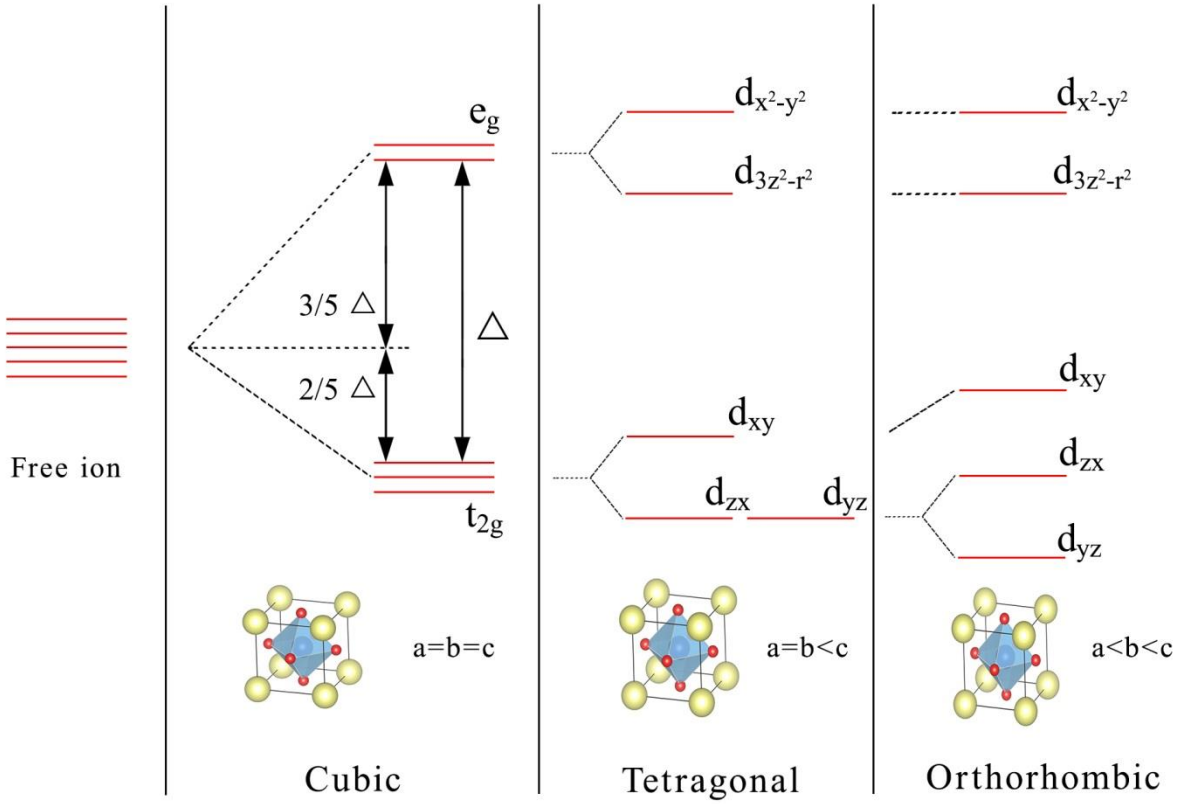

Figure 2.3: Energy levels and orbitals of a 3d-transition metal ion in in a crystal field of cubic, tetragonal, and orthorhombic symmetry. The crystal field and Jahn-Teller effect lead to a splitting of the energy levels.

However in a perovskite crystal, the d-electrons of B-site transition-metal cations experience an electric field created by the oxygen octahedral surrounding. This so-

called crystal field leads to a splitting of the electronic levels as depicted in the second column [30]. For the ideal cubic perovskite structure, the former five d-orbitals are split by the crystal field into two degenerate e_g orbitals (x^2-y^2 and $3z^2$-r^2) at larger energy and three degenerate t_{2g} orbitals (*xy, zx* and *yz*) at lower energy. The separation in energy between e_g and t_{2g} orbitals is the so-called crystal field splitting energy Δ, which depends on the distance between the transition-metal ion and the oxygen ligands. When Δ is large, it is energetically more favourable for electrons to occupy the lower set of orbitals (low-spin state). When Δ is small, it is energetically more favourable for the electrons to occupy both t_{2g} orbitals and e_g orbitals with as many parallel electron spins as possible (high-spin state), according to the Hund's rules. For the manganites, Δ is typically in the range of 2 eV [31].

Moreover, the degeneracy of the e_g and t_{2g} levels is also lifted in some systems due to Jahn–Teller effect. The Jahn–Teller effect can leads to a distortion of the lattice, or fluctuating without any average change of the crystal structure [32]. This is illustrated in the third and fourth column in **Figure 2.3**. The phenomenon is very common in six-fold coordinated complexes (e.g. perovskites with oxygen octahedral coordination). Such complexes are distorted along one of the oxygen octahedral axes, which have the effect of lowering the overall energy. As shown for the case of tetragonal symmetry, the c-axis is elongated and thus the e_g electron levels are further split lowering the energy level of the $3z^2$-r^2 orbital compared to the x^2-y^2 orbital. The Jahn–Teller splitting energy Δ is typically in the range of 0.6 eV. It is a typical demonstration that the electronic and lattice degrees of freedom are strongly coupled. In addition the splitting of the t_{2g} and e_g levels can be supported by strain in the thin films.

In doped manganites such as the $La_{1-x}Sr_xMnO_3$ system, Mn ions have two valence states Mn^{3+} and Mn^{4+} for a stoichiometric sample, with 4 and 3 d-electrons, respectively. According to Hund's first rule and the crystal field splitting energy, the first three d-electrons of the ion will occupy the t_{2g} orbitals while the fourth electron occupy the e_g orbitals. Their ground states according to the usually moderate crystal field splitting are $t_{2g\uparrow}^3 e_{g\uparrow}^1$ and $t_{2g\uparrow}^3$ for Mn^{3+} and Mn^{4+}, respectively.

2.1.2 Exchange interaction

In transition metal oxides, like manganites, the magnetic properties are governed by exchange interactions between the Mn cation spins. These interactions are relatively large between two Mn d-orbitals and mediated by the O p-orbitals which lie in between. The magnetic behavior is then associated with exchange mechanisms which depend on the spin configurations.

Superexchange interaction occurs between two magnetic cations with same valence via an intermediate non-magnetic anion e.g. O^{2-} [33]. This mechanism relates the magnetic pairing between two neighboring cations to the degree of overlap between the relevant orbitals, which is described with the Goodenough–Kanamori–Anderson (GKA) rules [34–36]. As shown in **Figure 2.4**, depending on the Mn d-orbital occupancies and angles between two Mn ions, the magnetic moment alignment can be ferromagnetic or antiferromagnetic. Essentially, the GKA rules indicate that two magnetic cations will have a strong tendency to align in an antiferromagnetic fashion when the orbitals of neighboring cations are all half-filled or empty. The coupling between cations with either a half-filled or filled orbital and one with a vacant orbital can be either antiferromagnetic or ferromagnetic, but generally favors a ferromagnetic alignment. In the case of 90° superexchange, the GKA rules indicate that the magnetic moment alignment is ferromagnetic.

(a)

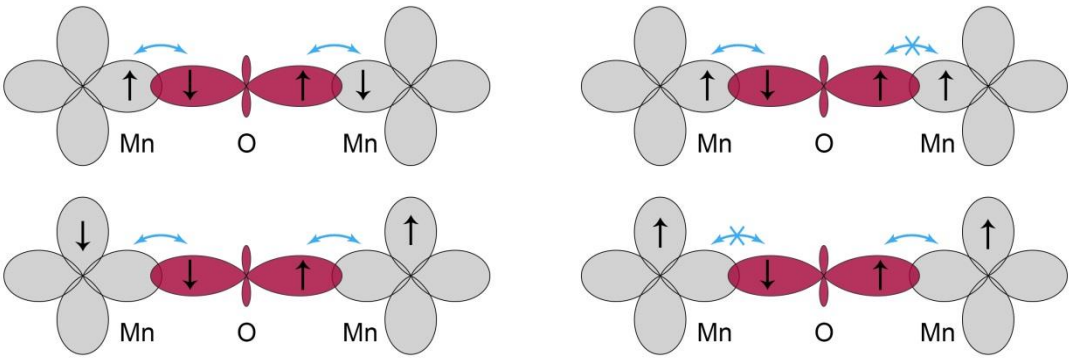

180^0 exchange between half-filled or empty orbitals leads to an antiferromagnetic coupling

(b)

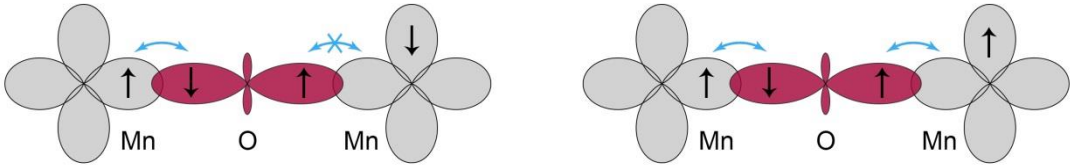

180^0 exchange between half-filled and empty orbitals leads to a ferromagnetic coupling

(c)

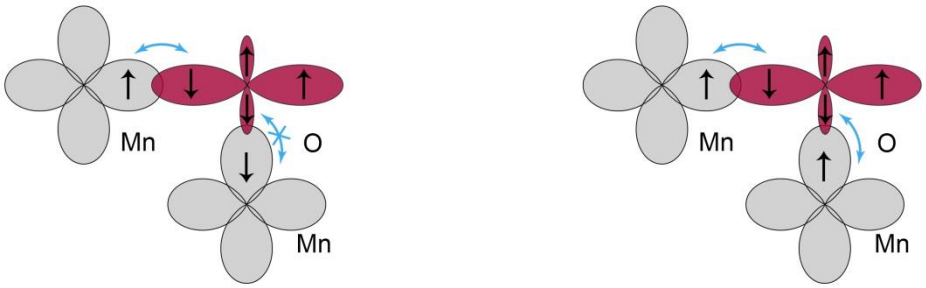

90^0 exchange between half-filled orbitals leads to a ferromagnetic coupling

Figure 2.4: Illustration of superexchange interaction mechanisms between two Mn ions with same valence. (a) shows the GKA-rule 1: antiparallel order of spins is favored between two filled or empty orbitals of Mn ions with 180 ^{0} arrangement, (b) shows the GKA-rule 2: parallel order of spins is favored between one filled orbital and one empty orbital of Mn ions with 180 ^{0} arrangement, (c) shows the GKA-rule 3: parallel order of spins is favored between two filled orbitals of Mn ions with 90^0 arrangement.

The important fact is that superexchange is regarded as a virtual hopping process with no actual charge transfer. A real hopping process between cations and the intermediate anion will cause an increase of Coulomb energy, which cannot be compensated by the kinetic energy.

Double-exchange interaction is another mechanism existing between two magnetic ions with different valences, first proposed by Clarence Zener [37]. In superexchange, the occupancy of the d-shell of the two cations is the same or differs by two, and the electrons are localized. For double exchange, the occupations of the two cations are different, where one cation has an extra electron compared to the other. In this kind of interaction, the electrons are itinerant (delocalized), which results in the material displaying magnetic exchange coupling as well as metallic conductivity. As can be seen in **Figure 2.5**, the Mn e_g electrons can hop between neighboring Mn^{3+} and Mn^{4+} cations via the oxygen anion when their spins are aligned parallel.

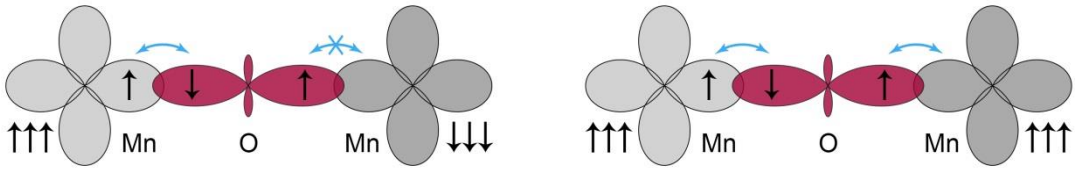

Figure 2.5: Illustration of the double-exchange interaction mechanism between two Mn ions with different valences. Different from the superexchange interaction, the Mn e_g electrons hop between neighboring cations when their spins are parallel.

2.1.3 Magnetic anisotropy

The dependence of magnetic properties on a certain direction of the applied field with respect to the crystal lattice is called magnetic anisotropy [38]. It turns out that depending on the orientation of the applied field one needs a lower (along the easy axis) or higher (along the hard axis) magnetic field to reach the saturation magnetization. In particular, the contribution of the anisotropy energy becomes more significant for low dimensional materials e.g. thin films and nanoparticles [39,40]. In these cases, the magnetic anisotropy strongly affects the shape of hysteresis loops and controls the coercivity and remanence.

There are several types of anisotropy: i) magnetocrystalline anisotropy, ii) shape anisotropy, iii) surface anisotropy, iv) strain anisotropy.

Magnetocrystalline anisotropy arises as a result of the spin-orbit coupling and the orbit-lattice coupling. In the crystal lattice, different orientations of the orbital momentum will give rise to different overlap energies between the wave functions of neighboring moments. Together with spin-orbit interaction, a set of crystallographic directions are energetically more favorable for the magnetic moment. As a consequence, different magnetization curves are observed in the magnetometry measurements along different crystal directions.

For example in cubic crystals, like magnetite, the anisotropy energy density (the ratio E/V) can be written as [38]:

$$\frac{E_{cubic}}{V} = K_1(\alpha^2\beta^2 + \beta^2\gamma^2 + \gamma^2\alpha^2) + K_2\alpha^2\beta^2\gamma^2 \quad (2.1)$$

where spherical polar coordinates are used with $\alpha = \cos\varphi \sin\theta$, $\beta = \sin\varphi \sin\theta$, and $\gamma = \cos\theta$. Here θ and φ are the polar and azimuthal angles between the orientation of the magnetic moment and easy axis, respectively. The easy axes depend on two constants K_1 and K_2, which are so-called the first and second order anisotropy constants, respectively.

Shape anisotropy is encountered when the sample does not have a perfect sphere shape, where the demagnetizing field will not be equal for all directions, thus creating one or more easy axes. The energy of the demagnetizing field is completely determined by an integral of the dipolar energy over the volume V of the magnet:

$$E_{demag} = -\frac{\mu_0}{2}\int \vec{M} \cdot \vec{H}_{dm} dV \quad (2.2)$$

with $\vec{M} = M\ (\alpha_1, \alpha_2, \alpha_3)$ being the magnetization and $\vec{H}_{dm}$ the demagnetization field. μ_0 is the permeability of vacuum. In the case of a single magnetic domain, one can write $\vec{H}_{dm} = -\vec{N} \cdot \vec{M}$, where $\vec{N}$ is the demagnetization tensor with respect to the axes of the coordinate system. For a spherical sample one has:

$$N = \begin{bmatrix} 1/3 & 0 & 0 \\ 0 & 1/3 & 0 \\ 0 & 0 & 1/3 \end{bmatrix} \Rightarrow E_{demag} = \frac{1}{2}\mu_0 M^2 \frac{1}{3}(\alpha_1^2 + \alpha_2^2 + \alpha_3^2) = \frac{1}{6}\mu_0 M^2 \quad (2.3)$$

The demagnetization energy will be isotropic and no dependence on the orientation of the magnetic moment will be found. However for infinitely expanded films and/or very thin films one has:

$$N = \begin{bmatrix} 0 & 0 & 0 \\ 0 & 0 & 0 \\ 0 & 0 & 1 \end{bmatrix} \Rightarrow E_{demag} = \frac{1}{2}\mu_0 M^2 \alpha_3^2 = \frac{1}{2}\mu_0 M^2 cos^2(\theta) \quad (2.4)$$

Here, the demagnetization energy is dependent on the angle θ with the film normal. The energy will be minimized for an angle $\theta = 90°$ i.e. the magnetization lying in the plane of the film. Therefore in thin film systems, shape anisotropy is an important factor and is largely responsible for the in-plane magnetization that is usually observed.

Surface anisotropy is an additional anisotropy created by the reduced symmetry at the surface, firstly pointed out by Néel [41]. Due to broken symmetry at surfaces, the spins have nearest neighboring spins only on one side. Therefore the anisotropy energy contains additional terms in reduced dimensional systems with a large surface. The effective magnetic anisotropy for the thin film can be written as [42,43]:

$$K_{eff} = K_V + \frac{K_{surf}}{t} \quad (2.5)$$

where "K_V" and "K_{surf}" are the bulk anisotropy and surface anisotropy per unit area, respectively. t is the thickness of the thin film. For thick samples, the surface anisotropy is negligible as the thickness term is inversely proportional to the sample thickness. The interfacial/surface anisotropy would exert a strong influence only in the case of ultrathin ferromagnetic layers.

Strain anisotropy is a type of anisotropy related to spin-orbit interaction called magnetostriction. The magnetostriction effect arises from a change of physical distances in the material induced by the change of the orientation of the magnetization. The relative deformation is usually very small, i.e. in the order of 10^{-5} to 10^{-6}. However, if

the stress is sufficient to overcome all the other anisotropies, an easy axis of magnetization can be induced. The corresponding anisotropy energy is expressed as [44]:

$$E_{strain} = K_{\sigma_N} sin^2(\theta) = \frac{3}{2}\lambda_s \sigma_N sin^2(\theta) \quad (2.6)$$

where λ_s is the saturation magnetostriction, and θ is the angle between the measured magnetic moment and the stress σ_N axis. Especially in epitaxial thin films, the strain can persist up to many interlayers.

2.1.4 Order and magnetic structure

In the case of transition-metal oxides with a magnetic element, the compounds can be magnetic and exhibit a rich spectrum of magnetic phases. As an example, in strontium doped lanthanum manganite ($La_{1-x}Sr_xMnO_3$), changes in Sr doping level result in the complex phase diagrams as shown in **Figure 2.6**. As function of the Sr concentration x, this series of compounds e.g. adopt ferromagnetic (FM) or antiferromagnetic (AFM) order depending on the valence states of the manganese ions. Four possible magnetic ordering states for typical perovskites are shown in **Figure 2.7**.

For a Sr doping level x<0.1, an AFM spin state of A-type is adopted at low temperatures. With increasing Sr doping level, a FM phase emerges 0.1<x<0.5. With increasing concentration x, an AFM phase emerges again. Structural, magnetic, and electrical properties were reported by Akimoto et al for stoichiometry x= 0.5 and x=0.54 [45]. For x=0.54, they reported an orthorhombic (Pbnm) nuclear and an A-type AFM structure at 10 K. Similar experimental results were also published by Moritomo et al in the Sr regime (0.5<x<0.6). Furthermore the crystal symmetry changes to pseudotetragonal at x=0.54. For Sr concentrations around x=0.55 a metallic AFM phase with A-type spin structure at low temperatures is observed, followed by a FM metallic state at high temperatures [46]. For the larger Sr concentration regime (0.5<x<0.85), a systematic investigation on single-crystalline $La_{1-x}Sr_xMnO_3$ samples has been carried out by Hemberger et al., and an AFM insulator is established below room temperature [18].

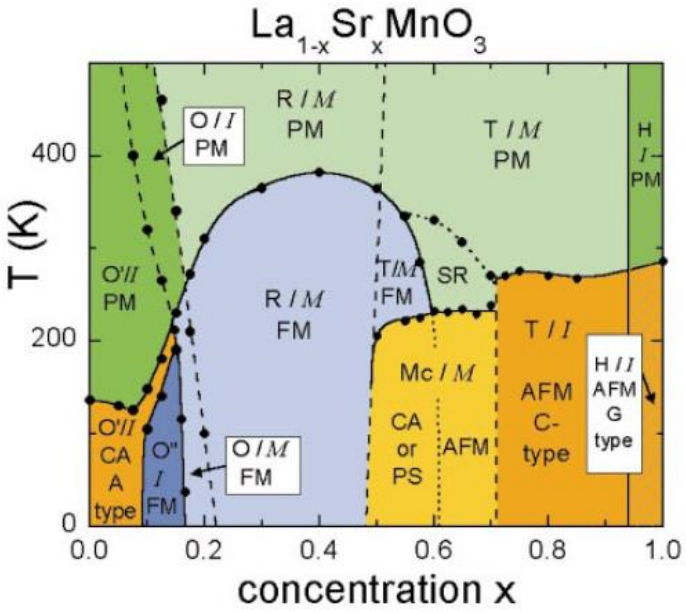

Figure 2.6: Structural, magnetic, and electronic phase diagram of single-crystalline $La_{1-x}Sr_xMnO_3$ reported by Hemberger et al. For the crystal structures: Jahn-Teller distorted orthorhombic, orthorhombic, and orbital-ordered orthorhombic are denoted with O', O, O", respectively. Rhombohedral: R, tetragonal: T, monoclinic: Mc, and hexagonal: H, are indicated as well. For the magnetic structures: paramagnetic: PM (green), shortrange order (SR), canted (CA), A-type antiferromagnetic structure: AFM (yellow), ferromagnetic: FM (blue), phase separated (PS), and AFM C-type structure. For the electronic state: insulating: *I* (dark), metallic: *M* (light). Figure reprinted with permission from [18].

In addition, there are also other mechanisms to mediate the magnetic order and structure in $La_{1-x}Sr_xMnO_3$ systems. Epitaxial lattice strain is one of the most crucial parameters for controlling the physical properties of thin films. Especially, the effects of strain on the properties of perovskite manganites are drastic since the unique physical properties of such strongly correlated systems arise from the complex interactions among the charge, lattice, orbital order and spin. Examples are the often observed strain-induced changes in the various ordering phenomena in complex transition metal oxides: **Figure 2.8** displays the strain versus doping level magnetic phase diagram of

$La_{1-x}Sr_xMnO_3$, reported by Horiba et al. [19]. The magnetic properties of $La_{1-x}Sr_xMnO_3$ thin films are sensitive to tetragonal distortion and the magnetic ground state can be tuned by using different substrates (LAO, LSAT, and STO). At a half doping level, a tensile strain can change the ground state from FM to C-AFI while a compressive strain leads to a change from FM to A-AFM. In this thesis, STO substrates are used and the stoichiometry of $La_{0.7}Sr_{0.3}MnO_3$ is chosen for the further studies. This stoichiometry is far away from the boundary between FM and AFM phases in order to avoid any possible strain-induced magnetic phase transition.

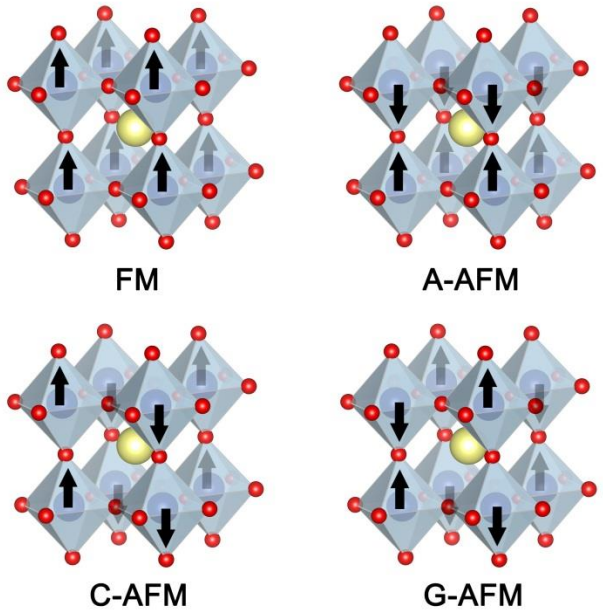

Figure 2.7: a) Four possible magnetic ordering states for typical perovskites, e.g. $La_{1-x}Sr_xMnO_3$: Ferromagnetic ordering (FM), A-type antiferromagnetic ordering (A-AFM), C-type antiferromagnetic ordering (C-AFM) and G-type antiferromagnetic ordering (G-AFM), respectively [47].

Another important aspect is that the concentration and profile of ionic defects is demonstrated to have profound influences onto the physical properties of transition metal oxides. Defect engineering can act as an extra functionality in such complex

oxides systems. The ionic defects—primarily the oxygen vacancies—can radically alter a multitude of intrinsic properties via valence changes or structural phase transitions [48][49]. Examples include pronounced effects of oxygen deficiency on metal-insulator-transitions, emergent phenomena at oxide interfaces and magnetic order [10]. A greater understanding of oxygen vacancies and the dynamic control of the oxygen vacancy behavior in complex oxide nanostructures can open prospects for novel functional oxides-based devices.

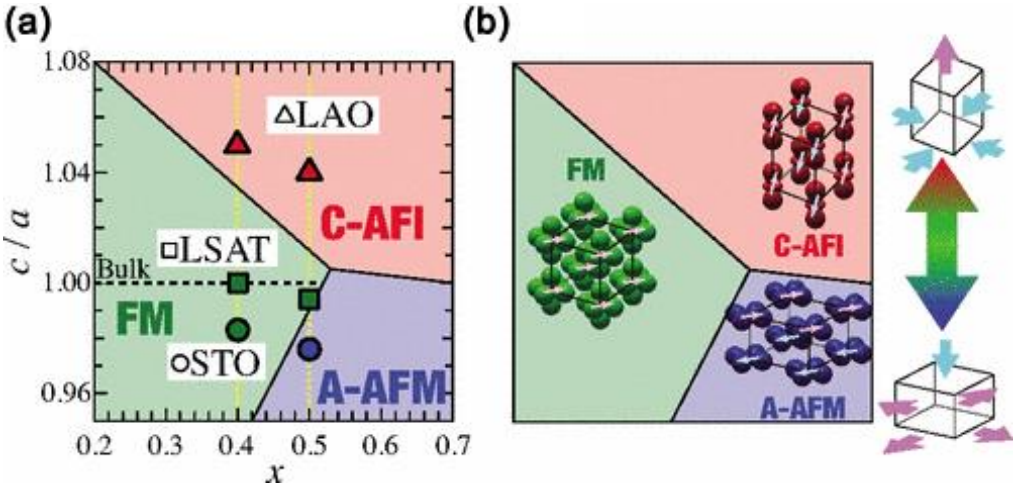

Figure 2.8: a) Phase diagram of LSMO films as a function of the lattice-constant ratio (c/a) and Sr doping level. The triangles, squares, and circles correspond to the Hard X-ray Photoelectron spectroscopy measurement points on LSMO thin films grown on LAO, LSAT, and STO substrates, respectively. b) Schematic illustrations of spin and orbital configurations. FM, C-AFI and A-AFM indicate ferromagnetic ordering, C-type antiferromagnetic ordering with insulating properties and A-type antiferromagnetic ordering with metallic properties, respectively. Figure reprinted with permission from [19].

2.2 ABO_3 Perovskite structure variants

Perovskite phases are well known for their structural flexibility. They also have a big family of structural variants in terms of not only cation and anion substitution, but also chemical defects. In this part, the formula of these perovskite-related structures is not

restricted to a composition of ABO_3. Different perovskite variants will be introduced and discussed in detail.

2.2.1 Anion-Deficient derivatives

The various ordering phenomena within the perovskite framework have attracted the interest of many researchers. The most often encountered ordering pattern is caused by doubly ordered A- and B-site cations, which can be found in $A_2(BB')O_6$ and $AA'_3B_4O_{12}$ type related phases [50]. $A_2(BB')O_6$ is called double perovskites, in which the commonest ordering corresponds to the two different cations, B and B', arranged in a chessboard pattern, often called rock-salt ordering. $AA'_3B_4O_{12}$ provides another example of A-site ordering, where A is an alkali metal, alkaline earth, or lanthanoid, and A′ is a 3d transition metal ion.

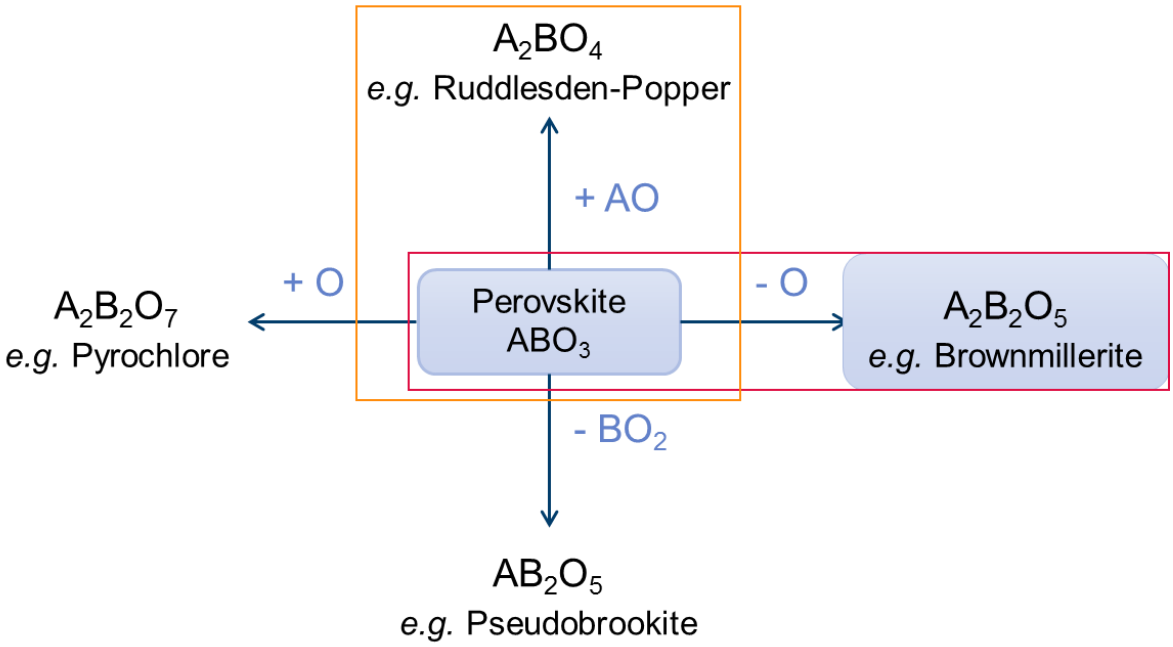

Figure 2.9: Achievable perovskite structure variants by changing the stoichiometry of AO or BO_2 blocks (vertical) and oxygen anions (horizontal).

In recent years, a further kind of ordering originating from the defect structure (e.g. from oxygen vacancies) has attracted intense attention due to remarkable influences onto its properties [51]. **Figure 2.9** displays the relevant perovskite derivatives reachable by changing the oxygen-related stoichiometry. As can be seen from the scheme, by dopping AO blocks, the stoichiometry of perovskites can be changed to an A_2BO_4 type, which has a Ruddlesden-popper phase. If doped with BO_2 blocks, a pseudobrookite structure can be achieved. In another aspect, by excessing or removing oxygen, the oxygen content can be modified, where the pyrochlore structure $A_2B_2O_7$ and the brownmillerite $A_2B_2O_5$ (also written as $ABO_{2.5}$) structure emerge, respectively. In this thesis the reversible transformation between Perovskite and Brownmillerite will be studied systematically.

2.2.2 Brownmillerites

Brownmillerite is a mineral with chemical composition of $Ca_2(Al,Fe)_2O_5$, first recognized in 1932 [50]. **Figure 2.10** shows the crystal structure of brownmillerite in two different viewing directions, projected along [011] and [010], respectively. This kind of structure has a very close relationship to perovskites, which can be viewed as an anion-deficient variant of the ABO_3 cubic perovskite structure. The brownmillerite can be thought of as a perovskite with one-sixth of the oxygen atoms removed from the lattice, resulting in an ordered arrangement of anion vacancies. As viewed along the [010] direction, half amount of the oxygen anions seem removed from alternate oxygen octahedron layers. Each alternating layer of the BO_6 octahedra in a perovskite lattice is transformed into a layer containing only apex-linked BO_4 tetrahedra. In contrast to the perovskite parent, the brownmillerite unit cell is rotated by 45°. This means that the [010] orientation of brownmillerite is parallel to the [011] orientation in the ideal perovskite unit cell. The lattice parameters are related as: $a_{BM} = 4a_{PV}$, $b_{BM} = \sqrt{2}b_{PV}$, $c_{BM} = \sqrt{2}c_{PV}$. In this notation, the surface normal is in the [010] direction.

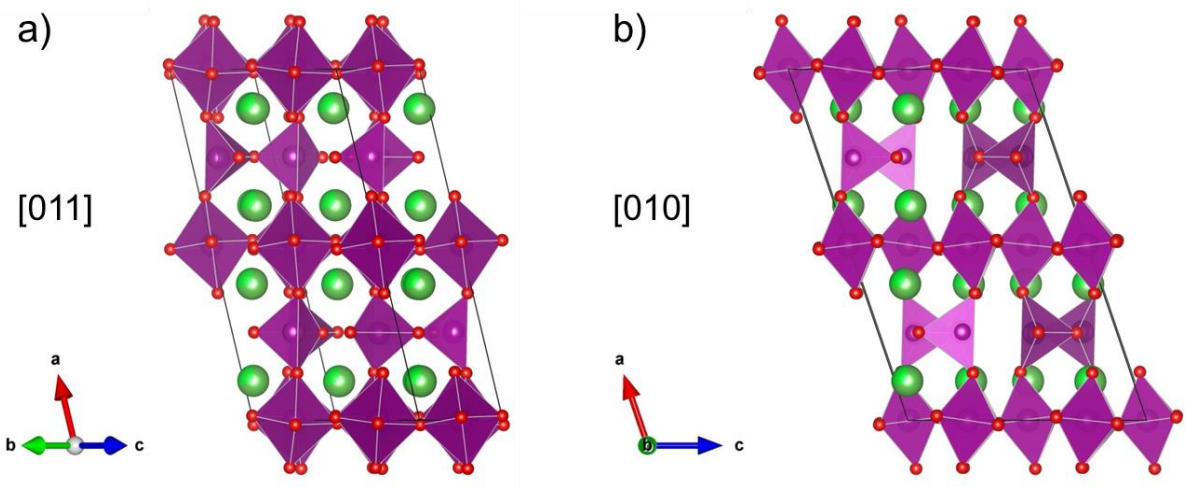

Figure 2.10: Crystal structure of brownmillerite, with (a) view along the [011] lattice direction, and (b) view along the [010] lattice direction. Both figures are drawn using the VESTA software [22,23]

Table 2.1: Oxides with the brownmillerite structure studied in literature

Ferrite	Cobaltite	Manganite	Others
$Ca_2Fe_2O_5$	$Sr_2Co_2O_5$	Ca_2MnAlO_5	Ba_2GaInO_5
$Ca_2Fe_{0.922}Al_{1.078}O_5$	Sr_2CoFeO_5	$Ca_2MnGaO_{5.045}$	$Ba_2In_2O_5$
Ca_2FeCoO_5		Sr_2GaMnO_5	
Ca_2FeMnO_5		$Sr_2Al_{1.07}Mn_{0.93}O_5$	
$Ca_2Fe_{1.5}Mn_{0.5}O_5$		$Ca_{0.5}La_{1.5}Mn_2O_5$	
$Sr_2Fe_2O_5$		$Sr_{0.8}La_{1.2}Mn_2O_5$	
$CaSrFe_{1.5}Mn_{0.5}O_5$		$Ba_{0.4}La_{1.6}Mn_2O_5$	

Many oxides with the brownmillerite structure have been studied so far, as displayed in **Table 2.1**. While most of these systems are reported as polycrystalline bulk samples, only few were grown into the form of thin films (in blue color).

2.2.3 Brownmillerite-related phases

The ideal brownmillerite structure can be represented as a stacking of layers of polyhedra with the sequence …OTOT…, where O stands for a layer containing oxygen octahedra and T for a layer containing oxygen tetrahedral [52]. However, additional oxygen can be accommodated easily if the cation valence permits. Therefore the T layers can be converted to O layers, and vice versa. A different stacking sequence can result and novel brownmillerite-related phases may emerge.

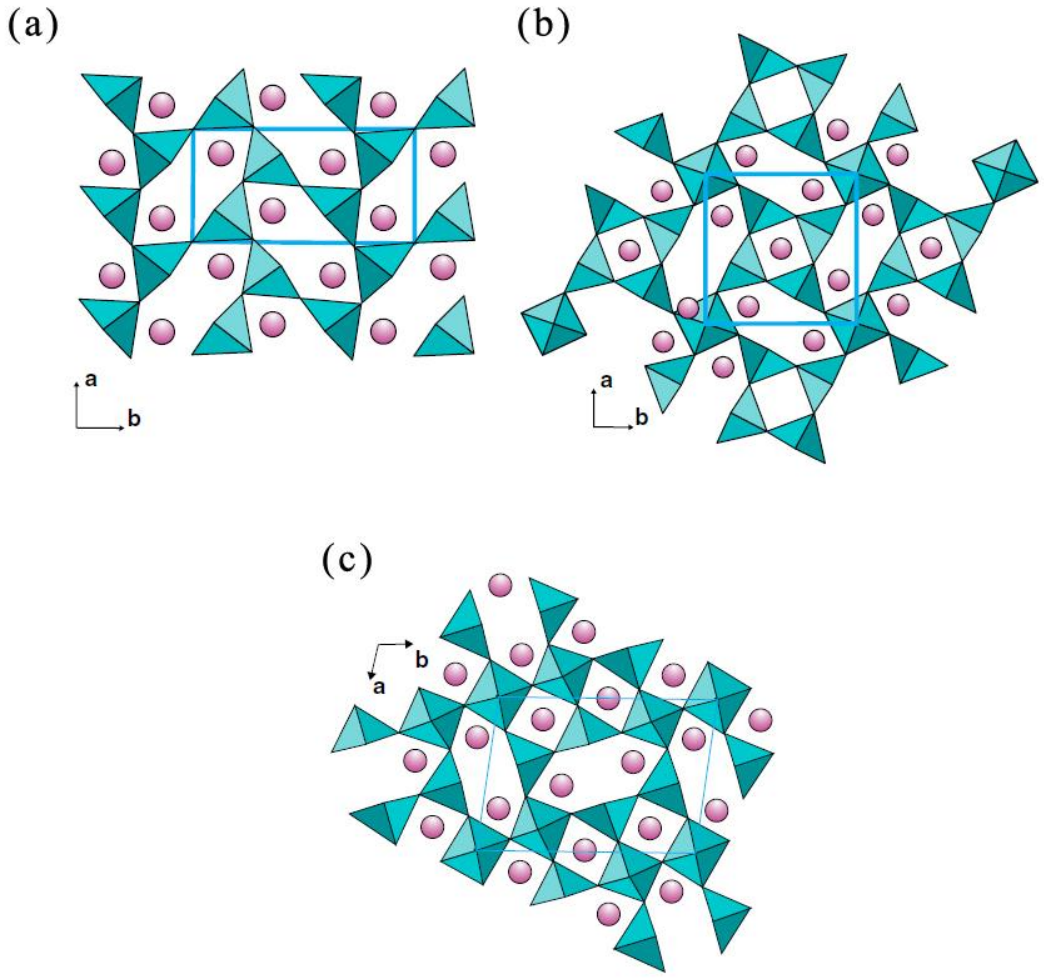

Figure 2.11: Structures of $Sr_{m+4}Mn^{3+}_{4}\ Mn^{4+}_{m}\ O_{10+3m}$ series: (a) $Sr_2Mn_2O_5$; (b) $Sr_5Mn_5O_{13}$; (c) $Sr_7Mn_7O_{19}$, projected along the [001] direction. Taken from [50].

In ferrite and cobaltite, these phases can be written as the series $A_nB_nO_{3n-1}$, of which the brownmillerite structure correspond to $n = 2$ and perovskite to $n = \infty$. Brownmillerite manganites are found in very different structural variants, described as $Sr_{m+4}Mn^{3+}_4 Mn^{4+}_m O_{10+3m}$. Here $Sr_4Mn_4O_{10}$ ($SrMnO_{2.5}$) corresponds to $m = 0$, and $Sr_5Mn_5O_{13}$ and $Sr_7Mn_7O_{19}$ to $m = 1$ and $m = 3$, respectively. The index m also corresponds to the number of apex-linked octahedra, as shown in **Figure 2.11**: (a) no apex-linked octahedra in $Sr_4Mn_4O_{10}$; (b) isolated octahedra in $Sr_5Mn_5O_{13}$; (c) chains of three octahedra in $Sr_7Mn_7O_{19}$. The $m = 2$ compound, $Sr_6Mn_6O_{16}$, with linked pairs of octahedra has not been synthesized yet.

Generally the brownmillerite structure is stable at low temperatures. However, above a certain temperature the oxygen vacancies starts to disorder, with the result that the tetrahedrally coordinated oxygen polyhedra are destroyed and a cubic perovskite with a population of disordered oxygen vacancies will be formed instead.

2.3 Thin film growth

In practical applications, numerous technologies are based on thin film suchs as switches, sensors, or electronic devices [53,54]. Different from bulk, thin films are strongly influenced by the surface and interfaces, defect structures, and strain effects. Therefore in order to explore the physical properties of complex oxides and to apply their functionality to future nano- and micro-electronic devices, the growth of high-quality oxide thin films is required.

2.3.1 Deposition methods

Until now a multitude of deposition techniques have been successfully utilized to grow high-quality thin films. These methods are essentially divided into two groups: Physical vapor deposition (PVD) and chemical vapor deposition (CVD) methods [55,56].

CVD: The basic principle underlying this method is a chemical reaction between volatile precursors from which the film is to be fabricated and suitable gases so as to produce the desired deposition on a substrate (e.g. wafer).

PVD: Here the solid materials are vaporized in a high vacuum environment and deposited onto a substrate. Many methods have been developed to facilitate the transfer of atoms from a solid source onto a substrate. Evaporation and sputtering are the two most commonly used PVD methods. In this study the sputtering deposition method is used, which will be introduced in detail in the next chapter.

2.3.2 Growth mode

The formation of thin films occurs in several steps: i) from vapor to adatoms (adsorption), ii) surface diffusion, iii) chemical bond formation (chemisorption), iv) nucleation: aggregation of single atoms/molecules, v) microstructure formation (amorphous, polycrystalline, or single-crystalline, defects, roughness, etc.). vi) changes within the bulk of the film, e.g. interdiffusion, grain growth. Depending on the intrinsic interaction between incoming clusters of molecules, adatoms, and the condition of the substrate surface, three different growth modes can be formed, as illustrated in **Figure 2.12**. As the thin film deposition is a non-equilibrium kinetic process, a minimization of surface energy is attained. The modes of film formation are determined by the interplay of three surface energies involved in the process, which includes the substrate surface free energy (γ_s), the film surface free energy (γ_f), and the substrate/film interface free energy (γ_i). The adopted growth mode largely determines the eventual structure of the film [56,57].

a) **Frank-van der Merwe mode**: Layer-by-layer growth

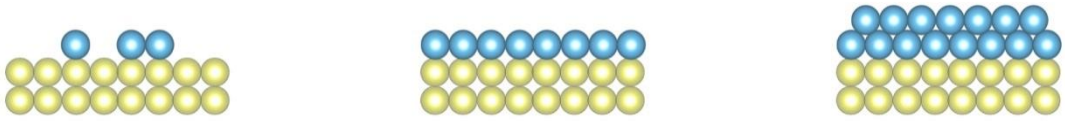

b) **Vollmer-Weber mode**: island growth

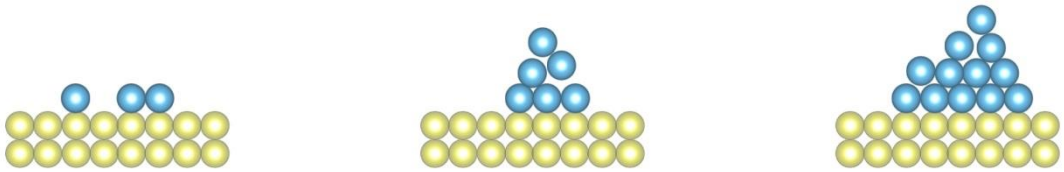

c) **Stranski-Krastanov mode**: Layer-by-layer followed by island growth

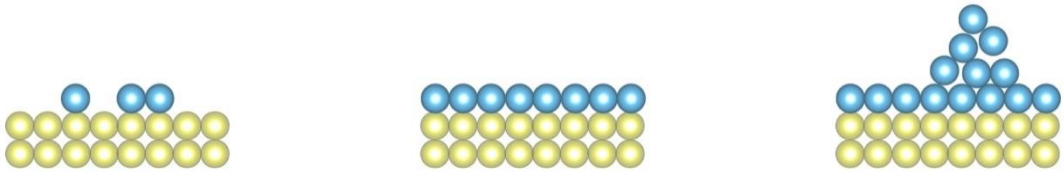

Figure 2.12: Sketch of different epitaxial growth modes for thin films. (a) Frank-Van der Merwe mode (2D), (b) Volmer-Weber mode (3D), (c) Stranski – Krastanov mode (2D + 3D).

If $\gamma_i + \gamma_f < \gamma_s$, film atoms are more strongly bound to the substrate than to each other and a fast diffusion might take place. 2D layered growth is observed and a smooth film will form. For the opposite case, $\gamma_i + \gamma_f > \gamma_s$, the interactions between adatoms-to-adatoms overcome the adatoms-substrate interactions. Then the most energetically favorable condition leads to the formation of 3D islands on the surface of the substrate. In this mode, the material piles up to minimize the interface with the substrate, resulting in rough film surfaces or even to isolated islands. In other cases, a mixed growth is found, as shown in the Stranski-Krastanov mode. This mode is an intermediate process where the film grows layer by layer initially and then changes to island growth after few

monolayers. The initial layer is strained to match the substrate, while the strain becomes relaxed at a critical thickness. In the ideal deposition of a thin film, the layer-by-layer mode is desired to obtain a smooth surface, a homogeneous structure, and a lower density of defects. To achieve this goal, one needs to optimize the growth parameters.

2.4 Scattering theory

Scattering is a non-destructive technique to characterize the structural and often also the magnetic properties of materials. In this thesis, X-rays, neutrons, and electrons are used as probes to investigate the structure of the complex oxide thin film systems. In this section, the basic principles of scattering will be introduced, especially focusing on diffractometry and refectometry. For a complete understanding of the scattering theory please refer to [58,59].

2.4.1 Basics of scattering

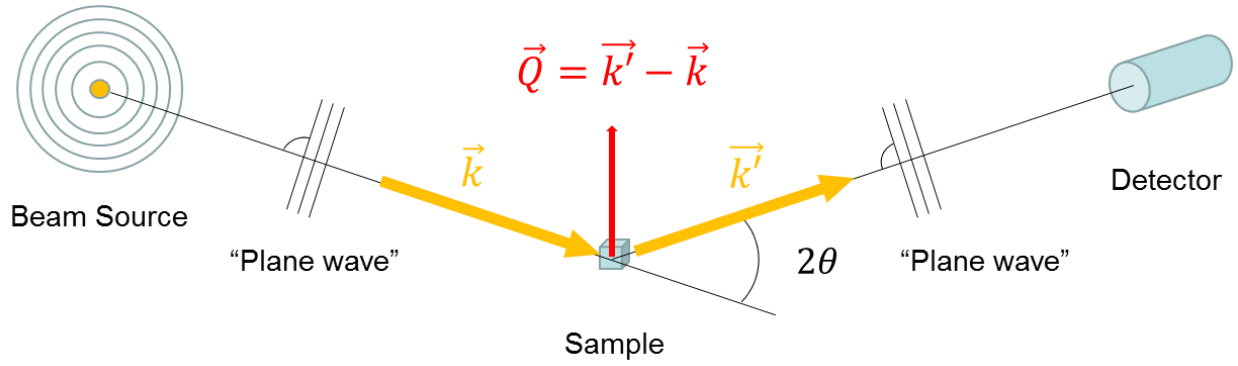

Figure 2.13: A sketch of the scattering process in the Fraunhofer approximation, as adapted from [58]. It is assumed that the incident beam is a plane wave and the size of the sample is much smaller compared to the distance from the source to the sample and the distance from the sample to detector, respectively.

In this thesis, the scattering events are discussed within the restriction of elastic scattering, where the so-called Fraunhofer approximation is assumed. **Figure 2.13** displays a schematic representation of an elastic scattering experiment. The incident and scattered beam can be described by the wave vectors $\vec{k}$ and $\vec{k'}$, respectively. Thus the length of the scattering vector $\vec{Q} = \vec{k'} - \vec{k}$ can be written as:

$$Q = |\vec{Q}| = \sqrt{\left(\vec{k'} - \vec{k}\right)^2} = \sqrt{2k^2\left(1 - cos(2\theta)\right)} = \frac{4\pi}{\lambda} sin(\theta) \qquad (2.7)$$

where $= |\vec{k}| = |\vec{k'}| = \frac{2\pi}{\lambda}$ for an elastic scattering process.

The scattered intensity is than measured by a detector which covers the solid angle $\mathrm{d}\Omega = dS/r^2$, where dS is the detector area and r is the distance to the detector. **Figure 2.14** shows the definition of the scattering cross-section in a scattering event.

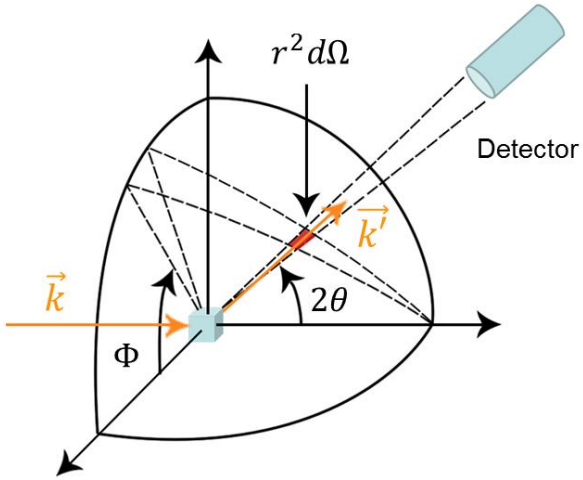

Figure 2.14: Geometry to derive the scattering cross-section. Adapted from [58].

The differential cross section is proportional to the probability that a particle is scattered into the solid angle $\mathrm{d}\Omega$ after interaction with the sample, which is given by:

$$\frac{d\sigma}{d\Omega} = \frac{dn}{Jd\Omega} \tag{2.8}$$

Here dn is the number of detected particles and J is number of incident particles.

In a microscopic view, quantum mechanics is needed for the calculation of the differential cross-section. By solving the Schrödinger's equation within the elastic scattering regime, the total scattering amplitude is given by:

$$A(\vec{Q}) \sim A_0 \cdot \int \rho_s(\vec{r}) \cdot e^{i\vec{Q}\cdot\vec{r}} d^3\vec{r} \tag{2.9}$$

Here A_0 denotes the amplitude of the incident wave field. The scattering amplitude is connected with the scattering density $\rho_s(\vec{r})$ by a Fourier transform. Since the probability to find a particle in the defined volume is given by the absolute square of the probability amplitude, the differential cross-section can be thus expressed as the square of the amplitude of the scattered wave. However, technically only the scattered intensity $I(\vec{Q})$ can be measured in a scattering experiment instead of the amplitude.

$$I(\vec{Q}) \sim \left|A(\vec{Q})\right|^2 \tag{2.10}$$

Therefore the phase information is lost and a back-transformation to obtain the scattering potential is not possible. This is the so-called “phase problem of scattering”. But one can refer to the structure refinement method, by which the created structure model is iteratively improved to obtain an optimum match between a simulation and the measured data. Thus more structural information can be extracted.

2.4.2 Diffractometry

X-ray radiation and moderated neutrons have a wavelength in the range of the typical distances between atoms. Therefore they can be used to probe crystal structures. When plane waves with a wavelength λ are scattered at an atomic periodic structure, interference of reflected waves will occur. If the so-called Bragg’s law is satisfied at

certain angles, constructive interference patterns can be observed. The Bragg's equation is hereby:

$$n \cdot \lambda = 2d \cdot sin(\theta) \tag{2.11}$$

with d being the interplanar spacing and θ the scattering angle.

In reciprocal space, the Bragg's equation is equivalent to the well-known Laue condition. The formulation of the Laue condition can be expressed as:

$$\vec{Q} = \vec{G} \tag{2.12}$$

Here $\vec{G}$ is the reciprocal lattice vector with $|\vec{G}| = \frac{2\pi}{d_{hkl}}$. By measuring the positions of Bragg reflections, the lattice parameters can be deduced.

2.4.3 Reflectometry

A reflectometry measurement is a surface-sensitive analytical technique used for the characterization of thin film systems. Such a measurement can provide information on thickness, roughness and other interfacial properties on the nanometer scale.

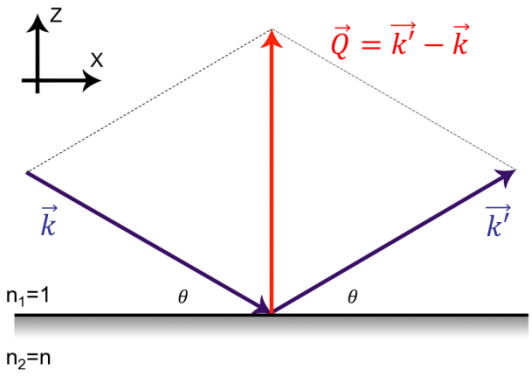

Figure 2.15: Scattering geometry of a typical reflectometry experiment.

A typical scattering geometry is shown in **Figure 2.15**, where a grazing incident beam of x-rays or neutrons is reflected from a flat surface of the film and the intensity of the outgoing beam in the specular direction is measured. Here the scattering potential is described within the continuum approximation. In analogy to classical optics, we can derive the reflection and transmission coefficients R and T by solving the wave function for a one dimensional step potential. At a flat interface, the reflection and the refraction can be written as [60]:

$$R = \left|\frac{\theta - n\theta_t}{\theta + n\theta_t}\right|^2 \tag{2.13}$$

$$T = \left|\frac{2\theta}{\theta + n\theta_t}\right|^2 \tag{2.14}$$

where n is the index of refraction of the thin film and the angle of transmitted beam is θ_t. For most materials, $n < 1$ is fulfilled for X-ray and neutron radiation, resulting in total reflection. For angles of incidence below the so-called critical angle θ_c, the incoming beam is reflected completely. The critical angle θ_c, for the case of x-ray or neutron scattering, can be written as [61]:

$$\theta_c = arcsin\left(\frac{1}{n}\right), \qquad \theta_c \simeq \lambda\sqrt{\frac{\rho}{\pi}} \tag{2.15}$$

where is the wavelength λ of the beam and ρ is the electron density for x-rays or scattering length density (SLD) for neutrons. Thus the higher the ρ of a material the higher the critical angle θ_c.

For angles of incidence above θ_c, the beam can be transmitted into the sample and the intensity of the reflected beam drops off approximately with Q^{-4} for an ideal flat surface, which is usually referred to as Fresnel reflectivity. However, the decay of the reflectivity from a thin layer is qualitatively different as it shows oscillations of period: $\Delta Q = 2\pi/d$, where d is the thickness of the thin film. This is attributed to the interference of waves scattered from the surface and from the interface to the substrate. These interference

fringes are referred to as “Kiessig fringes”. By measuring the separation of the maxima ΔQ at larger Q range, the film thickness can be determined using $d = 2\pi/\Delta Q$.

In reality, the surface and interfaces exhibit roughness on an atomic scale of a few nanometers which leads to diffuse scattering of the incident beam. Such effect decreases the intensity of the specular reflected beam dependently. Therefore the reflectometry measurement is also highly sensitive to roughness. For a rough surface, a strong damping with Q will be observed in reflectivity curve. For a layered system, the calculation of the reflection and transmission has to be considered at each interface. If the interface is rough, the reflected intensity drops off drastically with increasing incident angle. As a result, the amplitudes of the fringes are damped. Therefore the reflectometry technique is also used to determine both the surface and interface roughnesses.

2.4.4 Polarized neutron reflectometry

Neutrons provide a different contrast between elements compared to X-rays, as neutrons interact with the nuclei while X-rays interact with the electron clouds. Thus in neutron reflectometry, the scattering length density (SLD) is determined in contrast to the electron density measured by X-ray reflectometry. In addition, neutrons are also sensitive to the magnetization in the sample. Using polarized neutrons, magnetic as well as chemical profiles can both be probed. Due to the Zeeman interaction of the magnetic moment of the neutrons with the magnetic induction of the sample, an additional term for the scattering potential from the magnetic contribution has to be added. The interaction potential for neutrons can be thus described as [58]:

$$V(\vec{r}) = \frac{2\pi\hbar^2}{m_N}\rho_N b - \gamma_n \mu_N \vec{\sigma} \cdot \vec{B} \tag{2.16}$$

The first term corresponds to the nuclear potential, where ρ_N is nuclear number density and b is the scattering length. The second term represents the magnetic part of the scattering potential with the gyromagnetic factor for neutrons ($\gamma_n = -1.913$). $\vec{B}$ denotes

the magnetic induction field and μ_N is the nuclear magneton. $\vec{\sigma} = \{\hat{\sigma}_x, \hat{\sigma}_y, \hat{\sigma}_z\}$ is the spin operator which consists of Pauli-matrices.

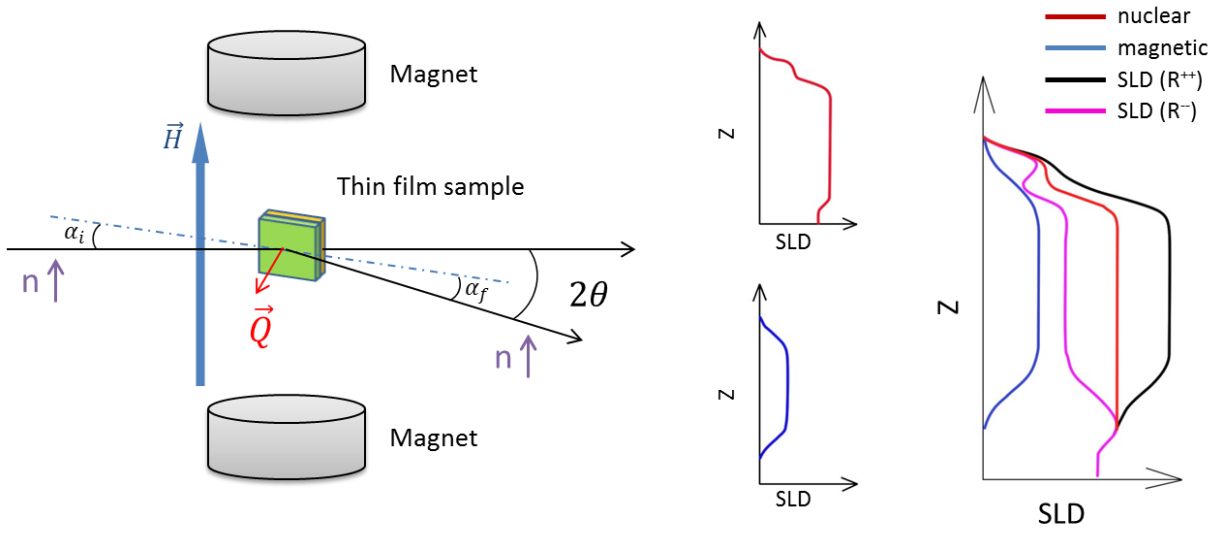

Figure 2.16: Scattering geometry for a neutron reflectometry experiment and the SLD for spin-up neutrons and spin-down neutrons in an example film system. The SLD is composed of a nuclear and a magnetic part.

A typical geometry of a polarized neutron reflectometry (PNR) measurement can be seen in **Figure 2.16** (left). PNR is very sensitive to magnetic structures because the nuclear and magnetic SLDs are of the same order of magnitude. A diagram of the SLD is shown in **Figure 2.16** (right). In the measurement, the neutron beam is polarized parallel or anti-parallel to the quantization axis along the external magnetic field $\vec{H}$. Here we describe the polarized neutron beam with two spin components $\psi_+(\vec{r})$ and $\psi_-(\vec{r})$ for "spin-up" and "spin-down" polarization with respect to the quantization axis. Thus the three dimensional Schrödinger equation can be expressed with the neutron wave function:

$$\psi_+''(z) + \left[k_z^2 - 4\pi b\rho_N + \frac{2m\gamma_n\mu_n}{\hbar^2}B_\parallel\right]\psi_+(z) + \frac{2m\gamma_n\mu_n}{\hbar^2}B_\perp\psi_-(z) = 0 \qquad (2.17)$$

$$\psi_-''(z) + \left[k_z^2 - 4\pi b\rho_N - \frac{2m\gamma_n\mu_n}{\hbar^2}B_\parallel\right]\psi_-(z) + \frac{2m\gamma_n\mu_n}{\hbar^2}B_\perp\psi_+(z) = 0 \qquad (2.18)$$

where $B_\parallel$ and $B_\perp$are the magnetic fields of the sample parallel and perpendicular to the neutron guide field, respectively. Both of them are perpendicular to the scattering vector $\vec{Q}$. For the magnetization component $B_\parallel$, the differential equations shown above are decoupled, which leads to nuclear and magnetic scattered intensities observed only in the so called non-spin-flip channels. In detail, the spin-up (R^{++}) channel shows the sum of both the nuclear and the magnetic contribution, while the spin-down (R^{--}) channel shows the difference of the nuclear and the magnetic contribution. For the magnetization component $B_\perp$, if $B_\perp \neq 0$, the above equations will not be decoupled and thus a spin-flip event occurs. In the spin-flip channels, pure magnetic information is contained and corresponding signals can be observed. Therefore PNR can act as a vector magnetometer and is able to study the magnetic depth profile in a layered system.

Chapter 3

Experimental Methods and Instruments

In this chapter the methods and instruments used for sample preparation and characterization are introduced. High oxygen pressure sputter deposition (HOPSD) was used to grow the thin film samples, given in section 3.1. The structural and physical properties of the samples were determined by various in-house characterization methods (described in section 3.2-3.8), and by large scale facility instruments (described in section 3.9).

3.1 High Oxygen Pressure Sputter Deposition (HOPSD)

Epitaxial $La_{0.7}Sr_{0.3}MnO_{3-\delta}$ thin films were grown on atomically flat $SrTiO_3$ single-crystalline substrates by High Oxygen Pressure Sputter Deposition (HOPSD) [62]. Sputtering is a technique frequently used for thin film deposition in research and industry. The sketch of the used sputter device is shown in **Figure 3.1**. In our study, the HOPSD technique is used, where the oxygen partial pressure during the sputtering process lies in the range of 1~3 mbar. By applying a radio frequency electric field (13.6 MHz) on a sputter target, an oxygen plasma is created between the target and substrate electrode, where atoms are ejected from the target material by the bombardment of ionized atoms from the sputtering gas. The target material will be then deposited onto the substrate.

In contrast to the common sputtering technique which operates at low pressures in the range of 10^{-3} to 10^{-6} mbar, the sputtered material has a very short mean free path for HOPSD, resulting in the localization of the plasma. The localized plasma will suppress the backsputtering effect from the already deposited material. Such effect highly depends on the pressure and the target-to-sample distance. Therefore a distance of 2-4

cm between target and substrate was adjusted in our case to optimize the film growth. Additionally, the high oxygen pressure minimizes an oxygen deficiency.

Further growth parameters will also influence the crystal quality of the thin film, e.g. the growth temperature, medium gas pressure and applied power. In our sputtering device, the substrate heater stage enables a maximum temperature of 1000 °C. The oxygen partial pressure can be tuned between 0.5 mbar to 3 mbar by a mass flow controller (MFC). A maximum power of 200 W can be applied between the target and the substrate. Here a fixed stoichiometry of the target is used to achieve a fast and reproducible film growth.

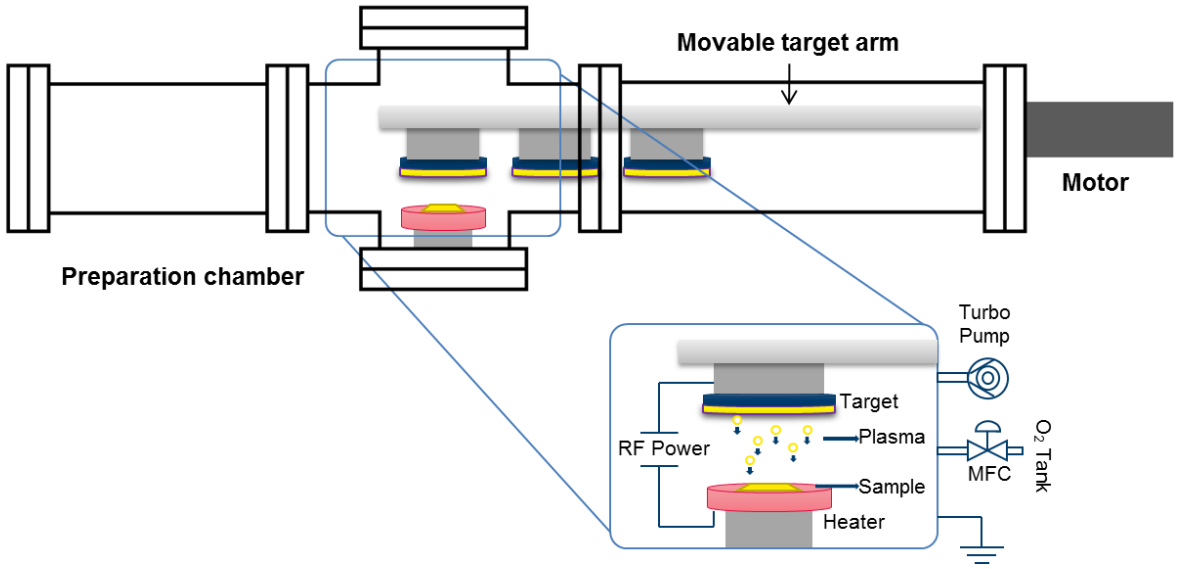

Figure 3.1: Sketch of the high oxygen pressure sputter deposition device. Several targets can be switched with a movable target arm to grow multilayer systems. The typical target size is 5 cm, where the distance between substrate and target is 2 cm. The zoom-in shows a detailed view of a sputtering process. A mass flow controller (MFC) and a pump system ensure a stable oxygen flow inside the chamber. Adapted from [63].

3.2 X-ray Diffractometery/ Reflectometry (XRD and XRR)

The X-ray reflectometer “D8 Advanced” from Brucker AXS is very suitable for the characterization of structural properties of thin film samples. With the X-ray reflectometry measurement at small angles one has access to the information on layer thickness, roughness and the periodicity of multilayer systems. With diffractometry measurement at high angles, one can probe the Bragg reflections, where structural information, e.g. crystal quality and lattice parameters can be obtained.

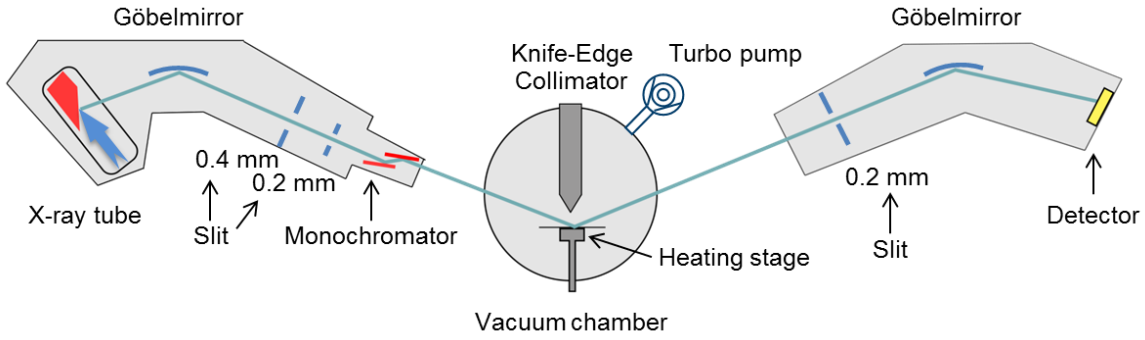

Figure 3.2: Schematic setup of the Bruker D8 Advanced X-ray reflectometer. A vacuum sample stage with a temperature unit can be installed to enable measurement at high temperatures. Adapted from [64].

Figure 3.2 displays the sketch of the Bruker D8 X-ray reflectometer. It operates with a copper X-ray source with a wavelength of λ=1.54 Å. The flight path is defined by Göbelmirrors and slits. A channel cut monochromator is mounted for the diffraction measurements to suppress background mainly from the Bremsstrahlung. Additionally a Knife-Edge Collimator (KEC) is installed to achieve an optimal collimation of the incident beam and for background suppression.

A dedicated vacuum chamber with heating stage and x-ray windows is also installed to provide the opportunity for in-situ measurements at high temperatures up to 600 °C, at high vacuum conditions of ~10^{-6} mbar.

3.3 X-ray photoelectron spectroscopy (XPS)

XPS is a surface sensitive (0.5-4nm) technique for the non-destructive analysis of the elemental composition. It utilizes photoionization and analysis of the kinetic energy distribution of the emitted photoelectrons, as illustrated in **Figure 3.3**. Therefore XPS can identify and quantify the elemental composition of the surface and determine the oxidation states of the detected elements.

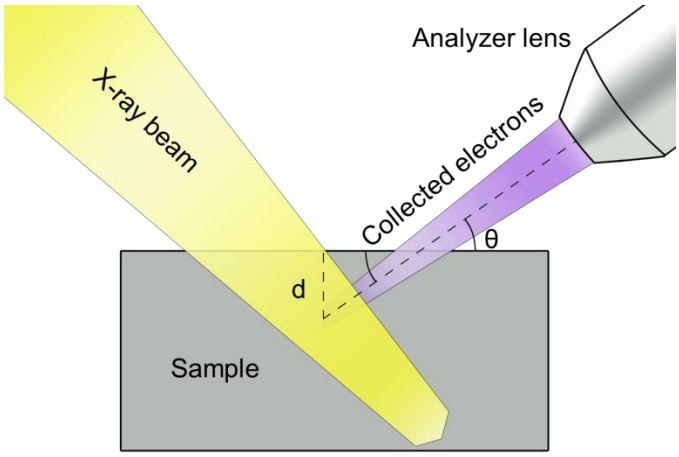

Figure 3.3: Schematic representation of photoelectron emission from a sample surface, where d is the depth of analysis, and θ is the detection angle. Adapted from [65].

In our study, the XPS studies were performed with a PHI Versaprobe II spectrometer using a monochromatic Al Kα source (1486 eV) at the institute ZEA-3, in collaboration with Dr. Heinrich Hartmann. The base pressure of the instrument was $1x10^{-9}$ mbar, rising to $1x10^{-7}$ mbar in the initial stages of the heating experiments (up to 1200 °C). The spectra were obtained using an analysis area of 200 µm in diameter with energies of 187.5 eV for survey measurements and 23.5 eV for high resolution spectra. The binding energy values are corrected by setting the binding energy of the main C1s peak to 285 eV. The spectra were analyzed using CasaXPS (version 2.3.17). Individual

components were fitted with a Gaussian (70%)-Lorenzian (30%) profile (defined as GL(30) in CasaXPS). The atomic concentration of the components of interest was calculated from the respective peak areas using instrument specific relative sensitivity factors.

3.4 Rutherford Backscattering Spectroscopy (RBS)

Rutherford Backscattering Spectrometry (RBS) is widely used for near-surface layer analysis. It determines the structure and composition of materials by measuring the Rutherford backscattering of a beam of high energy ions (typically protons or alpha particles) impinging on a sample. Compared with XPS, the analyzed depth is ~2 μm for He^+ ions, thus enabling quantitative determination of not only elemental composition, but also depth profiling of individual elements. The error of such method lies within a few percent and depends on the species of the scattering atoms. It is very sensitive for heavy elements, while less sensitive for light elements like oxygen.

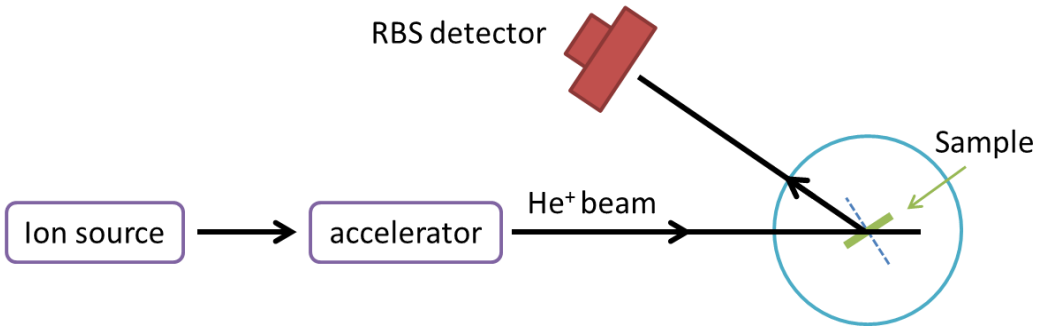

Figure 3.4: Sketch of a RBS experiment, where helium ions are accelerated towards the sample and then backscattered at the scattering angle. The backscattered ions are detected with an energy sensitive detector.

A typical Rutherford backscattering setup consists of a particle accelerator that can deliver beams of low-mass ions in the MeV range, as shown in **Figure 3.4**. The RBS

measurements in our study were carried out by Dr. Jürgen Schubert from the PGI-9 institute on a Tandetron accelerator. He^+ ions are accelerated to 1.4 MeV and used as probes. As the incident He^+ beam penetrates the sample, a small -but sufficient- number of the deflected ions will be backscattered into the detector. Their energy loss can be converted to a depth scale and in this way the RBS technique can be used to obtain several micrometer deep profiles of different atomic species. The typical RBS spectrum shows the number of backscattered particles picked up by the detector as a function of their energy. The obtained data was then analyzed with the software package RUMP [66,67].

3.5 Atomic Force Microscopy (AFM)

An Agilent Technologies 5400 Atomic Force Microscope (AFM) was employed to probe the surface morphology of thin films.

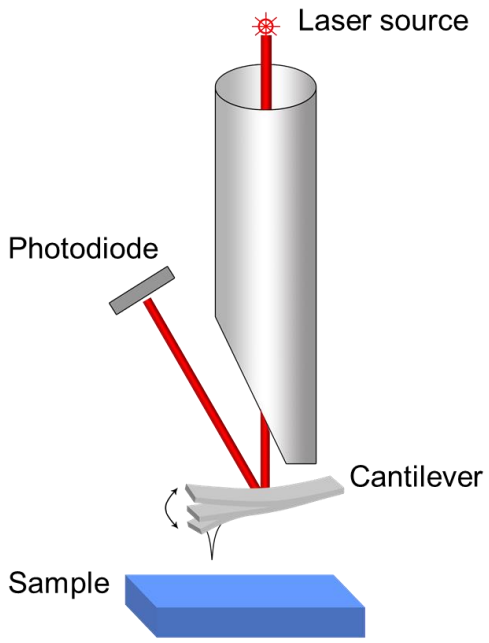

Figure 3.5: Sketch of an AFM setup, where the oscillations of the cantilever is probed by a laser beam and then detected with a photodiode detector.

Figure 3.5 shows a typical configuration of the AFM-setup. The small spring-like cantilever is carried by the support on which a measuring tip is fixed. When the tip is driven to the surface of the sample, the cantilever is excited to oscillate close to its resonance frequency. This oscillation is then measured using the reflection of a laser beam from the cantilever and probed by a position-sensitive detector. The AFM senses interactions like capillary forces, covalent forces, electrostatic forces, common repulsive interaction forces, and Van der Waals forces, etc. The change in the oscillation amplitude due to these interactions is compensated by a height correction of the cantilever realized by piezocrystals. This correction is interpreted as a topographical height profile of the sample

3.6 Scanning transmission electron microscopy (STEM)

Transmission Electron Microscopy (TEM) is a powerful characterization technique used for the observation of extremely fine details of low dimensional materials. In recent years, cutting-edge TEM and associated techniques have become effective tools for the comprehensive assessment of structural properties at the atomic scale. Scanning transmission electron microscopy (STEM) is a type of TEM which is based on the electron scattering analysis as a focused beam is scanned over a thin sample. A schematic of a STEM is presented in **Figure 3.6**. There is a wide range of possible signals available in the STEM, from which many characterization methods emerge, e.g. Bright-Field imaging (BF), Annular-Dark-Field imaging (ADF), High-Angle-Annular-Dark-Field imaging (HAADF), Electron Energy Loss Spectroscopy (EELS), and Energy-dispersive X-ray spectroscopy (EDX).

In BF mode, only the transmitted electrons leaving the sample at relatively low angles with respect to the optic axis (smaller than the incident beam convergence angle) are collected. With the annular detector, the transmitted electrons that are scattered at larger angles than a minimum angle θ contribute to the image in ADF mode. Especially at high angles, electrons are scattered incoherently, with essentially no Bragg scattering present. The image intensity is then mostly due to the individual contribution of each

atom. The signal collected by the HAADF detector will have an intensity directly related to the scattering cross-section, and thus it will depend on the atomic number of atoms in the specimen. In addition, transmitted electrons losing a measureable amount of energy are collected for EELS and the X-rays generated from the electron excitation in the sample are collected for EDX analysis.

In our study, STEM measurements using a FEI Titan 80-200 device were conducted by by Dr. Xiankui Wei at the Ernst Ruska-Centre (ER-C) at the Forschungszentrum Jülich.

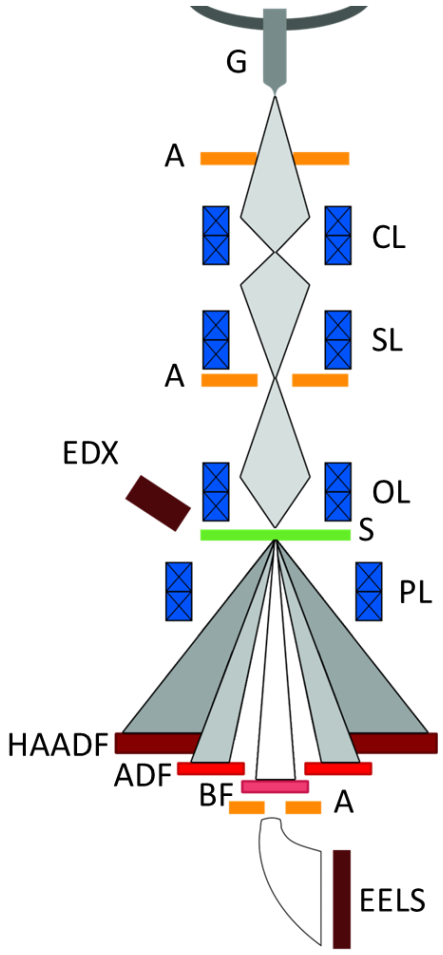

Symbol	Component
G	Electron Gun
A	Apertures
CL	Condenser Lenses
SL	Scanning Lenses
OL	Objective Lens
S	Sample
PL	Projector Lenses
BF	Bright Field Detector
ADF	Annular Dark Field Detector
HAADF	High-Angle ADF Detector
EDX	Energy-Dispersive X-ray Detector
EELS	EELS Spectrometer

Figure 3.6: Schematic diagram of an STEM microscope that depicts the main detectors and standard positions of the spectrometers. Adapted from [68].

3.7 Magnetic Property Measurement System (MPMS)

The Magnetic Property Measurement System (MPMS) from Quantum Design was employed to characterize the macroscopic magnetic properties. In **Figure 3.7**, the measurement principle of the MPMS is depicted.

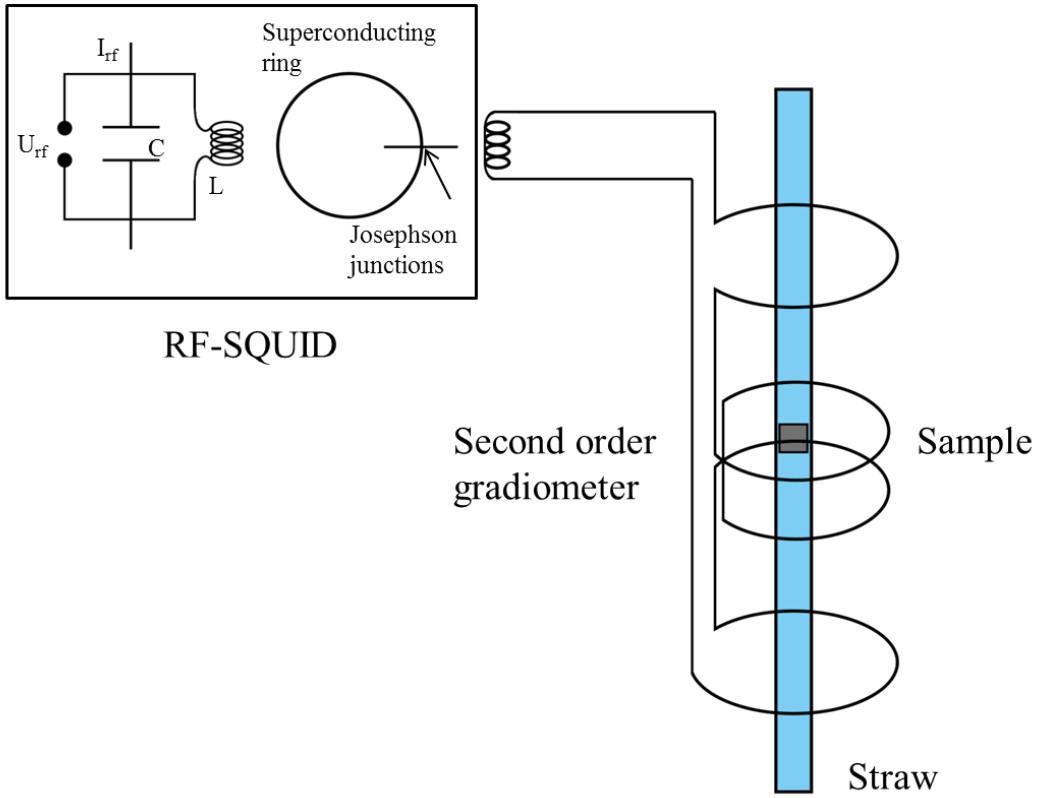

Figure 3.7: Detection system of a Quantum Design MPMS SQUID-magnetometer. The sample is mounted in a straw. Adapted from [69].

The sample is mounted in a straw like sample holder and can be moved up and down through the pick-up coils. The magnetic moment of the sample induces a current in the

second order gradiometer while it is moved. The gradiometer typically comprises a large differential pickup coil. A vertical magnetic field from -7 to 7 T can be applied using a superconducting magnet. This gradiometer is coupled to a RF-SQUID circuit. The SQUID itself is a device which consists of a superconducting ring interrupted by a Josephson junction, and a LC circuit. The current transferred from the pickup coil produces an additional magnetic flux penetrating the SQUID-ring and thus induces a current inside the superconducting ring. The experimental data of the response function are fitted to the theoretical one, which corresponds to the theoretical response when a magnetic moment is moved through a pick-up coil. A SQUID-magnetometer can probe the magnetization down to 10^{-11} A m^2.

This method works for both modes of the SQUID-magnetometer, i.e. direct current (DC) mode and reciprocating sample option (RSO) mode. In a DC measurement, the sample moves through the pick-up coil in discrete steps. Using a RSO option, an oscillation of the sample around the measurement position is performed. RSO technique offers a faster measurement and a better noise rejection due to harmonic motion than the DC technique.

3.8 Physical Property Measurement System (PPMS)

A Quantum Design Physical Property Measurement System (PPMS) was used to characterize the physical properties of the sample. The heat capacity, thermal transport properties, and electrical transport properties can be measured by such a device in applied magnetic fields between -9 and 9 T and temperatures between 1.9 and 400 K. In addition, the magnetization and AC susceptibility can also be measured using a vibrating-sample magnetometer (VSM), although with a slightly lower sensitivity of ~10^{-9} A m^2 compared to the MPMS system. In this work, the “Resistivity Option” and the “VSM Option” were used.

Figure 3.8 displays the PPMS probe and the cross-section of the probe's sample region. At the bottom of the sample chamber is a 12-pin connector pre-wired to the system

electronics. This connector allows one to plug-in a removable sample insert or sample “puck”. This connector provides the basis for all PPMS measurement inserts. Resistivity sample pucks have four contacts for each user bridge board channel, i.e. one positive and one negative contact for current and voltage. The samples are then contacted with platinum wires which are fixed on the sample surface using silver paste. Using four wires to attach a sample to a sample puck strongly reduces the contribution of the leads and joints to the resistance measurement.

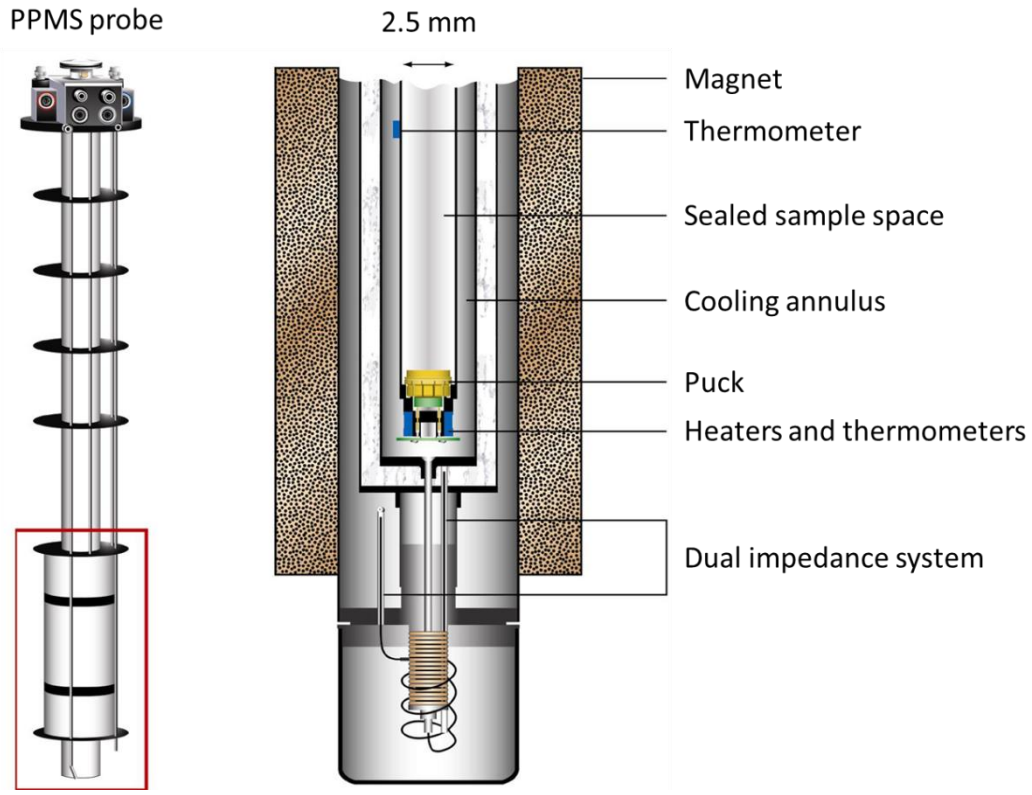

Figure 3.8: PPMS probe and cross-section of the probe's sample region, SC magnet, and dual impedance system. Source: Q. Design, Physical Property Measurement System: User's Manual (Quantum Design, Inc., San Diego, CA, 2002).

3.9 Polarized Neutron Reflectometry (PNR)

The magnetic depth profiles of the thin film samples were investigated by polarized neutron reflectometry (PNR). In our study, the magnetism reflectometer with high incident angle (MARIA) at MLZ was used [70,71].

Figure 3.9: Side view of MARIA, starting on the left with (1) casemate wall, (2) velocity selector, (3) lift with neutron guide and two Fermi chopper positions, (4) polarization chamber and lift with three positions, (5) radio frequency flipper, (6) elliptical vertically focusing neutron guide (from 4 to 9), (7) slit S1, (8) collimation base, (9) slit S2, monitor 1 and attenuators, (10) hexapod with sample position and optional magnet, (11) detector arm with ^{3}He filter and ^{3}He two-dimensional position sensitive detector, and (12) beam stop. Taken from [71].

MARIA is a vertical sample reflectometer, which is optimized for layer thicknesses between 3~300 Å and lateral structure sizes from nm to µm sizes. The overview of MARIA is shown in **Figure 3.9**. The wavelength of the incoming neutrons are selected by a velocity selector in the range of 4.5 Å < λ< 40 Å, with a maximum intensity for a wavelength of 4.5 Å. The resulting wavelength resolution is Δλ/λ = 10%. MARIA also provides polarization analysis, where the neutron beam is polarized by a polarizing guide and analyzed by a wide angle ^{3}He-cell. Different scattering channels (i.e. non-spin-flip and spin-flip) can be distinguished to reveal the alignment of the in-plane magnetization. Next to the polarizer a slit system collimates the neutron beam and shrinks the beam for an optimal illumination of the sample, leading to a reduction of the background. The beam size of the neutrons is important for resolution considerations.

The instrument is designed for small focused beam and the typical sample size is 1 cm^2. The sample is mounted in a cryostat with a vacuum of 10^{-6} mbar. The lowest temperature one can achieve is 5 K. A magnetic field of up to 1 T can be applied along the in-plane direction of the thin film sample and perpendicular to the scattering vector. After the scattering process, the scattered neutrons are detected by a two-dimensional ^{3}He detector. For simulation and analysis of the reflectometry data, a flexible script-based python program (GenX) is used [72].

Chapter 4

Structural and physical properties of $La_{0.7}Sr_{0.3}MnO_{3\pm\delta}$ thin films in dependence of a systematic variation of the oxygen content during preparation

This chapter handles the aspects of synthesis of the samples that I investigated within the framework of this thesis. Lanthanum manganite ($La_{0.7}Sr_{0.3}MnO_{3\pm\delta}$) thin films were deposited on $SrTiO_3$ substrates by High Oxygen Pressure Sputter Deposition (HOPSD). The important growth parameters such as substrate pre-treatment, growth temperature, oxygen partial pressure and growth rates will be described in detail. The optimized growth parameters for a good quality of thin film sample are determined.

In the second part, the microstructure and physical properties of the as-prepared LSMO films are characterized and discussed, where the samples were prepared at various oxygen partial pressures. The influence of the oxygen off-stoichiometry and strain effects induced by the lattice changes were investigated with regard to magnetic and electric properties.

4.1 Sample preparation

4.1.1 Substrate selection

The substrate is often taken as one of the most important issues for thin film growth. Here, the selection of a proper substrate is considered. The first requirement is to choose a substrate with a best possible lattice match compared with the film. Usually a lattice mismatch of less than 7~9 % is required for the possibility of epitaxial growth [73].

Figure 4.1(a) presents several perovskite substrates which have comparable lattice constants with an LSMO film. By comparison, the LSAT substrate and $SrTiO_3$ (STO) substrate show the smallest lattice mismatch of less than 1%, making them ideal substrates for epitaxial growth of LSMO films with good quality. Here we need to note that the LSAT substrate has a complicated chemical composition, $(LaAlO_3)_{0.3}$-$(Sr_2AlTaO_6)_{0.7}$, which may create problems considering the possible reactions and inter-diffusion between film and substrate. Therefore $SrTiO_3$ is the most promising candidate for this project.

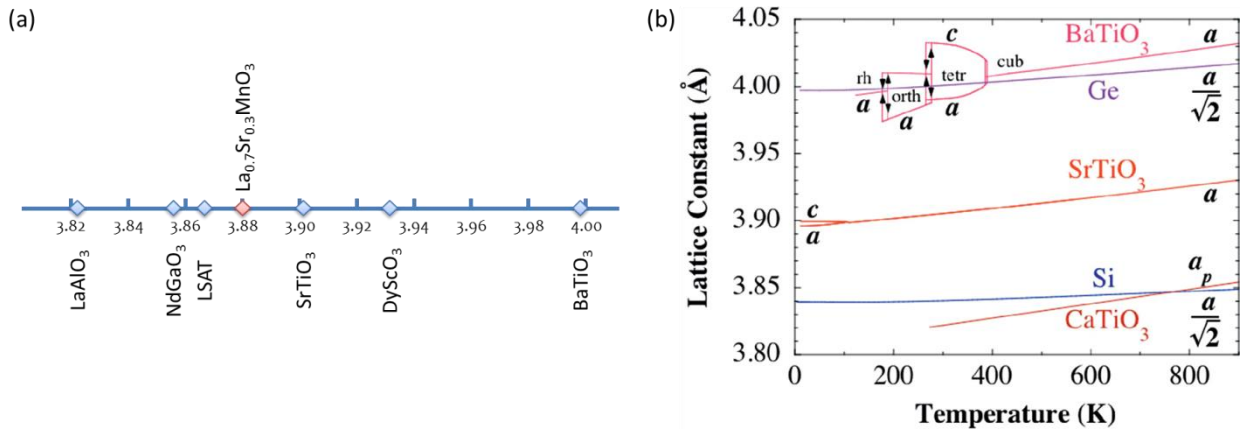

Figure 4.1: (a) Lattice parameters at room temperature of various substrates usually used for epitaxial growth. (b) Temperature dependence of the lattice constants of the perovskites $CaTiO_3$, $SrTiO_3$, and $BaTiO_3$ compared to the lattice parameter of silicon. The lattice parameters of silicon (and germanium) are divided by $\sqrt{2}$ as is relevant for the in-plane epitaxial alignment of $(100)_p$ $ATiO_3$/(100) Si with $[011]_p$ $ATiO_3$ ∥[001] Si, where the subscript *p* denotes pseudocubic indices. The pseudocubic lattice parameter a_p of $CaTiO_3$ is plotted as well. Figure reprinted with permission from [74].

In addition to the chemical compatibility, another aspect needs to be taken into account. That is the thermal stability and thermal-expansion of the substrate. Problems introduced by thermal instability can be caused by structural transformation among orthorhombic, tetragonal and cubic structure, such as in the perovsike substrate $BaTiO_3$

as shown in **Figure 4.1(b)**. Strain effects produced by the phase transitions may have profound influence on the properties of the film. This is what we should avoid in our systematic study of the role of oxygen onto the physical properties of the LSMO film.

On the other hand, the problems caused by a lattice mismatch due to thermal-expansion are more severe if the system must tolerate high temperatures. As in our case, temperatures above 500 °C are needed during film growth and post-annealing. A thermal-expansion mismatch may cause the film properties to be altered from what they would be if a mismatch were absent. Therefore the temperature dependence of the lattice constants of STO substrates should be checked beforehand. As shown in **Figure 4.1(b),** the coefficient of thermal expansion of STO substrate is small. A structural phase transition from a low temperature tetragonal phase (point group 4/mmm) to a high temperature cubic phase (point group m3m) is observed in the crystal at T_c=105 K. Above room temperature the STO substrate shows a stable cubic structure which is ideal for the further treatments at high temperature. Therefore single-crystalline $SrTiO_3$ substrates purchased from CrysTec GmbH are selected for the growth of epitaxial LSMO films. The orientation of the substrates is (001) and with one side of the surface chemo-mechanic polished.

4.1.2 Deposition parameters for HOPSD

$La_{0.7}Sr_{0.3}MnO_3$ thin films were prepared using HOPSD which is described in Chapter 3.1. The sputtering target (Size: 12.0'' Diameter × 0.125” Thick) is purchased from Kurt J. Lesker Company with high purity of 99.9%. After placing the substrates into the vacuum chamber, the sputter system was pumped by a backing pump and a turbo pump to a pressure of 5×10^{-6} mbar. In order to obtain a good film adhesion, it is necessary to clean the surface of the substrate from adatoms to achieve well defined surfaces. The STO substrate is firstly tempered at 500 °C overnight in vacuum. Then the STO substrate is continuously heated up to 1000 °C and kept for 2 hours before the start of the film growth in an oxygen atmosphere at the same partial pressure used for the subsequent growth. The pre-annealing procedure not only removes organic

residuals like hydrocarbon adatoms and molecules, but also provides atomically-flat surfaces of $SrTiO_3$ substrates [75].

After the pre-treatment of the substrate, the gate-valve between the turbo pump and the deposition chamber is closed. The turbo pump is then connected to the deposition chamber by an additional tube called “by-pass” with a smaller diameter. The reduced pumping cross section enables the control of oxygen flow by a mass flow controller (MFC) during the deposition of the film. In an oxygen atmosphere, the temperature of the substrate is reduced to the desired growth temperature. After a radio frequency power of 20 W is applied to the target initially, the plasma power is increased step by step to keep a stable and homogeneous state. This deposition comprises five relevant parameters: substrate temperature, plasma power, sputtering pressure, distance from target to substrate, and deposition time. **Table 4.1** shows the parameters and settings during deposition.

Table 4.1: Growth parameters used for $La_{0.7}Sr_{0.3}MnO_3$ thin films by HOPSD

Sample ID	Temperature [K]	Plasma Power [w]	Oxygen pressure [mbar]	Distance [cm]	Deposition time [min]
SP01	800	150	3.00	2	90
SP02	800	150	2.60	2	60
SP03	800	150	2.45	2	180
SP04	800	150	2.45	2	90
SP05	800	150	2.45	2	60
SP06	800	150	2.30	2	60
SP07	800	150	1.95	2	60

The growth temperature and plasma power are the most important factors which determine the kinetic energies of the particle on the substrate surface. Energies affect the atomic diffusion and nucleation of crystalline structures. Too low or too high kinetic

energies would change the growth mechanism and prevent the formation of a film with good quality. Growth temperatures from 650 °C to 850 °C and plasma powers ranging from 120 W to 150 W were examined carefully to search for the ideal parameters. The results indicate that the optimal parameters are 800 °C and 150 W, for the growth temperature and plasma power, respectively.

In addition, compared to low pressure sputtering, the localization of the plasma will suppress re-sputtering from already deposited material, which has then an influence on the stoichiometry. After several test experiments, the distance between target and sample was fixed to 2 cm for all subsequent depositions.

Also a crucial parameter is the oxygen partial pressure. It plays a critical role on the oxygen stoichiometry of the as-prepared LSMO films. Various samples were prepared at several oxygen partial pressures to investigate the influence on the initial states of the LSMO films. The results will be further discussed in the following sections.

After the deposition, the sample is cooled down to room temperature at a rate of 5 °C/min. The oxygen partial pressure is maintained at the same value, which was used for deposition to avoid any oxygen desorption while cooling.

4.1.3 Stoichiometry of the as-prepared sample

The advantage of sputtering techniques is the fixed stoichiometry of the target so that time consuming rate calibrations are avoided. However, the stoichiometry of the sample can be altered by different sputter rates of the different subcomponents.

Therefore it is necessary to check the actual stoichiometry of the sample after growth. RBS is an ion scattering technique that is used primarily for compositional thin film analysis. The measurements were conducted on the as-prepared LSMO film with the thickness of 45 nm. During the measurement, the energy distribution and intensity (yield) of backscattering He^{2+} ions are recorded, as shown in **Figure 4.2.** The energies of the backscattered particles depend both upon the mass of atoms as well as the depth at which a collision occurs. The peak at high energy (high channel number) corresponds to

scattering from the LSMO film while the intensities (yield) at low channel number comes from the STO substrate. On the other hand, the number of backscattered ions is directly proportional to the concentration of a given element. By correcting for the scattering cross section for each element, the exact ratio of La, Sr, Mn and O can be determined. The simulation result shows that we achieved the correct stoichiometry close to $La_{0.7}Sr_{0.3}MnO_3$. Here the Mn stoichiometry is normalized to 1. However, we need to note that RBS has high detection limits for light elements such as oxygen, with an error of more than 20 % when determining the oxygen stoichiometry. Thus oxygen deficiencies (or excess) cannot be detected using this method. Presently there is no perfect technique to precisely determine the oxygen stoichiometry in thin film systems. Other methods are considered for the quantitative measurements of oxygen composition in thin films. This part will be discussed in the next chapter.

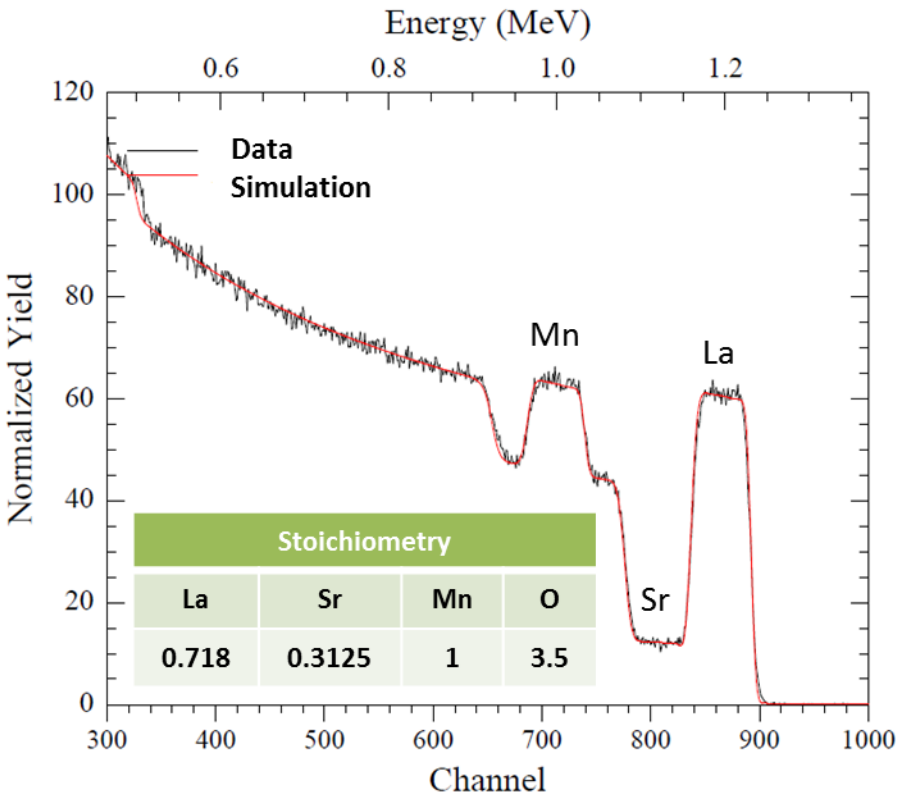

Figure 4.2: RBS spectrum with simulation of the stoichiometry of a $La_{0.7}Sr_{0.3}MnO_3$ thin film grown on a STO substrate (sample: SP07).

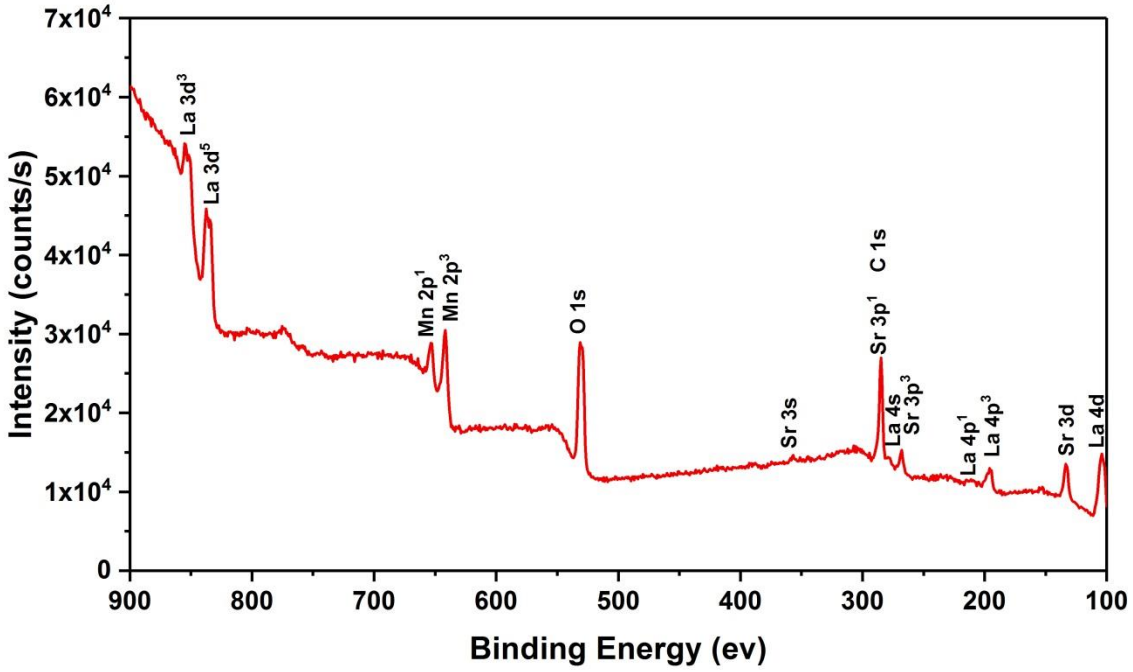

Figure 4.3: X-ray photoelectron survey scan of $La_{0.7}Sr_{0.3}MnO_3$ film grown on STO substrate measured at room temperature

In addition to the RBS analysis of the depth resolved stoichiometry of the entire film, surface sensitive X-ray photoelectron spectroscopy (XPS) was utilized to see if non-stoichiometry occurred at the surface during growth. **Figure 4.3** plots the XPS spectrum of the as-prepared film (sample: SP07). By simulations of La 3d, Sr 3d, Mn2p, O 1s peaks in the XPS spectrum, the atomic ratio of the surface chemical composition obtained. An off-stoichiometric ratio between La and Sr (La:Sr=0.26:0.40) near the film surface was found. Here the Mn stoichiometry is normalized to 1. Here we need to note that the strength of XPS technique is to provide chemical state determination. The elemental quantification is not as accurate as RBS analysis. The obtained values of atomic ratio have a relative error of 15 %. As observed by other research groups, Sr surface segregation is the most likely surface cation non-stoichiometry [76,77]. The

change of La/Sr ratio could originate from different mechanisms including Sr enrichment at the A-site, i.e. Sr replacing La on the perovskite terminated surface. Additionally, phase separations could also occur at the surface of a LSMO film. A further investigation will be discussed in chapter 5.

4.2 Oxygen pressure dependent lattice change

In this part, the structural properties of as-prepared thin films fabricated under different oxygen partial pressures are compared directly. **Figure 4.4** shows the results of XRR measurements of these samples after the preparation. The thickness of the films, the roughness of the surfaces and interfaces were determined after fitting the data, as shown below in **Table 4.2**. The reflectivity curves of sample SP07, which was prepared at a lower oxygen partial pressure, show a sharp drop in intensity, suggesting a higher roughness of the surface. In contrast, growth at a larger oxygen pressure of 3.0 mbar contributes to a good surface quality of the film.

As the stoichiometry of the layers is already confirmed by RBS, the corresponding scattering length density (SLD) versus thickness is also fitted based on the XRR data at the given composition. Here we need to note that in both fittings of the two samples, a top layer (~10 nm) has to be taken into account to achieve a better simulation. Detailed fitting parameters are given in the Appendix C.

For bulk LSMO, the SLD for X-rays is 4.781×10^{-5} Å^{-2}, while the resulting SLD for sample SP01 decreases to $(4.591 \pm 0.007) \times 10^{-5}$ Å^{-2}. With reducing the oxygen partial pressure during preparation, the SLD for sample SP07 further decreases to $(4.249 \pm 0.014) \times 10^{-5}$ Å^{-2}. Since for X-rays, the scattering arises from the interaction between the incident wave and the electron clouds of the atoms in the material, this hints towards that the electron density of LSMO films varies with the oxygen partial pressure during growth. To explain such variation, the lattice parameters for the corresponding as-prepared LSMO film need to be investigated, as the electron density depends on the volume of the unit cell and the sum of atoms within the unit cell.

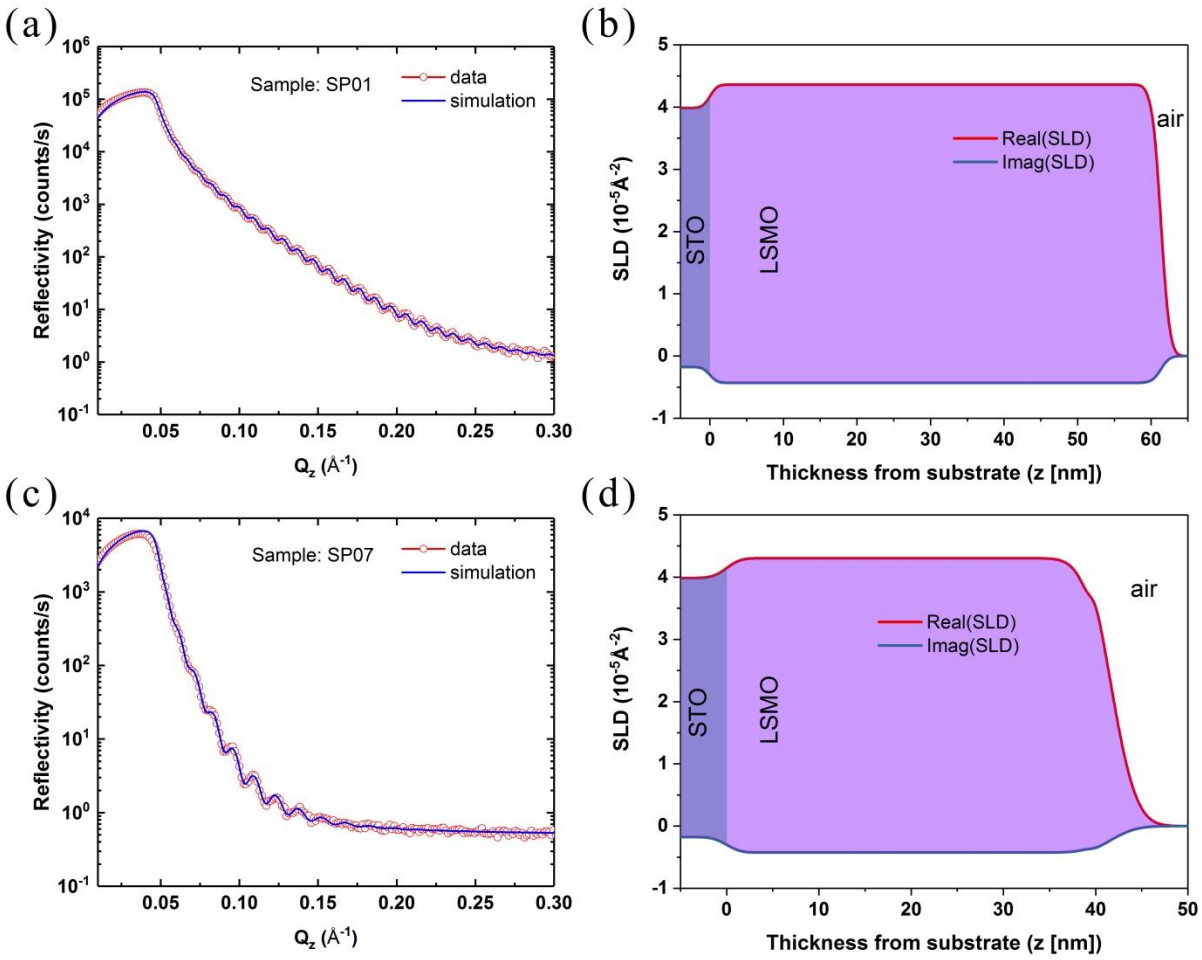

Figure 4.4: (a) and (c) shows the XRR measurements on sample SP01 and SP07 including the fit of the data, respectively. The resulting SLD with respect to the layer thickness are shown in (b) and (d). The blue area indicates the SLD of the STO substrate and the violet area indicates the SLD of the LSMO film.

Table 4.2: The fitting results of LSMO films grown at different oxygen partial pressure.

Sample ID	Oxygen pressure [mbar]	Thickness [Å]	Surface roughness [Å]	interface roughness [Å]
SP01	3.00	609.18	10.26	9.78
SP07	1.95	411.74	20.00	11.69

The crystalline quality of both samples was checked by XRD. As expected from a slight lattice mismatch between substrate and film, the LSMO films undergo a tensile stress. Here we also examine the in-plane lattice parameter of sample SP07. **Figure 4.5** displays the XRD scans around the (103) Bragg reflection for the as-prepared state and annealed state, together with the scans around the (002) reflection taken quasi-simultaneously with the (103) scans.

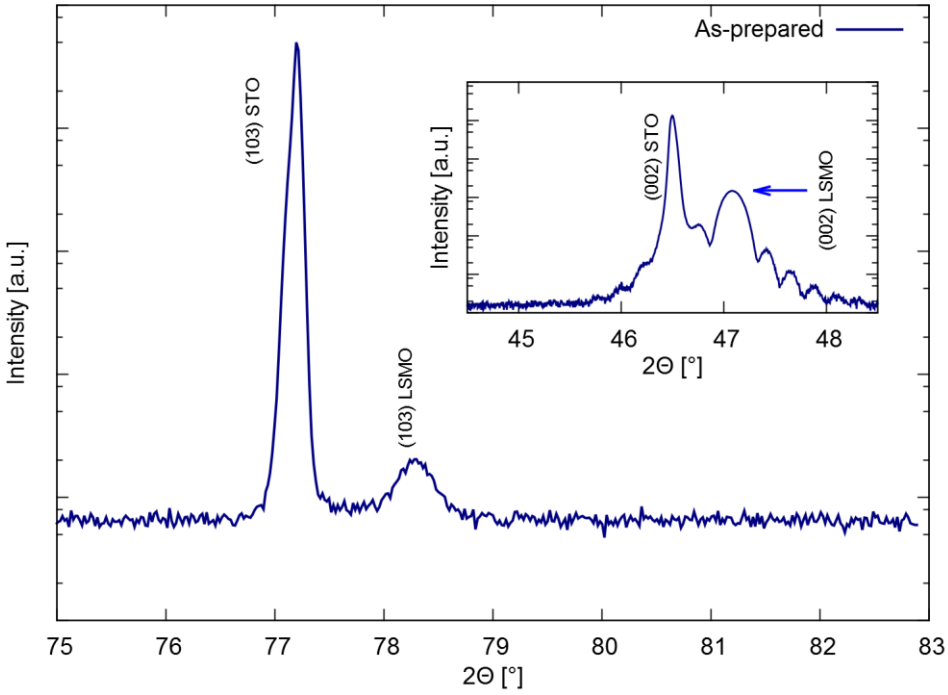

Figure 4.5: XRD scans around the (103) Bragg reflection for the as-prepared state (SP07) measured at room temperature. In the inset, the corresponding scan around the (002) reflections measured at the same time is plotted for comparison.

With a Gaussian fit, the peak positions are determined and the distance between corresponding lattice planes can be calculated. The out-of-plane lattice parameter can be directly obtained from the (002) peak position. Based on this information, the in-

plane lattice parameter can be evaluated from the (103) peak position, as it contains both in-plane and out-of-plane components. In our experiment, the STO substrate peak is stable and can be treated as a reference. For the as-prepared state, the obtained out-of-plane lattice parameter is 3.853 ± 0.001 Å, and the in-plane lattice parameter is 3.876 ± 0.010 Å.

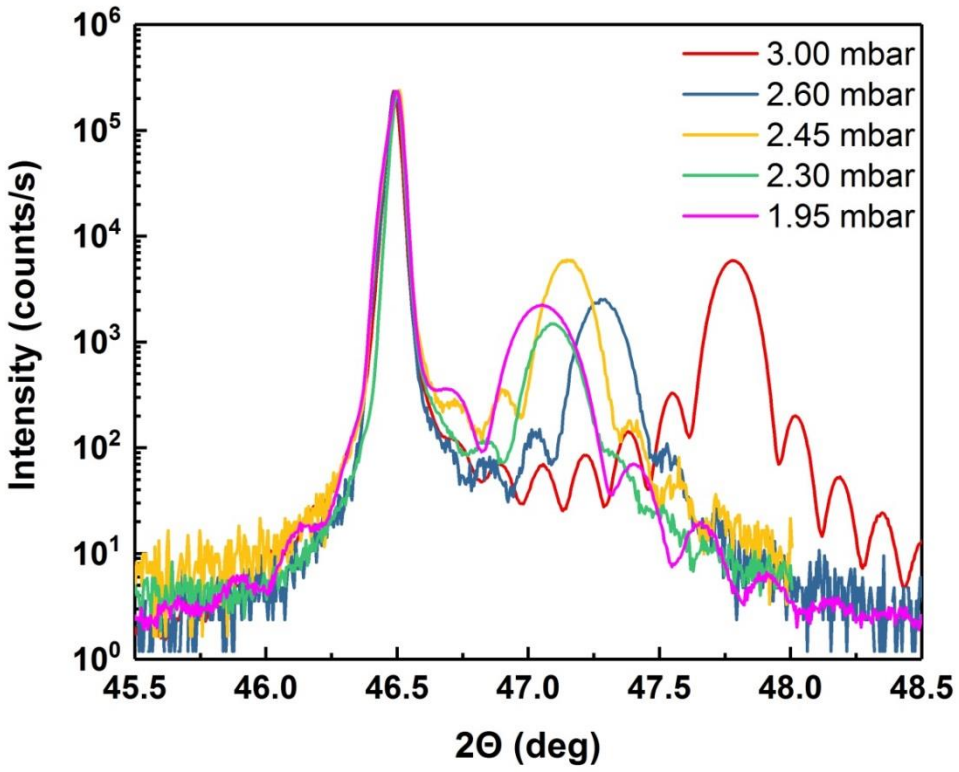

Figure 4.6: XRD θ/2θ scans around the (002) reflections of $La_{0.7}Sr_{0.3}MnO_3$ layer on the $SrTiO_3$ substrate, which were prepared at different oxygen partial pressure conditions, measured at room temperature.

Furthermore, the out-of-plane lattice constants of various as-prepared states are compared. **Figure 4.6** shows θ/2θ diffraction patterns around the (002) reflections. The

(002) Bragg peak of the LSMO film can be seen at a higher two theta value than the sharp (002) Bragg peak from the STO substrate. For all the samples the Kiessig thickness fringes are clearly visible, suggesting that the good surface quality of the film is not destroyed with changing oxygen pressure. Interestingly, with increasing oxygen pressure, the LSMO (002) peak position of the film on STO shifts to higher angle, meaning that the out-of-plane lattice constants of the LSMO film on STO is somehow sensitive to the oxygen stoichiometry. On the other hand, one can also imagine that the lattice strain on STO will be relaxed with decreasing oxygen pressure.

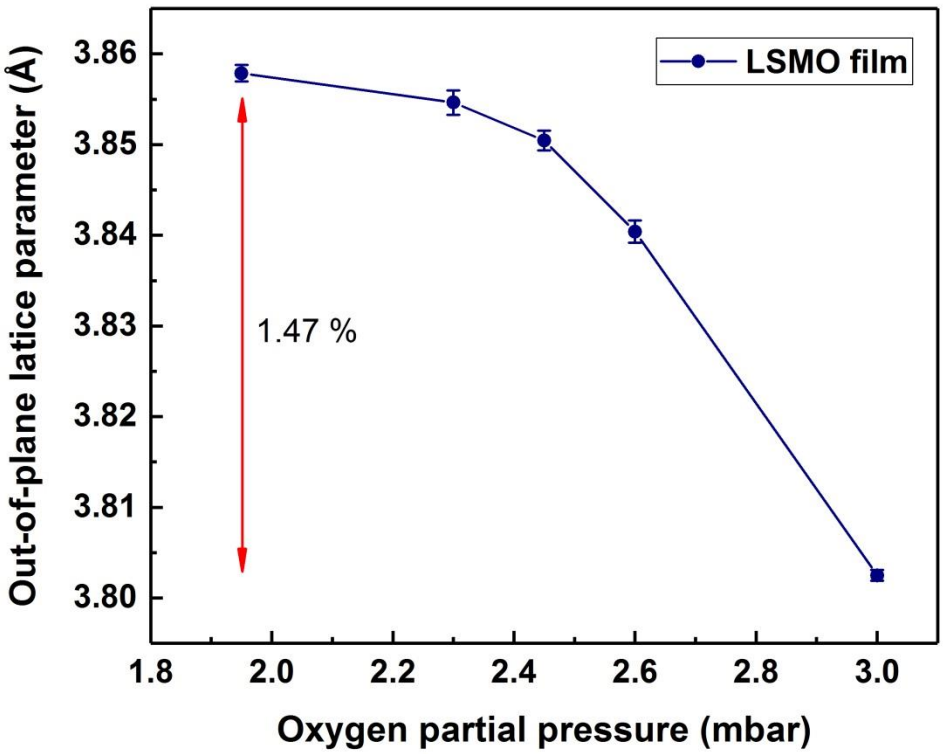

Figure 4.7: Out-of-plane lattice parameters of $La_{0.7}Sr_{0.3}MnO_3$ films at room temperature obtained from the diffraction data as function of oxygen partial pressure.

In a detailed view, the out-of-plane lattice parameter of LSMO film against oxygen partial pressure during preparation is plotted in **Figure 4.7**. The data was obtained after a Gaussian fitting, where a fixed background due to the Bremsstrahlung is assumed. Monotonic dependence of the lattice parameter can be clearly seen. The out-of-plane lattice parameter of sample SP07 (grown at 1.95 mbar) and SP01 (grown at 3.00 mbar) are 3.858 ± 0.009 Å and 3.802 ± 0.005 Å, respectively.

Form literature, such a lattice parameter change has been observed in many pseudo-cubic oxide systems, and is viewed as an additional consequence of the change of oxygen content [78–80]. In an oxygen deficient film, considering the charge balance, the oxygen-deficiency would partially convert Mn^{4+} to a Mn^{3+} valence state with a larger ionic radius while strengthen the distortion of the oxygen octahedron and increases the unit cell. Here in our study, we observe a consistent effect when we decrease the oxygen partial pressure during growth. The oxygen-deficiency induces an increase of the out-of-plane lattice parameter. On the contrary, when we increase the oxygen partial pressure during growth, a shrinking of the lattice is observed.

Combined with the observation of reduced SLD in as-prepared LSMO films, the variation of electron density in LSMO film can be rationalized by the consequent lattice expansion effect. Due to oxygen defects introduced during growth at lower oxygen pressure, the volume of unit cell increases by 4.5 %, thus decreasing the electron density of LSMO film.

In another aspect, the oxygen-deficiency would reduce the amount of atoms within the unit cell, which decreases the electron density as well. However the contribution of light element such as oxygen atoms for X-ray scattering is small. We would expect that the expansion of the unit cell plays a dominant role in the change of electron density.

Since there is no perfect technique to quantify the oxygen composition in a thin film system, one possible way is to extract information of oxygen content indirectly from lattice analysis, which can be determined by scattering methods. This idea will be further discussed in chapter 5 and chapter 6.

4.3 Oxygen stoichiometry dependent change of physical properties

While the lattice expansion induced by oxygen deficiency has been reported in many oxygen off-stoichiometric films, its influence on physical properties is not yet systematically studied. Therefore, besides the structural characterization, we compared the magnetic and transport properties of $La_{0.7}Sr_{0.3}MnO_3$ films prepared at various oxygen partial pressures, aiming at a better understanding of the effect of oxygen content onto the physical properties during growth.

4.3.1 Magnetometery

The temperature dependent magnetization at a magnetic field of 0.01 T after field cooling (FC) is shown in **Figure 4.8 (a)**. The M-T curves demonstrate that all the LSMO thin films exhibit a paramagnetic-to-ferromagnetic (PM–FM) transition at the Curie temperature. The hysteresis loop measured afterwards at 10 K shows a square like shape indicating a large size of magnetic reversal by domains wall motion and hence a high quality of the films.

For the sample SP07, which is grown at a low oxygen partial pressure of 1.95 mbar, we find a high Curie temperature (T_c) of 342 K. By a change of the oxygen partial pressure from 1.95 mbar to 2.60 mbar during growth, the Curie temperature exhibits an increase to 351 K. According to the double-exchange mechanism, T_c is proportional to the transfer integral of e_g electrons hopping between $Mn^{4+}$and Mn^{3+}. Considering the reduced out-of-plane lattice parameter with increasing oxygen pressure, the shrinking of the LSMO lattice causes a shortening of the Mn-O-Mn bond length, thus favoring the hopping of electrons. As a result, an increase of the Curie temperature is expected.

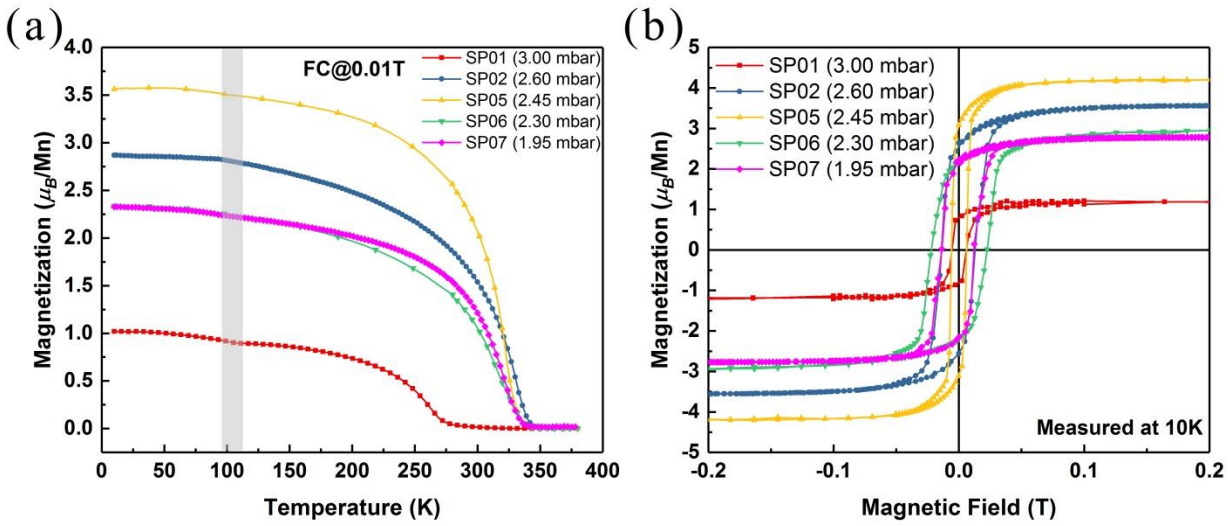

Figure 4.8: (a) Temperature-dependent magnetization of $La_{0.7}Sr_{0.3}MnO_3$ films prepared at different oxygen partial pressures, field cooling at 0.01 T (in-plane). The grey area denotes the cubic to tetragonal structural transition at 105 K for the STO substrate. (b) Corresponding hysteresis loops performed at 10 K.

On the other hand, the variation of oxygen content can be in principle thought as analogues to altering the Sr substitution ratio in La_{1-x} $Sr_xMnO_{3\pm\delta}$. If we describe the Mn^{4+}/Mn^{3+} ratio with respect to the oxygen content and Sr doping level quantitatively by the following chemical formula, then extracting oxygen from the LSMO lattice basically increase the Mn^{4+}/Mn^{3+} ratio. This has the same effect as decreasing the Sr doping level. In analogy, inserting extra oxygen to LSMO has the same consequence as increasing the Sr doping level. Therefore in our case, if we follow the Sr rich direction in the phase diagram of LSMO published by Hemberger et al [18], an increased Curie temperature is expected, which is consistent with our experiment results.

$$La_{1-x}^{3+}Sr_x^{2+}Mn_{x\pm2\delta}^{4+}Mn_{1-x\mp2\delta}^{3+}O_{3\pm\delta}^{2-} \tag{4.1}$$

Note that the sample (SP05), which is grown at an oxygen partial pressure of 2.45 mbar, has a Curie temperature in very good agreement with the reported T_c value (345 K) for bulk LSMO. In addition, it exhibits the largest saturation magnetization. Considering the XRD data, it also shows the largest intensity of the Bragg peaks compared with the other samples, if all the curves are normalized to the (002) Bragg peak of the STO substrate. Hence this sample can be used as stoichiometric reference sample for the further studies of the role of oxygen.

Remarkably, the above model does not apply to the sample SP01, which is grown at much higher oxygen pressure of 3.00 mbar. This sample possesses the smallest lattice parameter as evidenced by the XRD measurements. However, a decreased Curie temperature of 252 K is observed and the saturation magnetization drops by a factor of three compared with the reference sample. Obviously, the phenomenon cannot be simply explained by the oxygen off-stoichiometry which described above.

One explanation that could be particularly relevant for the reduction of T_c is the effects of lattice strain on magnetic behavior, which is reported by Lu Yin et al [81]. In this study the magnitude of epitaxial strain was varied in $La_{0.9}Sr_{0.1}MnO_3$ films using four different substrates and the strain-induced variation of the Curie temperature was explained quantitatively. The compressive strain shortens the in-plane Mn-O-Mn bond length, enhancing the transfer integral and thus T_c; in contrast, tensile strain reduces the T_c. Therefore in the sample SP01 with the smallest out-of-lattice parameter of 3.802 Å, a lattice shrinking leads to larger Mn-O-Mn bond length, where a reduced T_c is observed.

Another interesting feature is the kink in the field cooling curve observed at 105 K. As mentioned above, STO undergoes a structural transition from cubic to tetragonal. The induced biaxial strain will induce additional effects onto the magnetization of the system. Comparing both FC curves around 105 K, the influence onto the magnetization is more obvious for the sample with smaller out-of-plane lattice parameter, which hints towards that the extent of the strain effects varies for the as-prepared samples.

In summary, the mismatch in oxygen composition and the enhanced strain effects are two competing factors that have opposite influence onto the magnetization and should

both be taken into account to explain the magnetic behavior of the oxygen off-stoichiometric films. In addition, especially for the oxygen excessive $La_{0.7}Sr_{0.3}MnO_{3+\delta}$ films, the strain plays a more important role for the variation of T_c at higher oxygen excessive states.

4.3.2 Resistivity

For $La_{1-x}Sr_xMnO_3$ systems, the magnetic and electric properties are strongly coupled and governed by the double exchange interactions between the Mn ion spins [18,27]. This mechanism is active in the case of Mn^{3+}-O-Mn^{4+} cations, where the e_g electron on a Mn^{3+} ion can hop to a neighboring Mn^{4+} ion, when their spins are parallel. At low temperature, below the T_c, the Mn spins spontaneously align, which allows a delocalization of e_g electrons, leading to a ferromagnetic phase with low resistivity.

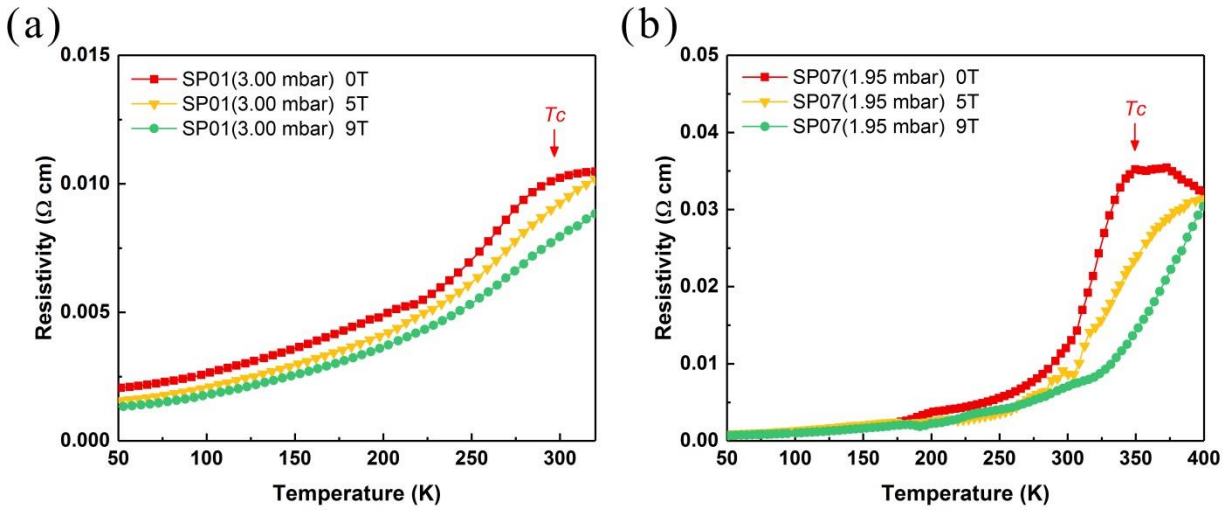

Figure 4.9: (a) Temperature-dependent resistivity of a $La_{0.7}Sr_{0.3}MnO_3$ film prepared at an oxygen partial pressure of 3.0 mbar, with in-plane magnetic field applied. (b) Temperature-dependent resistivity of a $La_{0.7}Sr_{0.3}MnO_3$ film prepared at an oxygen partial pressure of 1.95 mbar, with in-plane magnetic field applied.

As shown in the **Figure 4.9**, the resistivity monotonously decreases in the low temperature range for both samples. The metallic characteristics at low temperature is consistent with the results on bulk LSMO [82]. In particular, the sample SP07 shows an obvious metal–insulator transition peak in the resistivity curve at $T_{MI} \approx T_c$. Usually the T_{MI} is a few degrees larger than T_c, while the metal–insulator transition of sample SP01 is not well pronounced. For sample SP07, the low-temperature resistivity (7.88×10^{-4} Ω·cm at 50 K) is nearly two orders of magnitude smaller than the value measured above the metal-insulator transition temperature (3.23×10^{-2} Ω·cm at 400 K).

Moreover, the resistivity of SP07 is approximately 3 times larger than the resistivity of SP01.This could be explained in terms of the variation of lattice parameters observed for different as-prepared samples. As discussed above, the double-exchange of e_g electrons hopping between ferromagnetically coupled Mn^{4+} and Mn^{3+} ions is responsible for the ferromagnetism in manganites. In terms of the obtained out-of-plane parameter, sample SP01 exhibits a lattice shrinkage compared to SP07. The shrinking of the lattice in sample SP01 could lead to compression or rotation of the MnO_6 octahedrons, thus modifying the Mn-O-Mn bond angle and Mn-O bond length. Such a reduction of the Mn-O-Mn bond length favors enhanced e_g electrons hopping and thus an enhanced electric transport property. By analogy, one could imagine the expansion of the lattice would produce the reverse effect, which is consistent with the rise of resistivity found in many oxygen deficient transition metal oxide systems [78].

4.3.3 Colossal magnetoresistance (CMR)

For magnetite, the alignment of the Mn spins can be induced for $T>T_c$ or reinforced for $T<T_c$, by applying an external magnetic field. In **Figure 4.9**, the temperature-dependent resistivity of LSMO films were also measured with in-plane magnetic field of 5 T and 9 T, respectively. A field dependent resistivity change is observed. This tendency of a material to change the value of its electrical resistance under an external-applied magnetic field is known as magnetoresistance. $La_{1-x}Sr_xMnO_3$ with strong double exchange exhibits a rather large negative magnetoresistance, so-called CMR, which

peaks at about T_c. **Figure 4.10** shows the field-dependent resistance of the $La_{0.7}Sr_{0.3}MnO_3$ films with applied in-plane magnetic field for two samples prepared at different oxygen pressure.

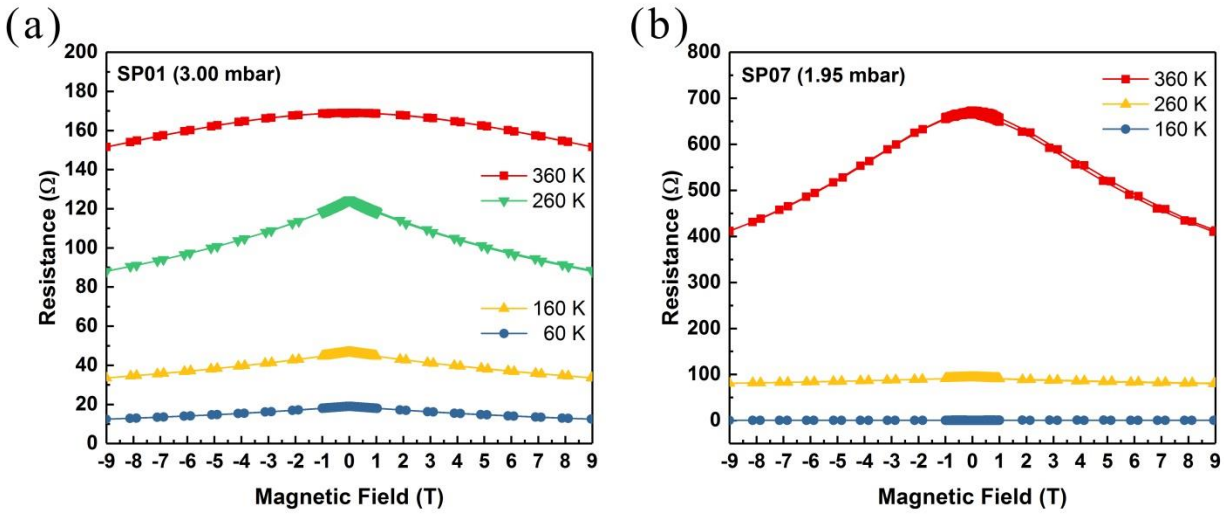

Figure 4.10 (a) Field-dependent resistance of a $La_{0.7}Sr_{0.3}MnO_3$ film prepared at an oxygen partial pressure of 3.0 mbar. (b) Field-dependent resistance of a $La_{0.7}Sr_{0.3}MnO_3$ film prepared at an oxygen partial pressure of 1.95 mbar. Field applied in-plane.

For both samples, the resistance decrease with increasing magnetic field, which is consistent with the reported negative magnetoresistance for LSMO. Near T_c, the decrease of the resistance becomes steeper, indicating that the maximum CMR effect is obtained close to T_c. In a detailed view, the temperature-dependent magnetoresistance values $[\rho(H) - \rho(0)]/\rho(0)$ are calculated for two as-prepared states (SP01 and SP07), as shown in **Figure 4.11**. The temperature of maximum colossal magnetoresistance effect corresponds well to T_c. A pronounced CMR effect of more than 60 % is found around 310~340 K in the sample prepared at a lower oxygen partial pressure.

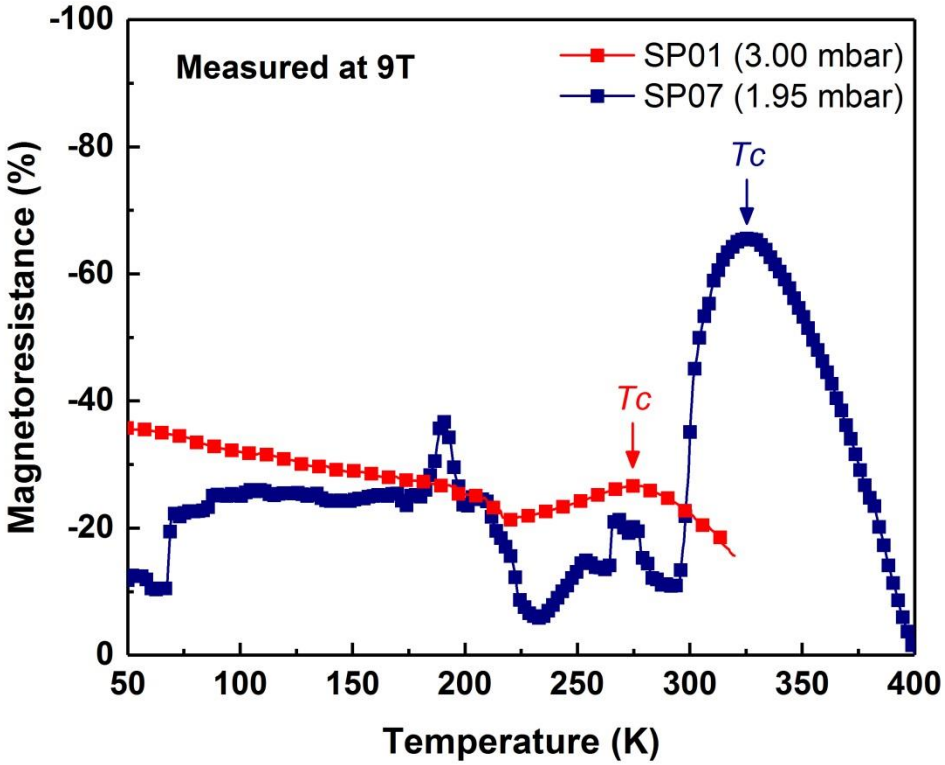

Figure 4.11: Temperature-dependent magnetoresistance of $La_{0.7}Sr_{0.3}MnO_3$ films prepared under different oxygen partial pressure. The critical temperature are marked by the arrows. The small jumps observed in the blue curve around 190 K and 270 K are artifacts due to signal fluctuations during the resistivity measurements and are not reproducible.

4.4 Summary

We demonstrate that epitaxial $La_{0.7}Sr_{0.3}MnO_3$ single layers can be successfully grown on $SrTiO_3$ substrates by HOPSD. A smooth surface and good crystal structure of LSMO film have been achieved, which is characterized by XRR and XRD. By tuning the oxygen partial pressure during growth, the out-of-plane lattice parameter of the as-prepared LSMO films can be varied by 1.47 %. This effect is attributed to the induced

oxygen defects during preparation. The sample prepared at a lower oxygen pressure of 1.95 mbar exhibits the closest lattice parameter with the reported bulk value.

The desired stoichiometry of $La_{0.7}Sr_{0.3}MnO_3$ of the entire film was verified by RBS measurement. An enrichment of atomic ratio of Sr is found at the surface (~ 10 nm) by XPS measurements. XRR data reveals a variation in scattering length density for two samples prepared at different oxygen pressure.

The magnetic and electric transport properties were characterized for different as-prepared LSMO samples. We demonstrate that the magnetic properties are highly dependent on the oxygen stoichiometry of LSMO film. The sample grown at an oxygen partial pressure of 2.45 mbar exhibits a Curie temperature in very good agreement with the reported T_C value (345 K) for bulk LSMO, and has the largest saturation magnetization. In contrast, the LSMO film prepared at a higher oxygen pressure of 3.0 mbar shows reduced T_c and saturation field.

On the other hand, both samples exhibit a metal-insulator transition and show a CMR effect, where the T_{MI} corresponds well to the Curie temperature. However, in the sample grown at higer oxygen partical pressure, the CMR effect is not well pronounced. A stronger CMR effect of more than 60 % is evidenced in the LSMO film grown at an lower oxygen partial pressure of 1.95 mbar.

Chapter 5

Reversible control of physical properties via oxygen vacancy-driven topotactic transition in $La_{0.7}Sr_{0.3}MnO_{3-\delta}$ thin films during post-annealing

In this chapter, LSMO films at two different as-prepared states are discussed, where also systematic studies during post-preparation treatments upon different annealing states were performed. A significant development in recent years is the realization of the layered vacancy ordered brownmillerite ($ABO_{2.5}$) structure from a perovskite-structure framework [8,13,14,83]. In this study, the transformations from perovskite to brownmillerite and vice versa were achieved in epitaxial $La_{0.7}Sr_{0.3}MnO_{3-\delta}$ films by a post-preparation annealing treatment. An in-situ x-ray diffraction method was employed to characterize the structural change in real-time. The transformation mechanisms between distinctive topotactic phases are investigated. Polarized neutron reflectometry was employed to probe the depth profile of both the nuclear and magnetic scattering length density. Besides the structural phase transitions, the crucial role of oxygen content for the physical properties in LSMO films is investigated systematically. In addition, In-situ X-ray photoelectron spectroscopy (XPS) analysis of the surface was carried out, focusing on the oxygen electronic band. The oxygen stoichiometry change at the surface is identified.

5.1 Structural analysis during post-annealing treatment

Since the role of oxygen content after sample preparation for the structural and physical properties is mostly unknown, it is necessary and interesting to study the influence of

the oxygen content in a post annealing treatment. The ability to control the oxygen composition after the preparation may provide the possibility to dynamically tune the physical properties e.g. for applications and also establish a comprehensive understanding of the structure-property relationship.

The post-annealing treatments were performed in a vacuum chamber (base pressure 10^{-6} mbar) of a Bruker D8 instrument, where in-situ X-ray diffraction (XRD) and reflectometry (XRR) measurements can be undertaken without breaking the vacuum. For post-annealing, two well characterized samples SP01 (3.00 mbar) and SP07 (1.95 mbar) were investigated, which were prepared at different oxygen partial pressures.

5.1.1 Lattice expansion effect induced by post-annealing

Figure 5.1 shows the in-situ XRD scans of the (002) Bragg peak measured while annealing the sample at 400 °C in a vacuum of 10^{-6} mbar for the first 40 hours. Due to thermal expansion, both the Bragg peaks of the LSMO film and the STO substrate will show a shift compared with the XRD curves at room temperature (shown in **Figure 5.5**). After the annealing temperature is reached, a realignment of the sample height is performed to move the sample back into the center of the x-ray beam and a corresponding rocking curve measurement was performed to calibrate the geometry again. Then the XRD patterns were recorded at an interval of one hour. With increasing annealing time, one can observe a tendency of the (002) LSMO Bragg peak to shift towards lower 2θ values, indicating an increase of the out-of-plane lattice parameter.

In a more detailed view focusing on the (002) LSMO peak region, the movement of the Bragg peak is clearer. In addition, the peak maintains the same width before and after annealing, suggesting no obvious change of the crystallite size within 40 hours. All curves are fitted using a Gaussian function with a fixed Bremsstrahlung background. The out-of-plane lattice parameters of both LSMO film and STO substrate are obtained from the fitting results, as shown in **Figure 5.2**.

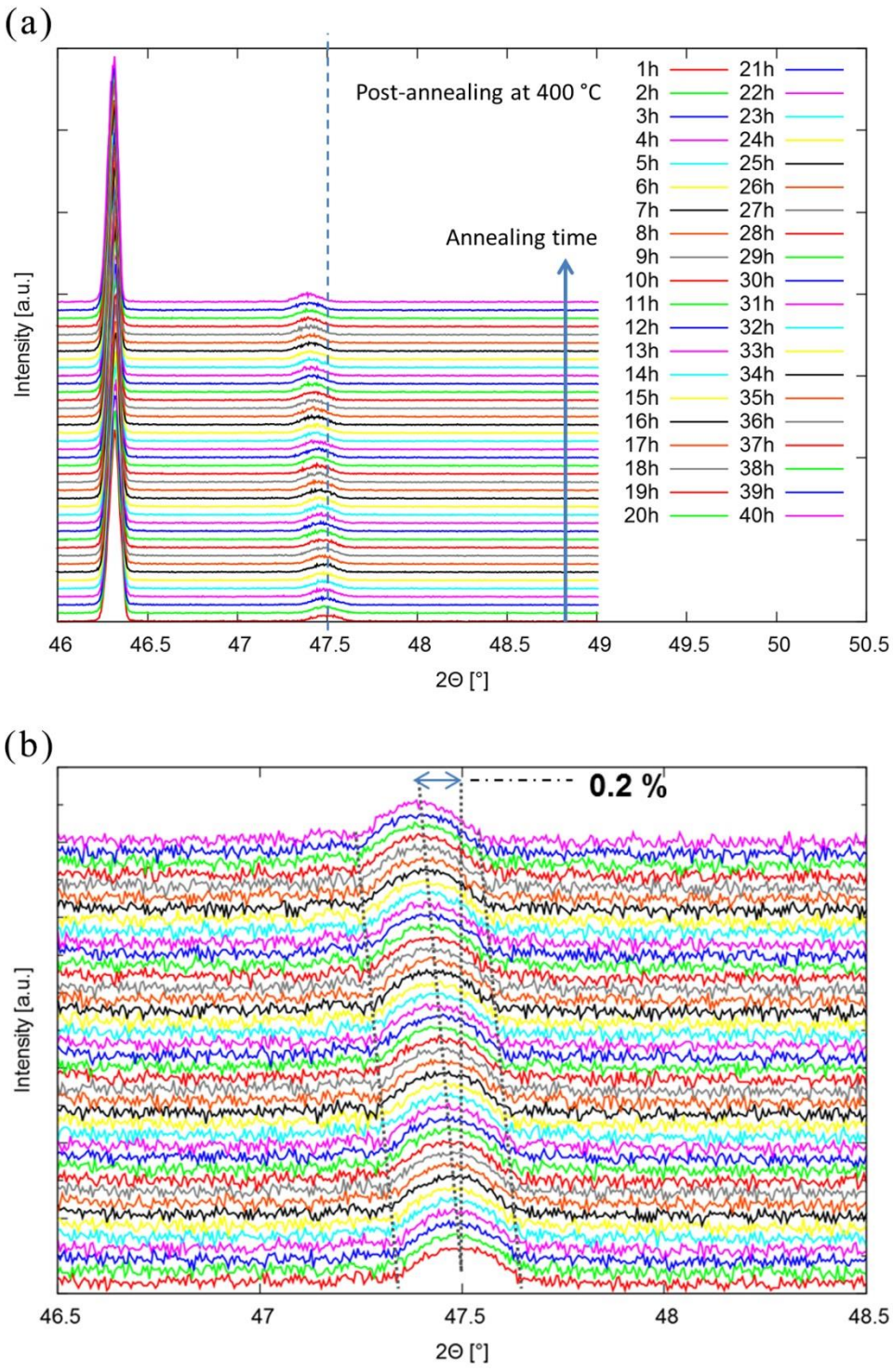

Figure 5.1: (a) In-situ XRD scans of the $La_{0.7}Sr_{0.3}MnO_3$ film on a $SrTiO_3$ (002) substrate (sample: SP01) measured during annealing in vacuum at 400°C. (b) Detailed view of in-situ XRD scans focusing on the (002) Bragg peak of the $La_{0.7}Sr_{0.3}MnO_3$ film.

A shift of the Bragg peak towards lower 2θ value indicates an expansion of the lattice. The corresponding out-of-plane lattice parameter shows a linear increase in the first 40 hours of annealing. This increase of the lattice parameter is generally regarded as an indication of oxygen O^{2-} desorption from the LSMO lattice, as the manganese ions change to a lower valence state, which has a larger ionic radius to compensate the change of total charge in the unit cell. However, the gradual change of the lattice parameter is not fast at 400 °C. In the first 40 hours of annealing, the increment of the lattice parameter is only 0.2 % and the curve still displays a linear trend. Other post-annealing parameters such as temperature have to be tuned to obtain a faster evolution of the out-of-plane parameter. Here we need to note that below 300 °C the reflections do not shift when annealed for even 60 hours.

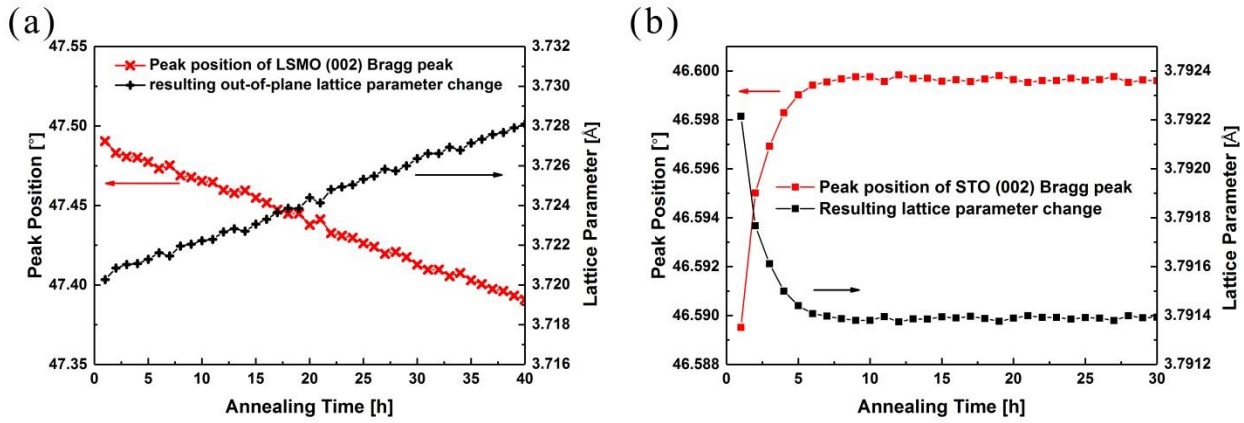

Figure 5.2: The (002) Bragg peak peak position and resulting out-of-plane lattice parameter as function of the heating time. (a): LSMO film; (b): STO substrate, for sample SP01.

Surprisingly, for the STO substrate, the (002) reflections show a contrary moving trend compared with the LSMO film during annealing, as shown in **Figure 5.2** (right). The out-of-plane lattice parameter decreases exponentially for STO in the first 5 hours, and then reaches a plateau during the remaining annealing time. Compared with the effect of

oxygen release, this decrease in lattice parameter can be ascribed to the oxygen incorporation in the STO lattice, which is a strong indication that the oxygen desorption of the LSMO film not only occurs at the surface but also at the interface. Some oxygen atoms diffuse into the STO through the film/substrate interface during the earlier stage of annealing, which causes a lattice parameter change in STO.

However, as the annealing proceeds, the oxygen content in STO starts to saturate after a few hours, where the oxygen diffusion at the interface reaches a limit. For the remainder of annealing time, the oxygen desorption of the LSMO film only occurs at the film/vacuum side. One should note that the decrease in the lattice parameter of STO is only 0.02 %, which is one order of magnitude smaller than the lattice change of the LSMO film. Hence, the induced strain effect will be negligible. The STO reflections can still be viewed as a proper reference peak for the further study.

5.1.2 Roughness change induced by post-annealing

AFM pictures of the LSMO film surface were measured before and after the annealing procedure in order to compare the roughness.

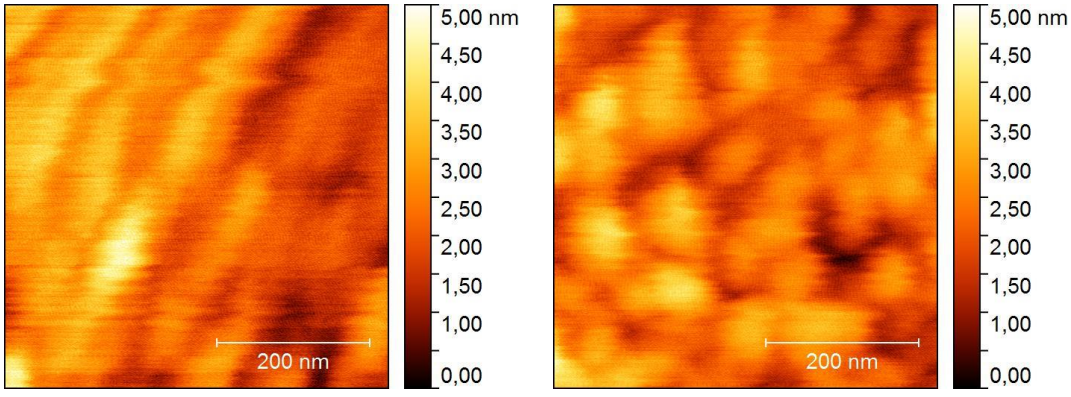

Figure 5.3: AFM measurement of the LSMO film (sample SP01) with topography. Left: as-prepared state; Right: after annealing for 40 hours.

As one can see from **Figure 5.3**, the film shows a relatively flat surface with traces of a step-shaped morphology, an indication of Frank–van der Merwe (layer by layer) growth. In comparison, island-shaped surface morphology emerges after annealing for 40 hours. As reported, post-annealing can have different effects on the thin film depending on the nature of the material and the process parameters used while annealing [84–87]. In our case, an increase of the surface roughness is revealed after annealing at 400 °C as compared to the as-prepared LSMO films.

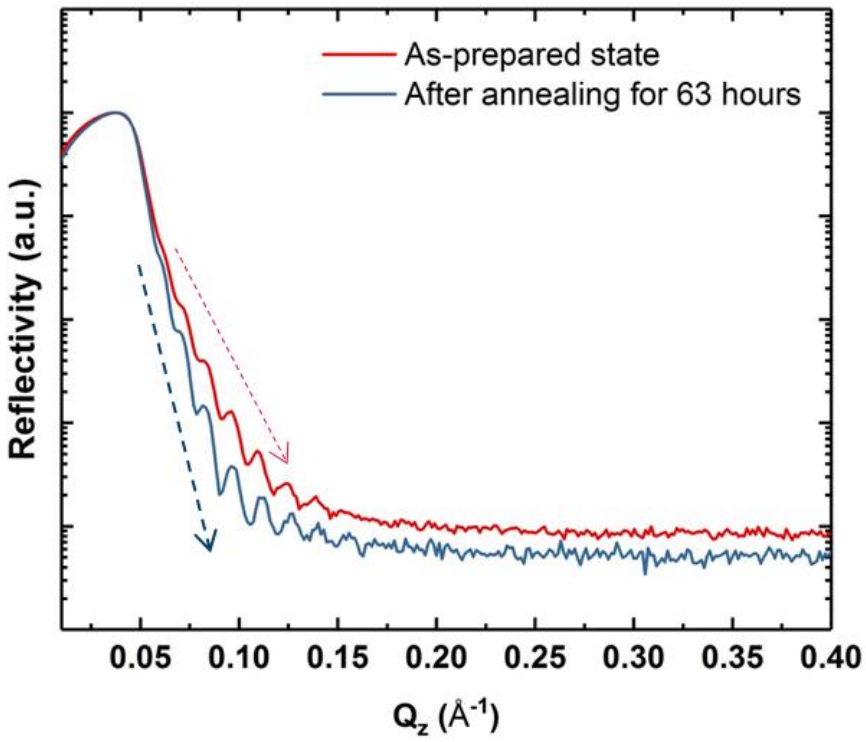

Figure 5.4: XRR measurement of the LSMO film on STO substrate (sample SP07). The arrows indicate the decline of reflectivities due to different surface roughnesses.

The change of roughness is also analyzed by the XRR measurements. **Figure 5.4** shows reflectivities measured before and after post-annealing at 500 °C in vacuum. The

density of the LSMO film remains identical before and after annealing as both curves exhibit the same value of the critical angle of total reflection. The roughness causes diffuse scattering, and therefore the density dependency of the reflectivity indicates the change of surface and interface roughness. As shown in the figure, the reflected intensity decreases faster after annealing, indicating an increase of surface roughness. On the other hand, the amplitude of the oscillations increase, which suggests a decrease of interface roughness after annealing.

5.1.3 Influence of thermal expansion on the lattice parameter

For sample SP07, a series of post-annealing experiments have been performed at different temperatures (200 °C, 300 °C, 400 °C, 450 °C, 500 °C, and 600 °C, respectively). Firstly the temperature was increased step by step to investigate the effects of thermal expansion on the lattice parameter.

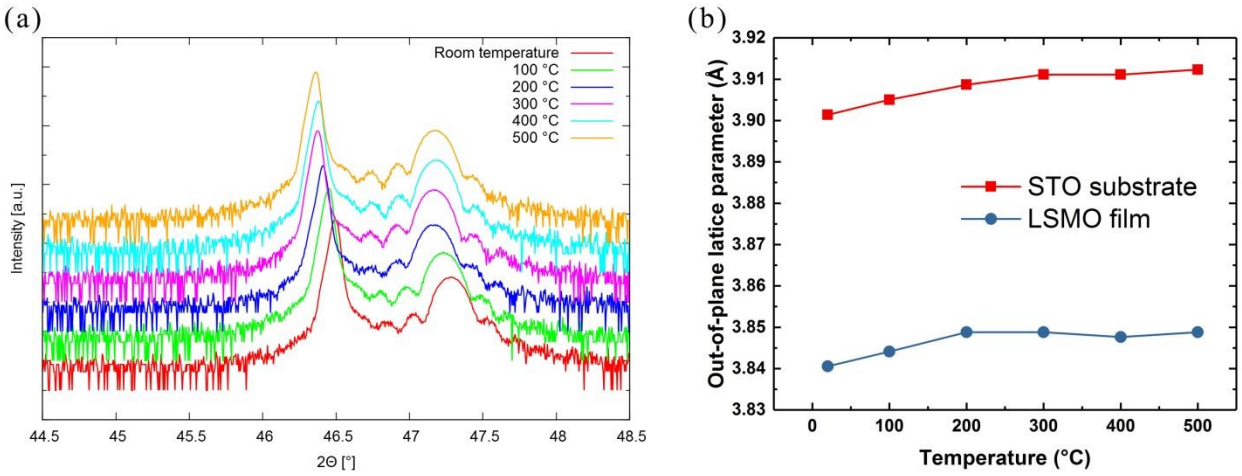

Figure 5.5: (a) XRD scans of as-prepaed $La_{0.7}Sr_{0.3}MnO_3$ film measured at various temperatures. (b) Resulting out-of-plane lattice parameter change versus the annealing temperature.

Figure 5.5 shows the XRD patterns measured after the sample has reached thermal equilibrium at the corresponding temperature. The lattice constants increase with increasing temperature, indicative of positive thermal expansion coefficients for both the LSMO film and STO substrate, which is consistent with the literature [74].

In addition, the difference between the gradients for both curves is relatively small, suggesting a close value of thermal expansion coefficients for the LSMO film and the STO substrate. This means the lattice for the film and the substrate still match with each other at high temperatures.

5.1.4 Structural evolution from PV to BM induced by oxygen desorption

In comparison to the post-annealing treatment at 400 °C, the annealing experiments of the LSMO films were also conducted at higher annealing temperatures. **Figure 5.6** displays the corresponding in-situ XRD patterns around the (002) reflections measured at 500 °C after the sample reached thermal equilibrium.

With increasing the annealing temperature to 500 °C, the shifting of the LSMO Bragg peak becomes “faster” compared to what is observed at 400 °C. From the first recording of the crystal structure at the beginning, the (002) Bragg peak of the LSMO film is clearly seen at a higher Q_z value than the sharp (002) Bragg peak of the STO substrate with the Kiessig fringes still visible. As the annealing proceeds, the (002) reflection of the film starts to shift towards lower angles, corresponding to an expansion of the lattice. This is attributed to the gradual oxygen loss within the film, as also discussed for the case of 400 °C. The lack of oxygen atoms in the film will contribute to a lower oxidation state of the Mn ions, if the charge balance is considered. With a coherent increase of oxygen deficiency (δ), more Mn ions are converted to a lower valence state with a larger ionic radius, which in turn increases the distortion of the oxygen octahedron and results in an expansion of the unit cell. After 15 hours of annealing, the film peak shifts even across the substrate peak position, suggesting a highly oxygen deficient state with a larger level of oxygen loss.

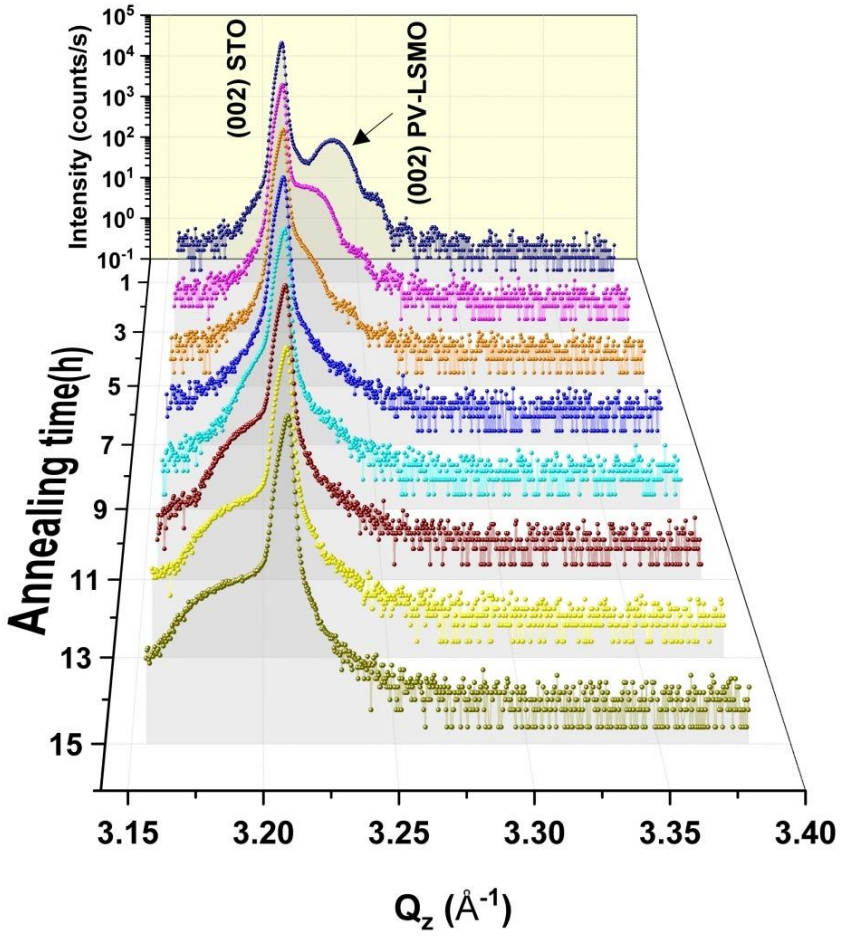

Figure 5.6: In-situ XRD scans recorded at one hour intervals during vacuum annealing at 500 °C of a 45 nm $La_{0.7}Sr_{0.3}MnO_{3-\delta}$ film on a $SrTiO_3$ (001) substrate. For clarity, not all the data are shown. The arrow indicates the thin film (002) reflection at the beginning of the annealing experiment.

In a detailed view, the time-dependent out-of-plane lattice parameter change is plotted in **Figure 5.7**. Interestingly, a clear deviation from a simple monotonic increase of the lattice parameter depending on the annealing time is observed. The ascent curve of the out-of-plane lattice parameter becomes steeper when the film peak shifts closer to the substrate peak. After the film peak shifts across the substrate peak, an inhibited expansion of the lattice is found. Here, one can expect that the expansion of the film

lattice is also affected by an additional energy associated with the epitaxial strain from the substrate. When the expanded unit cell of oxygen deficient LSMO becomes identical to the STO substrate one, the associated strain energy approaches a minimum value as no strain is involved. This might lead to the observed deviation from a linear dependency.

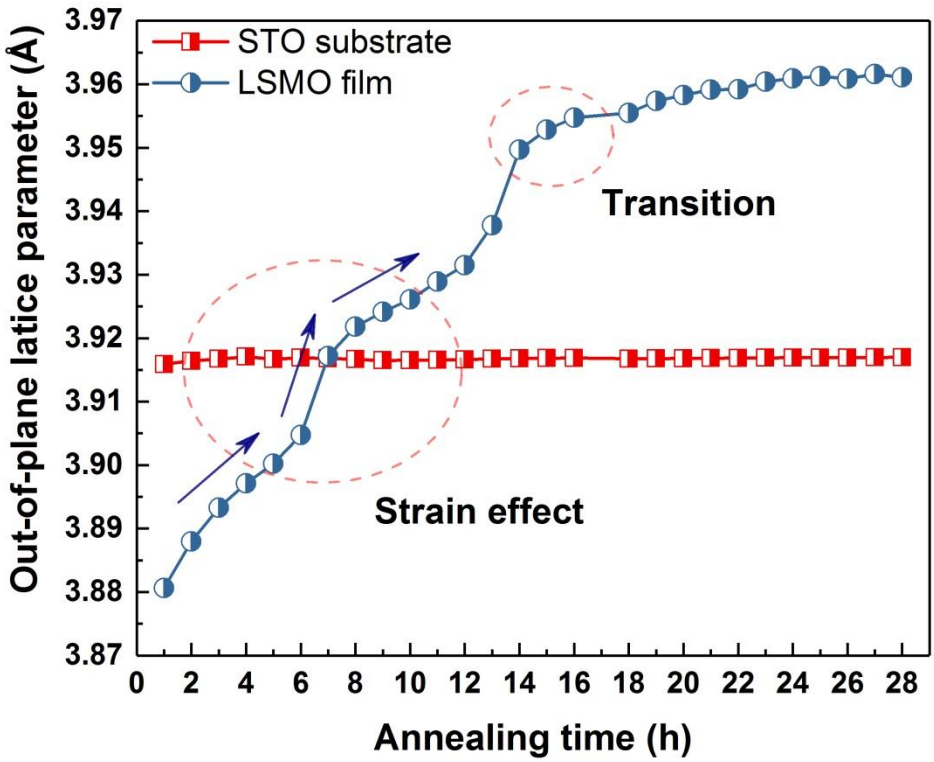

Figure 5.7: The out-of-plane lattice parameters for both the film and substrate obtained from a Gaussian fitting of the diffraction data. Dashed circles indicate the strain effect and the predictive signature of a phase transition, respectively.

To explain this, the strain states of LSMO film are investigated for the as-prepared state and the annealed state, respectively. **Figure 5.8** displays the XRD scans around the

(103) Bragg reflection for the as-prepared state and annealed state, together with the scans around the (002) reflection taken quasi-simultaneously with the (103) scans. With a Gaussian fit, the peak positions are determined and the distance between corresponding lattice planes can be calculated. The out-of-plane lattice parameter can be directly obtained from the (002) peak position. Based on this information, the in-plane lattice parameter can be evaluated from the (103) peak position, as it contains both in-plane and out-of-plane components. In our experiment, the STO substrate peak is stable and can be treated as a reference. The measured in-plane lattice parameter for STO is 3.919 ± 0.002 Å. For the as-prepared state, the obtained out-of-plane lattice parameter is 3.853 ± 0.001 Å, and the in-plane lattice parameter is 3.876 ± 0.010 Å, suggesting that the LSMO film is strained at the initial state.

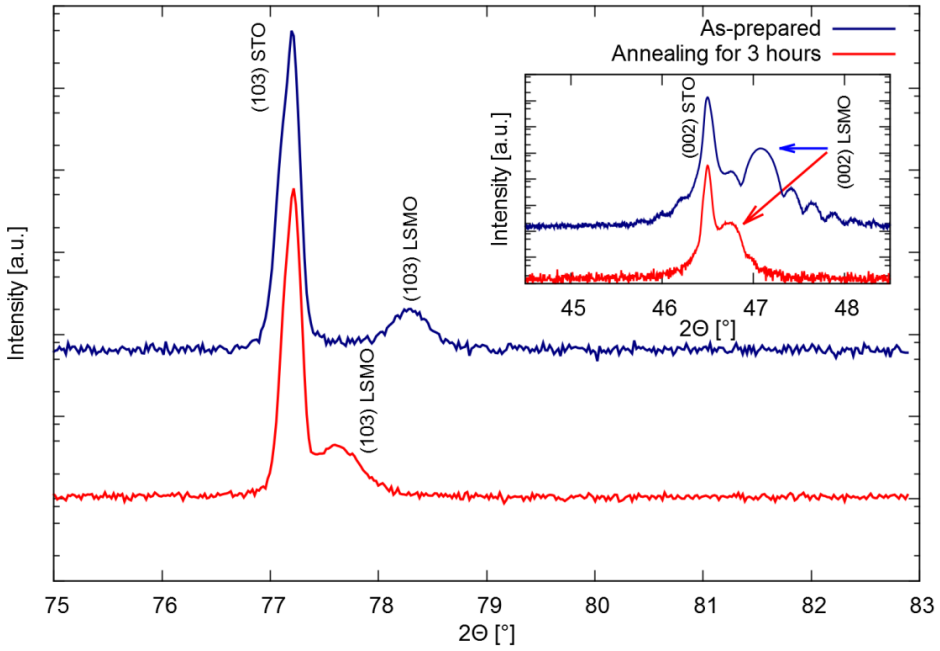

Figure 5.8: XRD scans around the (103) Bragg reflection for the as-prepared state and annealed state measured at room temperature. In the inset, the corresponding scans around the (002) reflections measured at the same time for each state are plotted for comparison.

After annealing for 3 hours at 500 °C in vacuum, a lattice expansion effect is induced by oxygen vacancies as discussed above. Here both (002) and (103) are found to shift towards lower angles. The corresponding out-of-plane lattice parameter increases to 3.885 ± 0.005 Å. The in-plane lattice parameter for the annealed state is 3.910 ± 0.016 Å, which indicates that the film still remains strained. The result shows that the film remains strained after annealing, and at the same time an increase of the in-plane lattice parameter is observed. This suggests that the lattice expansion occurs in three dimensions.

Here we need to note that the real time measurements can only focus on the out-of-plane lattice constant via the (002) peak due to practical reasons. In our study, the intensity for the (002) film Bragg peak is above 100 counts/s, while the intensity for the (103) film Bragg peak is below 10 counts/s. Therefore the XRD scans for the (103) Bragg peak need much longer exposure time to separate the peak from the background. The determination of the in-plane lattice parameter needs information from both (002) and (103) reflections. This makes the real-time monitoring of the in-plane lattice parameter during annealing not possible with the present experimental possibilities.

With further annealing, the out-of-plane lattice parameter saturates at a plateau. During this part of the structural change, the LSMO film constitutes a vacancy-disordered solid solution, still within the PV structure as no other peaks are observed. A cooperative long-range migration of oxide-ions is considered to take place during this process [15,16].

However, at around 15 hours of annealing, a jump in the ascent curve of the out-of-plane lattice parameter is observed, which is considered as a predictive sign of a phase transition. As also shown in the real-time monitored XRD patterns (**Figure 5.9)**, a Bragg peak from an oxygen-deficient new phase evolves at a lower Q_z value while the intensity of the initial PV peak decreases simultaneously. One can expect that the energy accumulated from the oxygen release is large enough to trigger a structural phase transition. A first order transition with coexistence of the two phases is observed. In addition, the positions of both diffraction peaks do not shift during the progressive transformation.

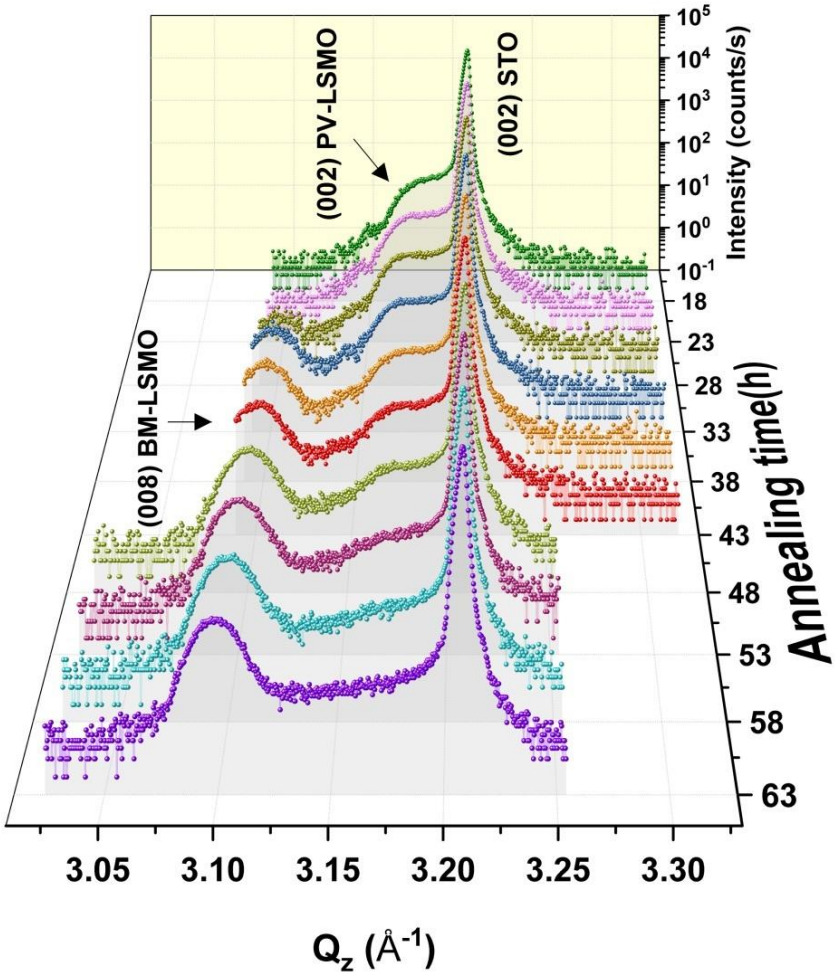

Figure 5.9: In-situ XRD scans recorded at one hour intervals during vacuum annealing at 500 °C of a 45 nm $La_{0.7}Sr_{0.3}MnO_{3-\delta}$ film on a $SrTiO_3$ (001) substrate. For clarity, not all the data are shown. Arrows indicate the thin film (002) and (008) reflections, respectively.

Upon continued annealing (t > 63 hours), a BM structure emerges eventually as the reflections of type (0 0 l) with l=2n are observed in the full range XRD pattern (**Figure 5.10**), which is the unique "fingerprint" of the BM phase, originating from the alternating octahedral and tetrahedral sub-layers [2,83,88]. The BM phase we found is stable in ambient atmosphere once it is formed and the obtained out-of plane lattice parameter is 16.449 ± 0.002 Å.

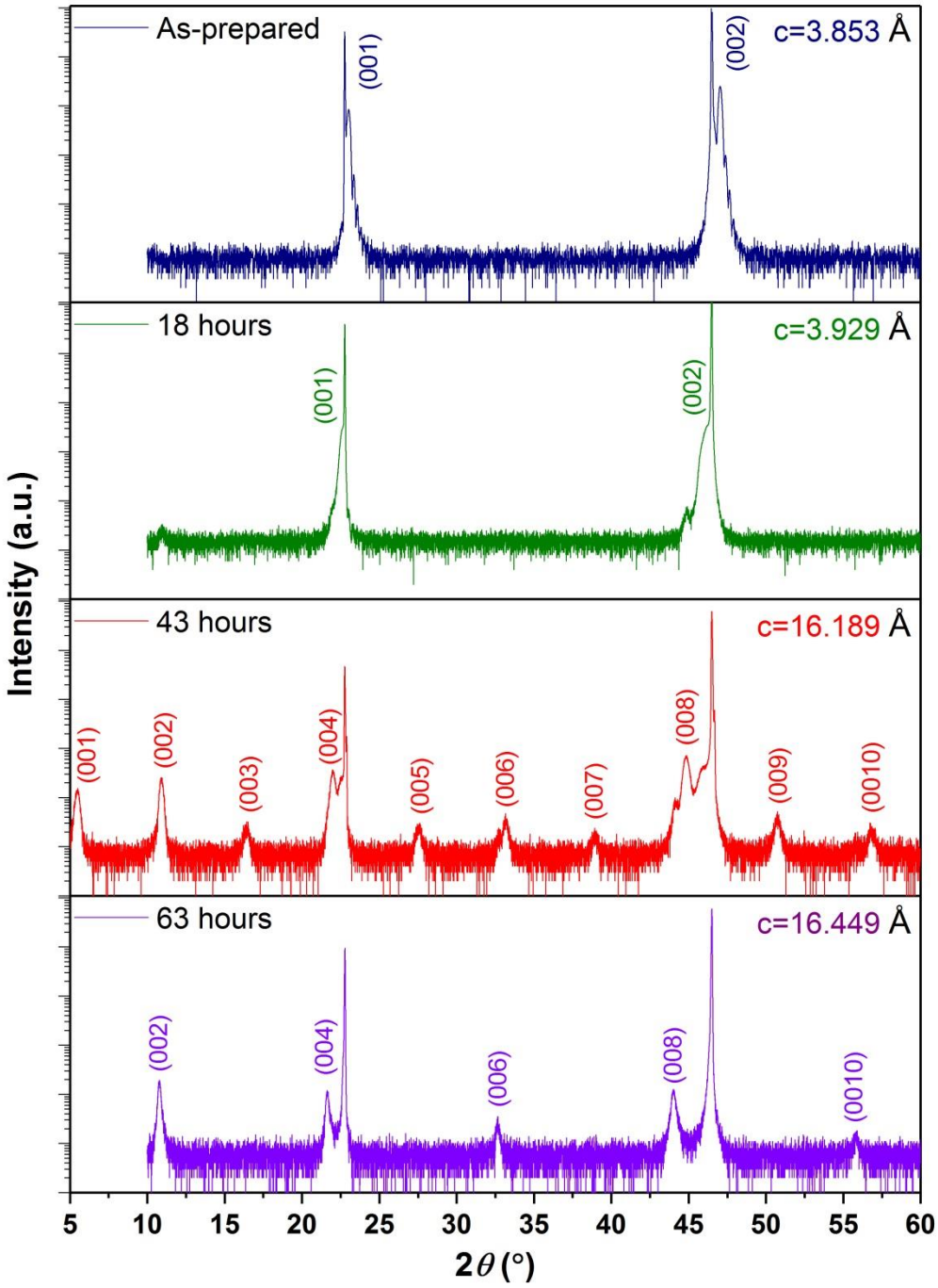

Figure 5.10: Full range diffraction patterns for different annealing states measured after cooling down to room temperature without breaking the vacuum. The XRD curves are plotted in logarithmic scale. An intermediate phase with a non-centered structure is evidenced at 43 hours (red curve).

Interestingly, an intermediate phase with a non-centered crystal structure is evident for the first time to our knowledge in LSMO films during the structural evolution from PV to BM, considering the full range XRD scans measured at 43 hours (**Figure 5.10** red curve). At this intermediate annealing state, the oxygen vacancies start to order and a superstructure is formed. Its out-of-plane unit cell size accounts to four times the size of the initial PV-LSMO. However, all the odd reflections from the superlattice are not forbidden, indicating a lower symmetry state in comparison to the latter formed BM phase which has a higher symmetry *C2/c* space group [89–93]. Neither a centered lattice, nor glide planes, is yet formed in consideration of corresponding extinction rules, suggesting that the observed phase does not belong to any known BM variants [94,95].

Remarkably, the PV reflections from the expanded lattice do not vanish when the intermediate phase emerges. With further annealing, the intensity of odd superlattice peaks decreases together with the initial PV peak, suggesting that the transformation to the final BM structure already occurs during the transformation to the intermediate phase. This hints toward the intermediate phase being in a metastable state.

With further annealing up to 120 hours, no other Bragg diffraction peaks become visible (data not shown), hence the BM phase being the final one. As the peak position does not shift with any further annealing, we infer that the oxygen stoichiometry cannot be further reduced. The oxygen loss process terminates at an oxygen composition of $La_{0.7}Sr_{0.3}MnO_{2.5.}$

Here we would like to note that the full XRD scans are very important for the investigation of the intermediate phase, the ordering structure, and the transition mechanisms, since we can extract information from more peaks. However, real-time full XRD scans are not possible in our case.

Due to the large thickness difference between the substrate and the film, the intensity of the film peak will be three orders of magnitude lower than the substrate. Hence all the presented XRD curves are plotted in logarithmic scale. For XRD scans focused on a small region around the (002) Bragg peak (**Figure 5.6** and **Figure 5.9**), nice data with enough resolution already takes one hour, in which only 5° in 2θ is covered. If one

planned to cover the full 2θ range (e.g. 60°) with the same resolution, this will require synchrotron experiments.

In addition, one finds from **Figure 5.10** that the intensity of the superlattice peak is even two orders of magnitudes smaller than the initial perovskite (002) Bragg peak, which makes the situation even worse. Therefore it is not possible to perform real-time full scans during the transition.

To solve this problem, another route to perform a full XRD scan is adopted. The real-time scans in a small region around the (002) peak are performed instead to monitor the structural evolution, and then the annealing process at some specific point is stopped in order to perform a deeper investigation. The sample is cooled down to room temperature and a time consuming full XRD scan is performed without breaking the vacuum.

By this route, enough time is gained to perform a full XRD scan because the structural changes are frozen. In addition, we can avoid the overlapping of peaks caused by the shift of peaks during the measurement. Moreover, if several peaks evolve in the XRD pattern, the order of appearance for such peaks cannot be distinguished. This is another reason why a long time XRD measurement during annealing is not useful. However, this problem can be solved by the measurement at room temperature, since the transition is stopped and the peaks do not shift over time.

5.1.5 Phase diagram

To investigate the temperature dependence of the structural change, a series of annealing experiments have also been performed at other temperatures (450 °C and 600 °C, respectively). **Figure 5.11** shows the in-situ XRD patterns measured at intervals of 1 hour minutes at 450 °C. The lattice expansion speed exhibits a strong dependence on the annealing temperature. The shift of the thin film Bragg peak is significantly faster than the annealing experiment performed at 400 °C, but slower than the annealing

treatment conducted at 500 °C. It takes 18 hours to achieve the same increment of the out-of-plane lattice parameter where only 3 hours are needed at 500 °C.

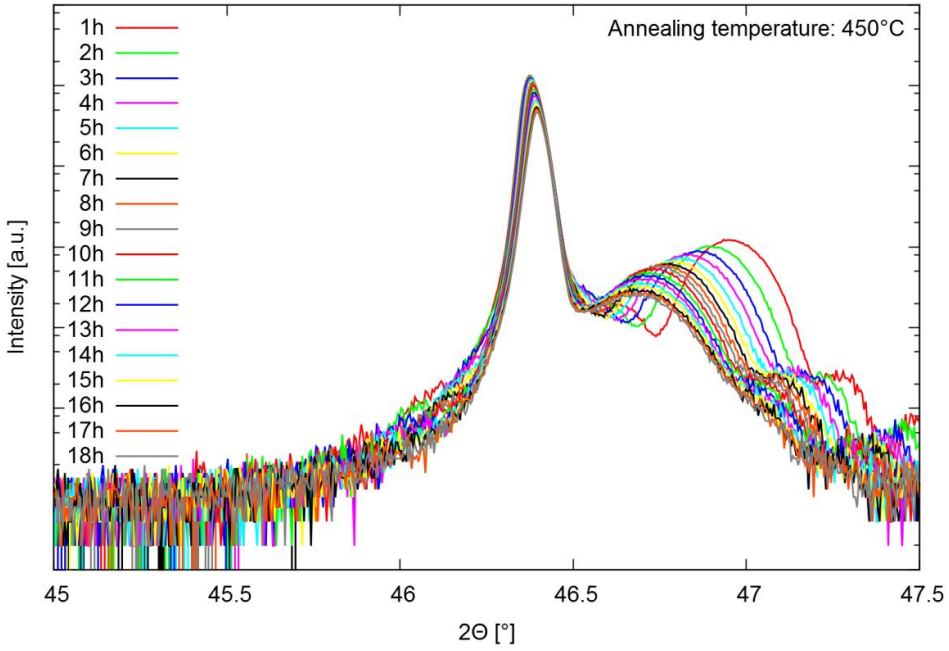

Figure 5.11: In-situ XRD scans recorded at 1 hour intervals during vacuum annealing at 450 °C of a 45 nm $La_{0.7}Sr_{0.3}MnO_{3-\delta}$ film on a $SrTiO_3$ (001) substrate. All XRD curves are plotted in logarithmic scale.

Increasing the annealing temperature to 600 °C, the structural evolution becomes faster and the film peak shifts across the substrate peak within one hour. **Figure 5.12** shows the in-situ XRD patterns measured at intervals of 10 minutes at 600 °C. Due to the shorter exposure time in comparison to the measurements performed at lower temperature, the resolution of the XRD data is lower. The entire phase conversion time from perovskite to brownmillerite is reduced to 5 hours.

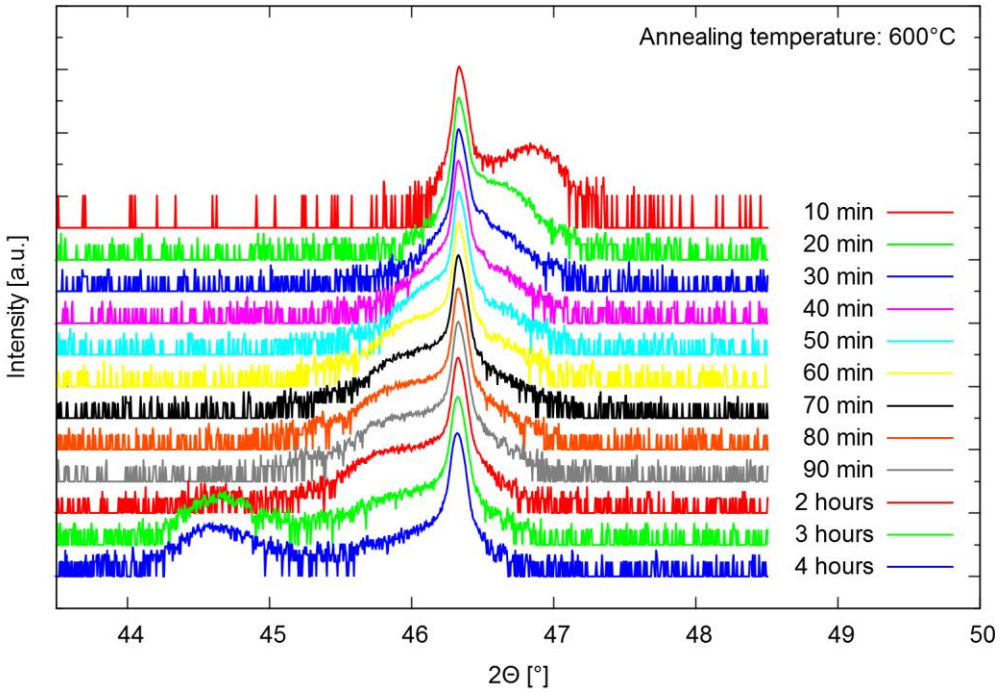

Figure 5.12: In-situ XRD scans recorded at 10 minutes intervals during vacuum annealing at 600 °C of a 45 nm $La_{0.7}Sr_{0.3}MnO_{3-\delta}$ film on a $SrTiO_3$ (001) substrate. For clarity, not all data are shown. All XRD curves are plotted in logarithmic scale.

With the data collected at various annealing temperatures, a phase diagram of the epitaxial LSMO thin film can be constructed according to the transformation from perovskite to brownmillerite, as shown in **Figure 5.13**. The transition speed exhibits a strong dependence on the annealing temperature and annealing time. Below 300 °C, the Bragg peak of the film does not shift with increasing annealing time, which indicates no oxygen desorption occurring. The PV phase is stable in both high vacuum and ambient atmosphere. At 400 °C, a gradual shift of LSMO Bragg peak induced by the oxygen desorption is observed, but nearly 15 times slower than what we observed at 500 °C, as indicated by the shadow area in the figure. Increasing the annealing temperature, the oxygen loss within the film is accelerated and a phase transition from

PV structure to BM structure is identified. At 600 °C, the phase transition speed becomes faster so that the film peak shifts across the substrate peak within one hour. The entire transformation takes only 5 hours being significantly faster compared to other studies [16,83,96,97].

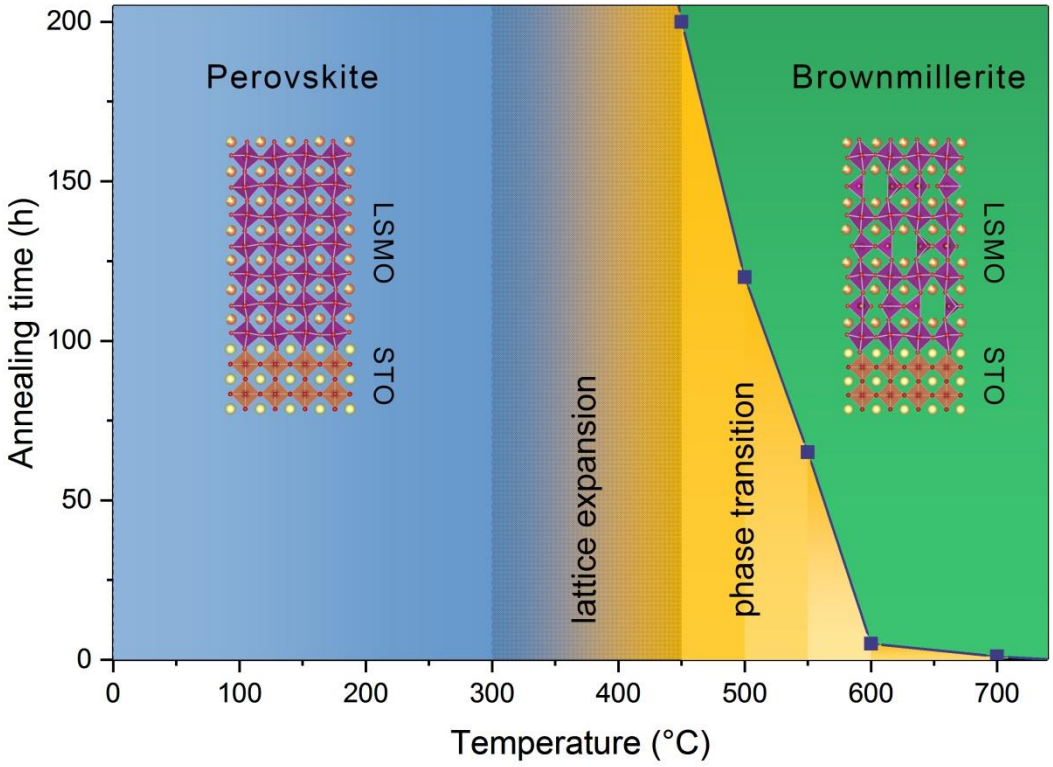

Figure 5.13: Phase diagram of the epitaxial LSMO thin film in dependence of the annealing time and the annealing temperature. Insets are the crystal structures of PV and BM phase drawn using the VESTA software, respectively [22,23]. Below 300 °C, the PV structure is stable, as marked by blue area in the phase diagram. Above this temperature, the lattice expansion caused by oxygen desorption is observed, as marked by the shadow area. With increasing the temperature for post-annealing treatments, a phase transition from PV phase to BM phase occurs. The yellow region in the phase diagram indicates the transformation with coexistence of both phases. Eventually a stable BM structure is formed after annealing for a certain time, where the region is marked by green.

Up to now a direct synthesis of a brownmillerite structure in LSMO thin films has not been reported. Other methods to induce a phase transition from perovskite to brownmillerite in a LSMO film comprise capping with an oxygen getter or by electron beam irradiation [9,88,98]. The former method requires an additional deposition during growth at even higher temperatures, and the latter one is only feasible for small areas of TEM samples. Compared with these methods, a vacancy driven transition induced by our post-annealing treatment is much easier to implement. This approach can be performed directly after sample preparation. Consequently, LSMO represents a good candidate as it shows both structures (perovskite and brownmillerite), and hence such kind of heterostructures can be realized within one single material.

5.2 Magnetic and electric transport properties

5.2.1 Macroscopic magnetization

In LSMO, the magnetic and electrical properties are governed by the exchange interaction between the Mn ion spins, i.e. the super exchange (SE) and the double exchange (DE) [18,99]. **Figure 5.14** shows the temperature dependent magnetization curves for various annealing states. For the as-prepared state, $La_{0.7}Sr_{0.3}MnO_3$ has charge fluctuations of Mn^{3+}–O–Mn^{4+} in the system. Thus the DE mechanism leads to a ferromagnetic (FM) coupling, where a large Curie temperature (T_C) of 342 K is observed. As discussed in the previous chapter, this value is close to the reported value, indicating a correct stoichiometry after sputtering deposition.

For oxygen deficient states in the first few hours of annealing, the properties are influenced by the change of Mn valence state, resulting from the increasing number of oxygen vacancies. Considering the charge balance in the whole film, the nominal manganese valence state is reduced and the Mn^{3+} valence state becomes more abundant, resulting in a decrease in ferromagnetism. The suppressed T_c indicates a deterioration of the perfect perovskite structure and hence of the DE paths by vacancies.

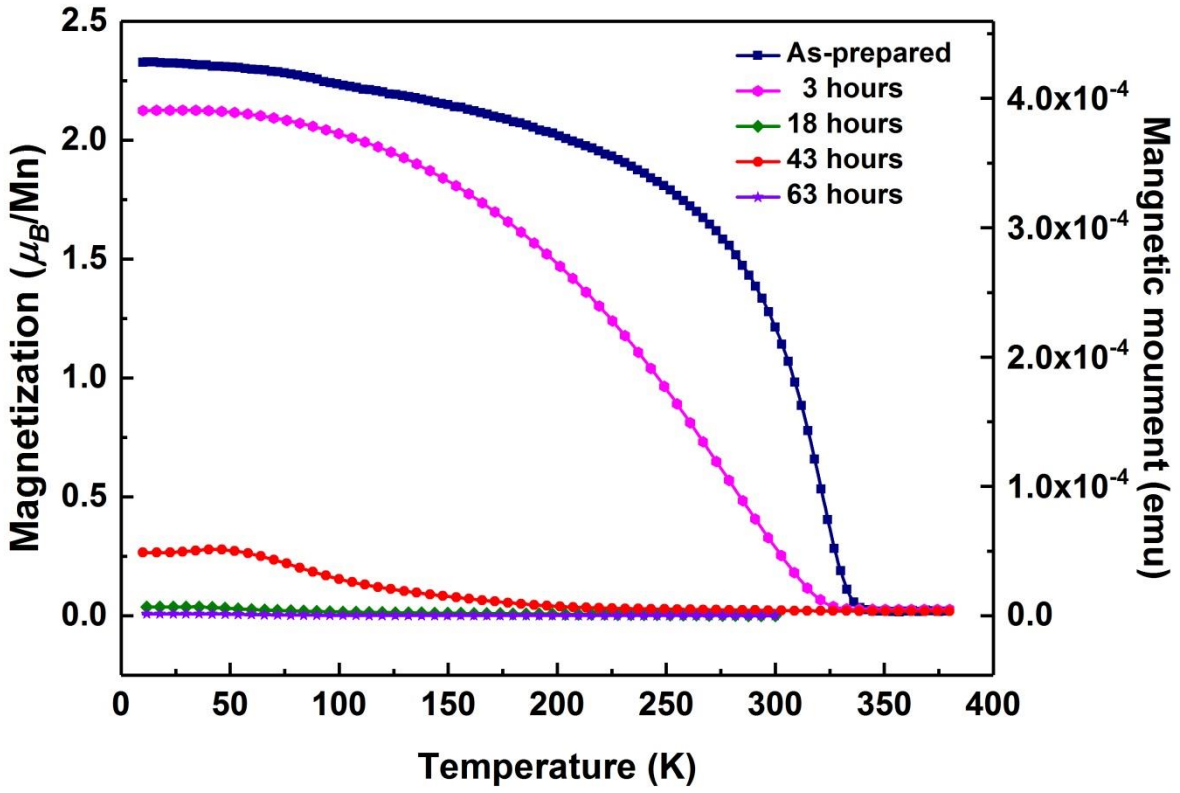

Figure 5.14: Temperature dependence (*T*) of normalized magnetization (*M*) measured for LSMO films at various annealing states. The measurement were performed upon field cooling (FC) at a magnetic field of 0.01 T. The conversion to unit (μ_B/Mn) has large systematic due to the number of Mn atoms. A second y-axis with units taken directly from the measurement is added on the right. For the as-prepared state, the $SrTiO_3$ phase transition is visible at 105 K, while the similar feature is not observed for the other annealing states. This indicates that structural phase transition for $SrTiO_3$ (from a high temperature cubic phase to a lower temperature tetragonal phase) is suppressed in an interface region due to the change in oxygen content.

With increasing annealing time, the material should only contain Mn^{3+} ions at some point. This point is probably around 18 hours of annealing. Here we observed a sharper peak in the FC curve, compared with the latter formed $Mn^{2+/3+}$ phases, as shown in **Figure 5.15**. This is an evidence that at this state, a stronger SE interaction exists, thus supporting a Mn^{3+}-Mn^{3+} combination. From the view of stoichiometry, if the material has

only Mn^{3+} ions, the stoichiometry should be $La_{0.7}Sr_{0.3}MnO_{2.85,}$ given the possible formation of $La_{0.7}Sr_{0.3}MnO_{3-\delta}$ (δ=0.15).

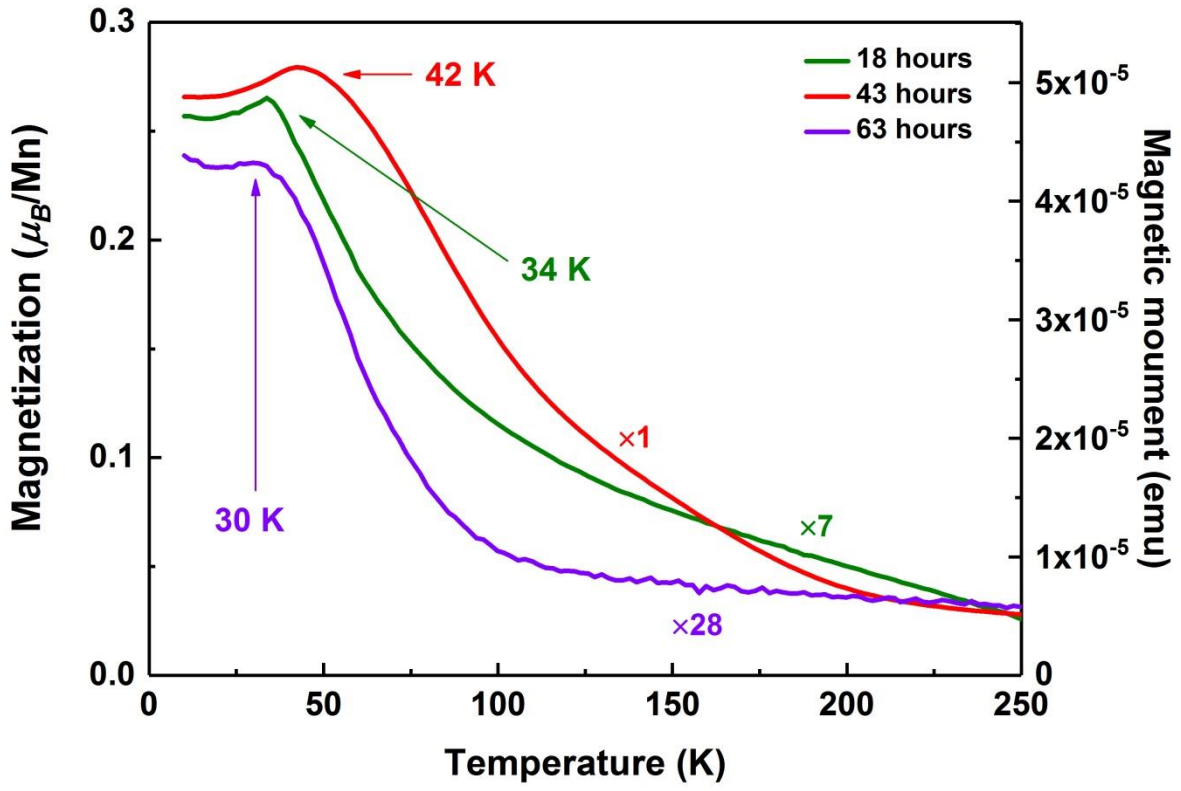

Figure 5.15: Detailed *M-T* curves for three highly oxygen deficient states. For the sake of visibility, the magnetization for 18 hours and 63 hours are multiplied by 7 and 28, respectively. The critical temperatures are marked by arrows. The measurement were performed upon field cooling (FC) at a magnetic field of 0.01 T.

Continuing the annealing till 43 hours, the $La_{0.7}Sr_{0.3}MnO_{3-\delta}$ film transforms into the intermediate state with a vacancy-ordered superstructure as confirmed by diffraction measurements. A striking feature is that the magnetization increases, and an antiferromagnetic (AFM) order is adopted with a corresponding Néel temperature (T_N) at 42 K. This magnetic behavior clearly indicates the formation of a new intermediate

phase. However the magnetization is surprisingly high for an AFM state. Therefore it is possible that a small FM component or canted AFM state exists. With further annealing until the final BM phase is formed, the T_N shifts to 30 K in contrast to the former intermediate state.

Figure 5.16 displays the hysteresis loops measured at 10 K for various annealing states. For the as-prepared state, the sharp hysteresis loop is consistent with the observed high T_c in the field cooling curve, indicative of a high quality of single-crystalline LSMO film with large domains. For the final state with a BM structure, the hysteresis loop measured at 10 K reveals zero coercive field, consistent with an AFM order, suggesting a pure phase without any FM remnants.

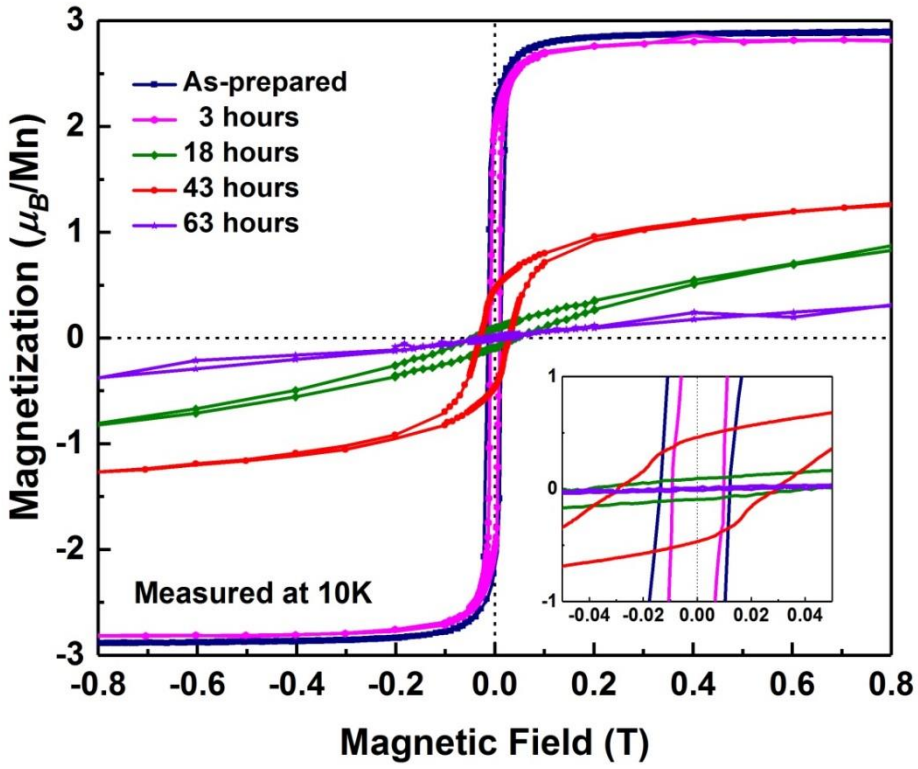

Figure 5.16: Hysteresis loops measured at 10 K with the magnetic field (*H*) applied in-plane for various annealing states. The inset shows a magnification of the corresponding *M*-*H* curves around the origin.

Here we also need to note that a magnetic hysteresis loop is observed for the intermediate state after annealing for 43 hours, as shown in the red curve. This effect can be attributed to a two-phase region or canted AFM state. As discussed in the XRD measurements, the initial PV peaks are still visible at 43 hours of annealing. Therefore a minor FM feature from the PV phase might be still detectable. On the other hand, as only one transition is observed in **Figure 5.15**, a weak FM signal from the canted AFM state is also possible. In addition, the enhanced coercivity observed in the intermediate state can then be attributed to the pining of magnetic domains by the nonferromagnetic regions in the film.

5.2.2 Resistivity influenced by oxygen content

In perovskite-type transition metal oxides, the electric transport properties are demonstrated to be very sensitive to the oxygen off-stoichiometry. In order to further investigate the electronic transport properties of LSMO, we characterized the temperature dependent resistivity for the distinctive oxygen deficient $La_{0.7}Sr_{0.3}MnO_{3-\delta}$ phases.

The temperature variation of the resistivity of the LSMO films at zero field and 9 T are presented in **Figure 5.17**. For the as-prepared LSMO film, a half-metallic nature is observed. Due to the dominant DE interactions, it exhibits a transition from a high temperature paramagnetic semi-conducting or insulating phase to a low temperature FM conducting phase, which is known as metal–insulator transition [27,49]. The transition temperature peaks at the Curie temperature, T_c. At low temperatures $T < T_c$, the spontaneous alignment of the Mn spins below T_c, allows a delocalization of the e_g electrons according to the DE mechanism, leading to a low resistivities ferromagnetic phase.

However the resistivity of different annealing states strongly increases on the gradual desorption of oxygen. This enhancement in resistivity arises from the strong electronic correlations in perovskite manganites. In agreement with the increasing lattice parameter, the extension of the Mn-O-Mn bond length is expected during oxygen

desorption, which results in a reduction of orbital overlap and favoring of electron localization. If the separation of Mn atoms increases more and more, the gain in kinetic energy due to the hopping will not win over the penalty in potential energy associated with the on-site Coulomb repulsion. Combined with the valence change of Mn ions induced by oxygen vacancies, a strong suppression of conductivity is observed at the oxygen deficient states.

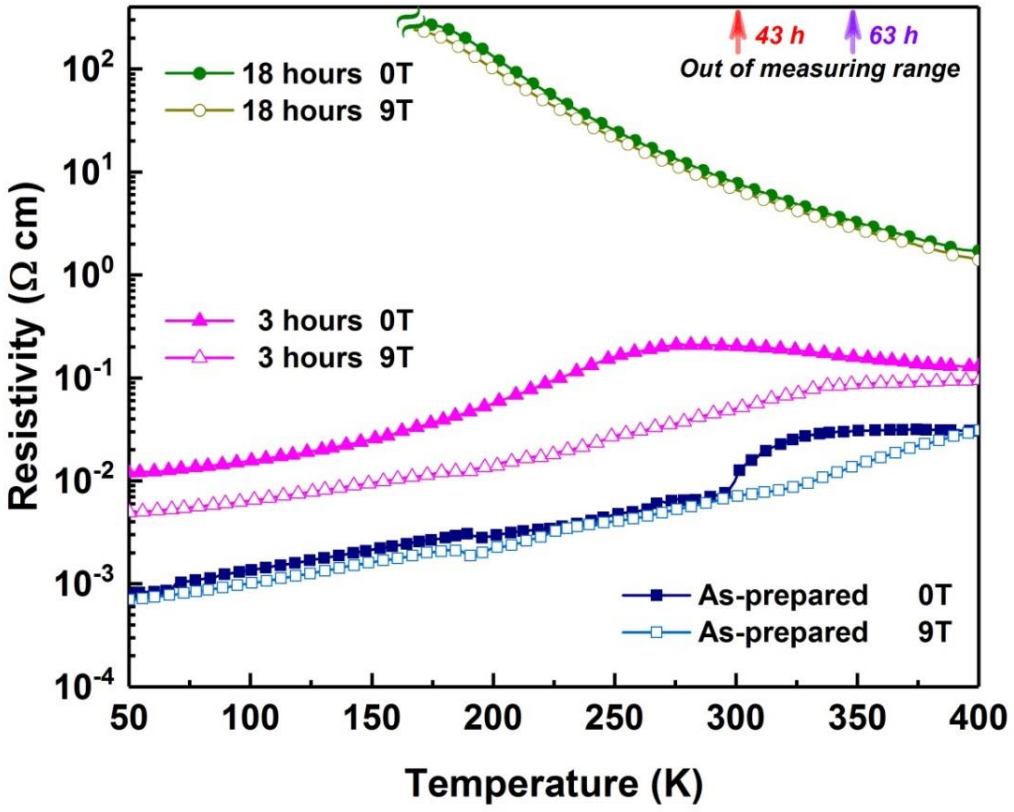

Figure 5.17: Temperature-dependent resistivity measured for LSMO films at various annealing states at zero field (solid symbols) and an in-plane magnetic field of 9 T (open symbols). A dramatic increase of resistivity upon oxygen desorption is evidenced. With further annealing for more than 18 hours, the resistance values exceed the measurement limit of10 MΩ, corresponding to upper limit of 10^3 Ω cm in the resistivity.

After 18 hours of annealing, an increase of three orders of magnitude of the resistivity is observed at room temperature in comparison to the as-prepared state. Increasing the heating time to more than 43 hours, the resistance of the film even exceeds the limit of the instrument and becomes too large for our measurement equipment.

In another aspect, the prevalence of the antiferromagnetic order in the $Mn^{2+/3+}$ systems can be explained by the observation of insulating behavior. According to the Goodenough-Kanamouri rules, [34–36] $Mn^{2+/3+}$ phases could have mixtures of antiferromagnetic and ferromagnetic couplings, similar to $Mn^{3+/4+}$ materials. However, the ferromagnetism is generally accompanied by metallic conductivity. This coupled metallic-ferromagnetic behavior is generally attributed to the DE mechanism, as the ferromagnetic alignment of Mn spins needs the presence of itinerant conduction electrons to take part in the DE exchange [37,91]. Since all the topotactically reduced LSMO are insulators, the localized valence electrons are unable to participate in DE interaction. Therefore the antiferromagnetic order is more favored rather than the ferromagnetic order in these materials.

5.2.3 Magnetoresistance influenced by oxygen content

Manganites have a large negative magnetoresistance, the so-called colossal magnetoresistance (CMR). By applying an external magnetic field, tunable CMR is found, as shown in **Figure 5.18**. The maximum CMR effect is obtained close to T_c for all the annealing states. The CMR effect also follows the same trend as the suppression of T_c. A large CMR effect of more than 80 % is observed in a minor oxygen deficient state (annealed for 3 h). Here one should note that the observed broadening of the temperature dependent response could be favorable for applications. These results clearly suggest a dramatic sensitivity of magnetotransport properties on oxygen content variation in epitaxial LSMO films.

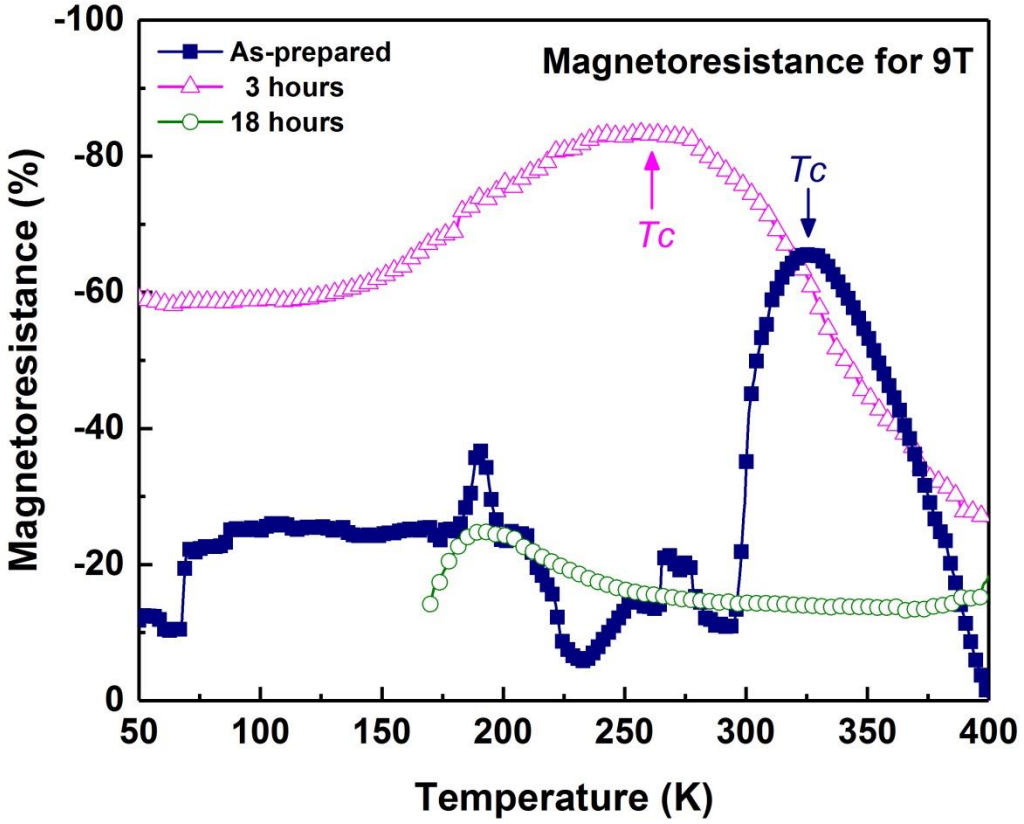

Figure 5.18: The temperature-dependent magnetoresistance ratio between 9T and 0T for the corresponding annealing states. With oxygen release, the maximum colossal magnetoresistance effect is found to shift towards lower temperatures, accompanied by a broadening of the metal-insulator transition.

5.2.4 Reversible switching of physical properties

We realized the reversible switching realized between the BM and PV structure. By tempering the sample in an oxygen atmosphere, the oxygen composition can be cycled between oxygen deficient and a stoichiometric state.

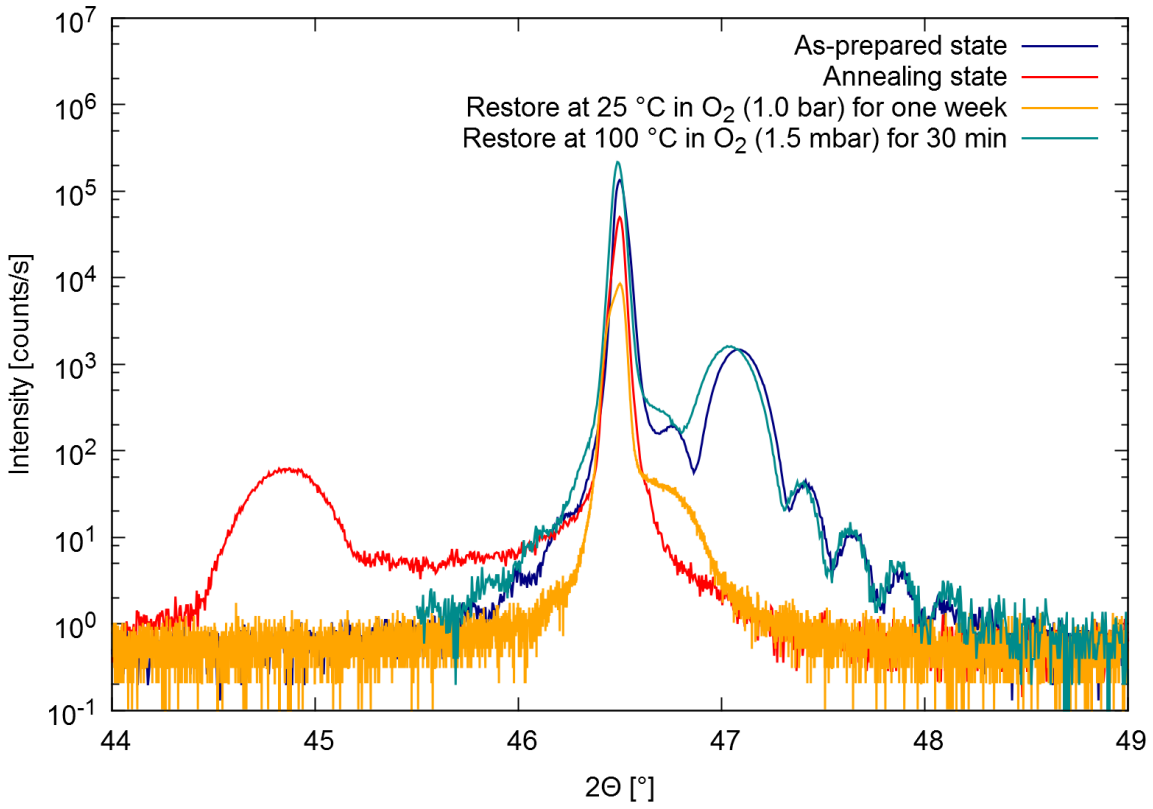

Figure 5.19: XRD ω-2θ scans around the (002) Bragg peaks of a 45 nm $La_{0.7}Sr_{0.3}MnO_{3-\delta}$ film on a $SrTiO_3$ (001) substrate at various states. The patterns are shifted for clarity. The XRD patterns of the as-prepared state (PV-LSMO) and annealed state (BM-LSMO) are denoted with blue and red lines as indicated, respectively. The XRD patterns of two restored states after annealing in oxygen atmosphere at 25 °C and 100 °C are denoted with yellow and light blue lines as indicated, respectively.

The XRD patterns of the restored systems are shown in **Figure 5.19,** in comparison to the experimental results for the as-prepared state and annealing state. The (002) Bragg peak of the as-prepared LSMO film can be seen at a higher two theta value than the sharp (002) Bragg peak from the STO substrate with Kiessig thickness fringes clearly visible. After annealing, a structural transformation from PV to BM is induced as

discussed in the previous text. The (008) Bragg peak of a BM superlattice evolves on the left hand side of the STO peak, as shown as the red curve.

A reverse transformation from BM to PV can be achieved by annealing the sample in oxygen atmosphere. The restoring treatment at 25 °C was performed at a larger oxygen partial pressure of 1.0 bar. The PV peak is restored at the right hand side of the STO peak (yellow curve). During this transformation, the oxygen atoms incorporate and diffuse into the LSMO film. The additional oxygen disorders the BM structure and a cubic PV phase forms. The superlattice of alternating oxygen tetrahedral and octahedral layers is replaced by disordered vacancies. However this conversion is slow and takes long time, i.e. in the order of one week. We can infer that 25 °C is already cutting the border of the phase transition but not all the oxygen atoms are at the correct sites in the PV structure. When we increase the annealing temperature to 100 °C, the oxygen incorporation is significantly accelerated. Not only the phase transition is faster (30 min), but also the requirement of the oxygen pressure is reduced to 1.5 mbar. Under such conditions, the quality of the film is fully restored as the thickness fringes become visible again.

We can assume that there is an energy threshold to accelerate such a dynamic process. Similar effects have been seen in bulk $SrCo_{0.8}Fe_{0.2}O_{2.53}$ above a critical oxygen partial pressure, but the oxygen is incorporated into the phase between the temperatures of 600 and 743°C [50]. In analogy, both, the temperature and the oxygen partial pressure need to be taken into account in the restoration of the film from BM to PV.

In combination with properties characterization, the ferromagnetism and metallic properties are restored as well. The temperature-dependent resistivity for as-prepared LSMO films and reversed systems are compared in **Figure 5.20**. After reloading the oxygen at 25 °C at an oxygen partial pressure of 1.0 bar, the sample turns to conductive again with the analogous shape of resistivity curve compared to the as-prepared state. Furthermore, the critical temperature of the metal-insulator transition for the restored LSMO film becomes identical to the as-prepared state while annealing at 100 °C in oxygen atmosphere, suggesting a complete restoration process.

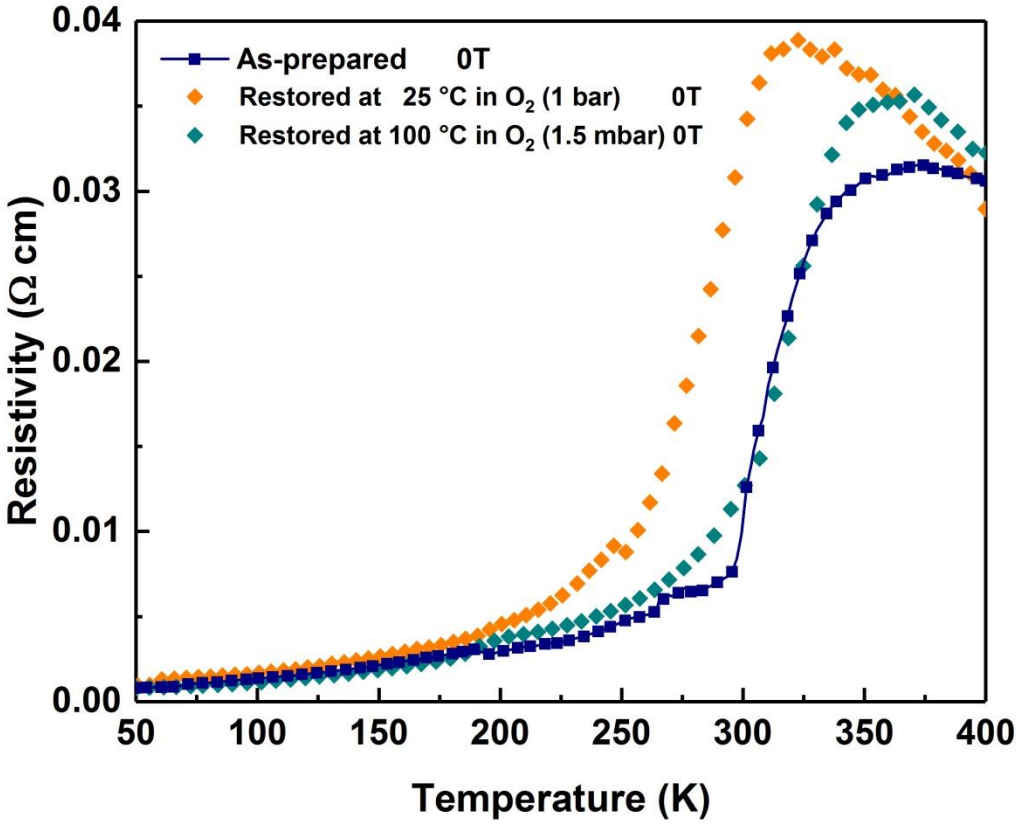

Figure 5.20: Temperature-dependent resistivity measured for as-prepared LSMO films and restored systems measured at zero field. The temperature-dependent resistivities of the reversed systems are depicted without lines, where a clear restoration of metallic behavior is observed at100 °C.

Figure 5.21 shows the field cooling curves and hysteresis loops measured for as-prepared LSMO films and restored systems. Both the Curie temperature and the shape of the hysteresis loops are restored after annealing at 100 °C in 1.5 mbar of O_2. Therefore a fast (30min) and low temperatures (below 100°C) restoration of epitaxiality, ferromagnetism, and the CMR effect is achieved in LSMO thin films which could be of technological relevance.

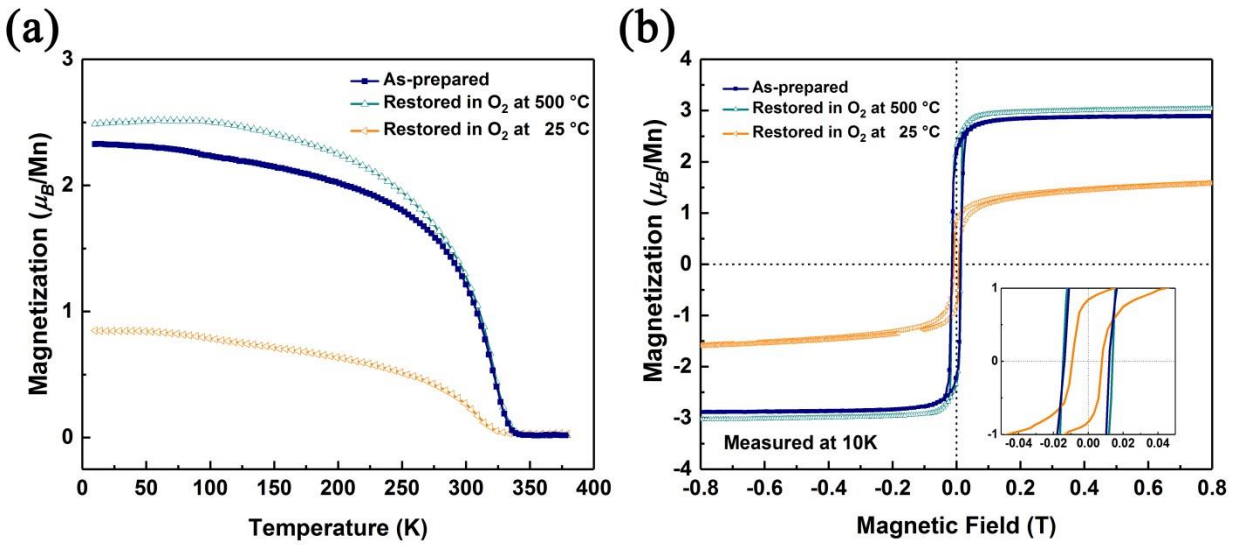

Figure 5.21: (a) Temperature dependence (*T*) of the normalized magnetization (*M*) measured for as-prepared LSMO films and restored systems. The *M-T* curve of as-prepared state is denoted with solid symbols. The *M-T* curves of the restored systems are denoted with open symbols. (b) Hysteresis loops measured at 10 K with the magnetic field (*H*) applied in-plane for as-prepared LSMO films and restored systems. The inset shows a magnification of the corresponding *M-H* curves around the origin.

Compared with other reported oxides like $SrCoO_{2.5}$ and $SrFeO_{2.5}$, which also show a similar phase conversion, the Gibbs free-energy of the PV structure is lower than that of the BM structure in magnetite [83]. This is why in LSMO films the PV structure is always stable and the direct synthesis of the BM LSMO film is still viewed as a great challenge. In other transition metal oxides such as $SrCoO_x$, the Gibbs free-energy shows an opposite trend, resulting in an easy formation of the BM structure, while the PV phase is always very hard to obtain. Therefore different material systems have different tendencies for the transition direction, depending on the multivalent transition metal. LSMO can thus be viewed as an excellent complementary model to conventional material systems.

5.3 Stoichiometry change after post-annealing

5.3.1 Stoichiometry determination of LSMO films by RBS spectrometry

The stoichiometry was checked by RBS spectrometry after the post-annealing treatments to make sure the difference is due to oxygen only. The stoichiometry is given in **Figure 5.22** by simulation of the RBS spectrum.

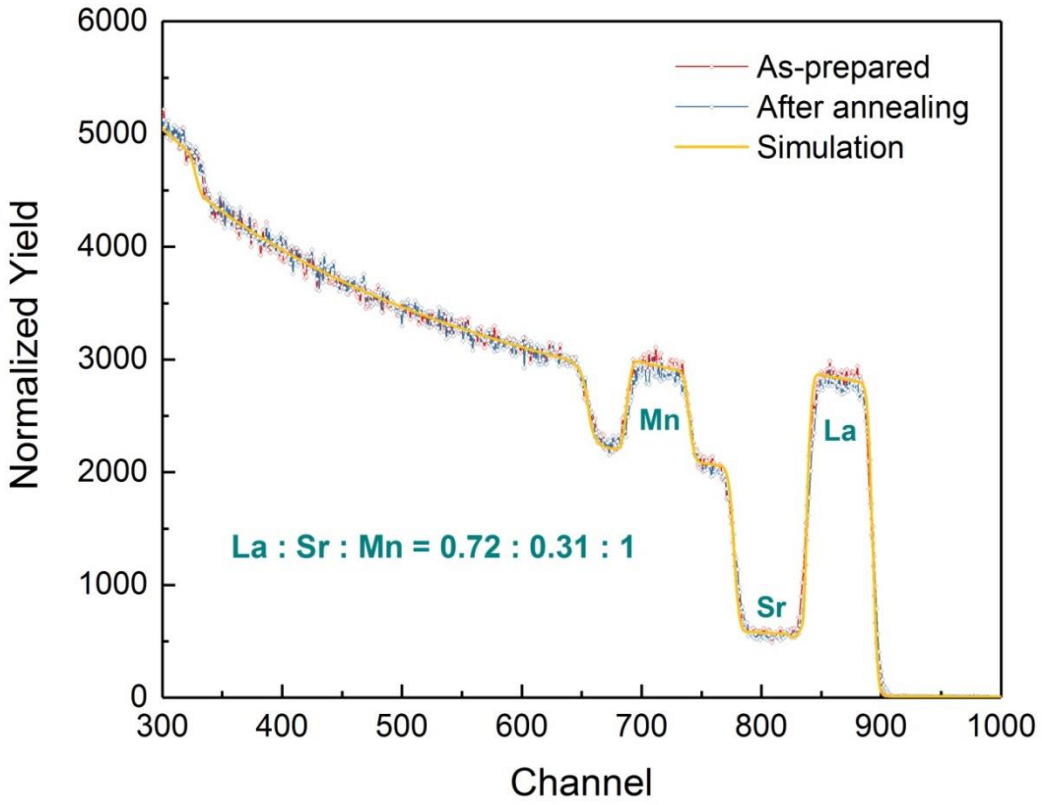

Figure 5.22: RBS analysis of stoichiometry change before and after annealing for a 45 nm $La_{0.7}Sr_{0.3}MnO_{3-\delta}$ film grown on a $SrTiO_3$ (001) substrate. The red and blue curves correspond to the RBS signal obtained from the as-prepared state and annealed state (120 hours) at 500 °C, respectively. The data is simulated by the software RUMP [66,67] under consideration of the thickness and the density of the sample. The simulation result is denoted by the yellow line.

As shown in the figure, there is no obvious difference to the obtained RBS signal measured before and after annealing in vacuum for 120 hours at 500 °C. This suggests that the composition of La, Sr and Mn has not changed during annealing.

Here we need to note that the RBS measurements are not sensitive to oxygen composition, with an error of more than 20 % when determining the oxygen stoichiometry as discussed in the previous chapter. Therefore the oxygen deficiency (or excess) cannot be detected by this method.

5.3.2 Determination of oxygen stoichiometry for LSMO film by PNR

In order to overcome the challenge of the precise determination of oxygen stoichiometry in transition metal oxide thin films, PNR is employed as a promising alternative to measure the oxygen composition.

Figure 5.23 shows the results of the PNR measurements conducted on the sample in the intermediate phase. The measurements were performed at two different temperatures, i.e. 10 K and 150 K, respectively. At a small Q_z range, a larger splitting between R^{++} and R^{--} reflectivities are observed at 10 K. This suggests that the magnetization at low temperatures is larger than at high temperatures, which is consistent with the feature of the field cooling curve measured for the intermediate phase (**Figure 5.15**). Another observation is the disappearance of thickness fringes found in the R^{++} channel measured at 150 K. From the basics of the polarized neutron scattering, the SLD is composed of a nuclear and a magnetic part. The R^{++} channels show the sum of both, the nuclear and the magnetic contribution, while the R^{--} channels show the difference of the nuclear and the magnetic contribution. Thus the results indicate that the sum of NSLD and MSLD from the film happens to be very close to the one of the substrate. This further implies, after subtraction of the MSLD, that a reduction of the NSLD smaller than the value of the STO (3.525×10^{-6} Å^{-2}) is found in the oxygen deficient layer.

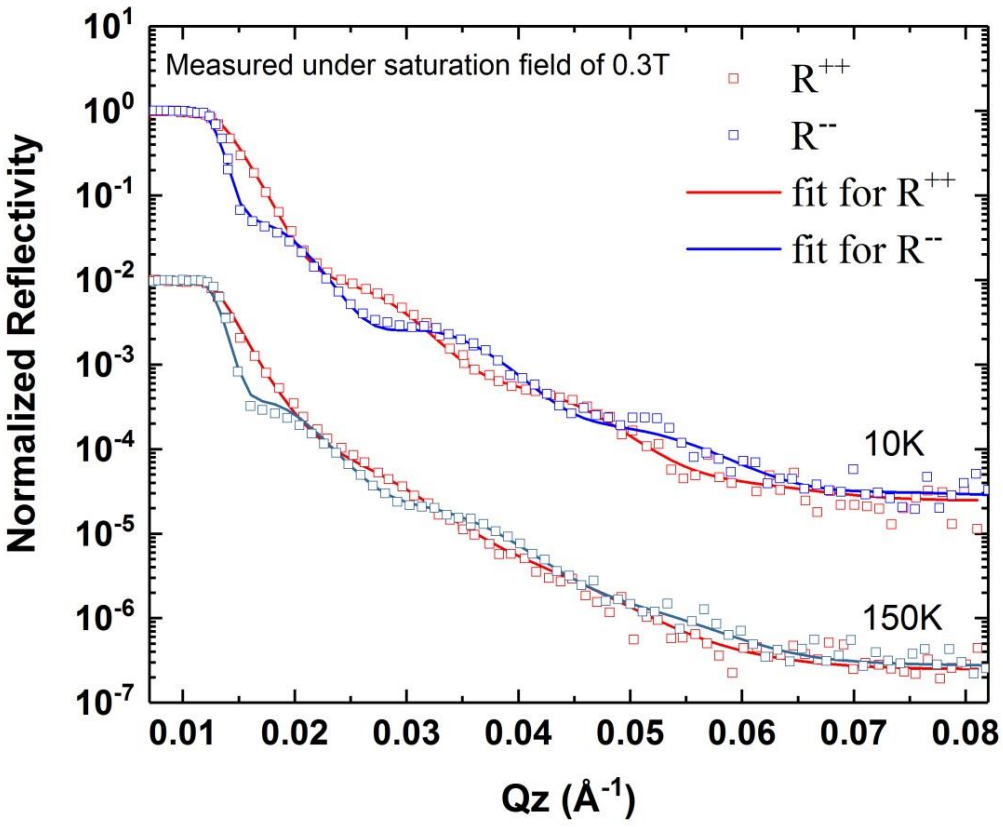

Figure 5.23: PNR measurements of a LSMO film in the intermediate state, observed after 43 hours of annealing. Measured (open symbols) and fitted (solid lines) reflectivity curves for spin up-up (R^{++}) and spin down-down (R^{--}) polarized neutrons are shown as a function of the scattering vector component Q_z. For better visibility, the reflectivities measured at 150 K are divided by a factor of 100.

Figure 5.24 shows the results of NSLD and MSLD obtained from the fit to the PNR data. Quantitative analysis of nuclear and magnetic depth profiles is performed. For a stoichiometric $La_{0.7}Sr_{0.3}MnO_3$ and $La_{0.7}Sr_{0.3}MnO_{2.5}$ sample, the SLD is 3.707 × 10^{-6} Å^{-2} and 2.964 × 10^{-6} Å^{-2}, respectively, from the Inorganic Crystal Structure Database, as indicated by the horizontal dashed lines in the figure. For our samples, the stoichiometry

of other elements was checked by RBS to make sure the difference is only due to oxygen (**Figure 5.22**). Therefore the distinct difference in NSLD for LSMO systems makes it a prospect to resolve variations of the oxygen composition in thin films using polarized neutron reflectometry.

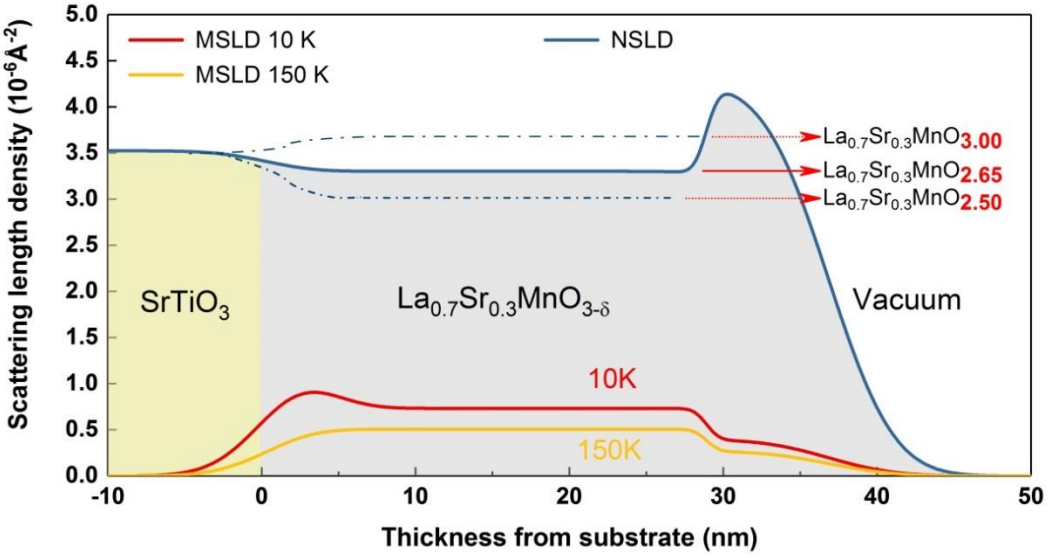

Figure 5.24: Nuclear scattering length density (NSLD) and magnetic scattering length density (MSLD) depth profiles as function of thickness. The contrast in NSLD for three different oxygen stoichiometries is plotted as horizontal dashed lines for comparison.

Here a uniform oxygen deficient phase is found throughout the film. A reduced NSLD due to oxygen loss is further confirmed with its value of $(3.346 \pm 0.012) \times 10^{-6}$ Å^{-2}, corresponding to an oxygen stoichiometry of $La_{0.7}Sr_{0.3}MnO_{2.65}$. Additionally, a top layer with increased NSLD is evidenced as well.

5.3.3 Determination of surface stoichiometry for LSMO film by XPS

In the previous chapter (**Figure 4.3**), the XPS measurements performed at room temperature reveals a surface off-stoichiometry for the as-prepared LSMO thin films. Strontium segregation is observed near the surface of LSMO thin film compared with the RBS results for the entire film. Similar effects have also been reported in LSMO films grown by pulsed laser deposition [76,100,101].

Many studies have revealed an enriched surface phase of $La_{1-x}Sr_xMnO_3$ systems [102,103]. Possible phases that can stabilize on the LSMO surface are e.g. SrO, $SrCO_3$, La_2O_3, and $(La,Sr)_2MnO_4$. However, the origin of the A-site segregation, the structure of the segregated surface, and the temperature and pressure conditions that promote this segregation are still unknown.

In order to identify the structural nature of surface segregation of Sr in LSMO, XPS and STEM were employed as complimentary methods to determine the surface phase in our system.

Figure 5.25 shows the in-situ XPS data measured during annealing at 600°C in a vacuum of 10^{-8} mbar. The sample was heated to 600 °C in ca. 60 min. After reaching 600 °C, the spectra were recorded at 30-120 min intervals. The primary features include the La 3d, Mn 2p, Sr 3d, and O 1s peaks. The content of carbon cannot be quantified due to the overlap of the C 1s and Sr 3p1 peaks. Except for carbon contaminations, no other impurity is detected. Here we need to note that the quantification analysis in atomic ratio has at least 15% relative error, which is normalized to 100 at% with a Shirley-Background and empirical relative sensitivity factors.

Presented in **Figure 5.26** are the annealing time dependent atomic ratios of La, Sr, Mn, and O obtained from the corresponding XPS peaks of La 3d, Sr 3d, Mn 2p, and O 1s. The initial La/Sr ratio measured before annealing is 0.7:0.8, which far beyond the stoichiometry of $La_{0.7}Sr_{0.3}MnO_3$ for the entire film. This is a clear indication that the Sr atoms are abundant at the surface.

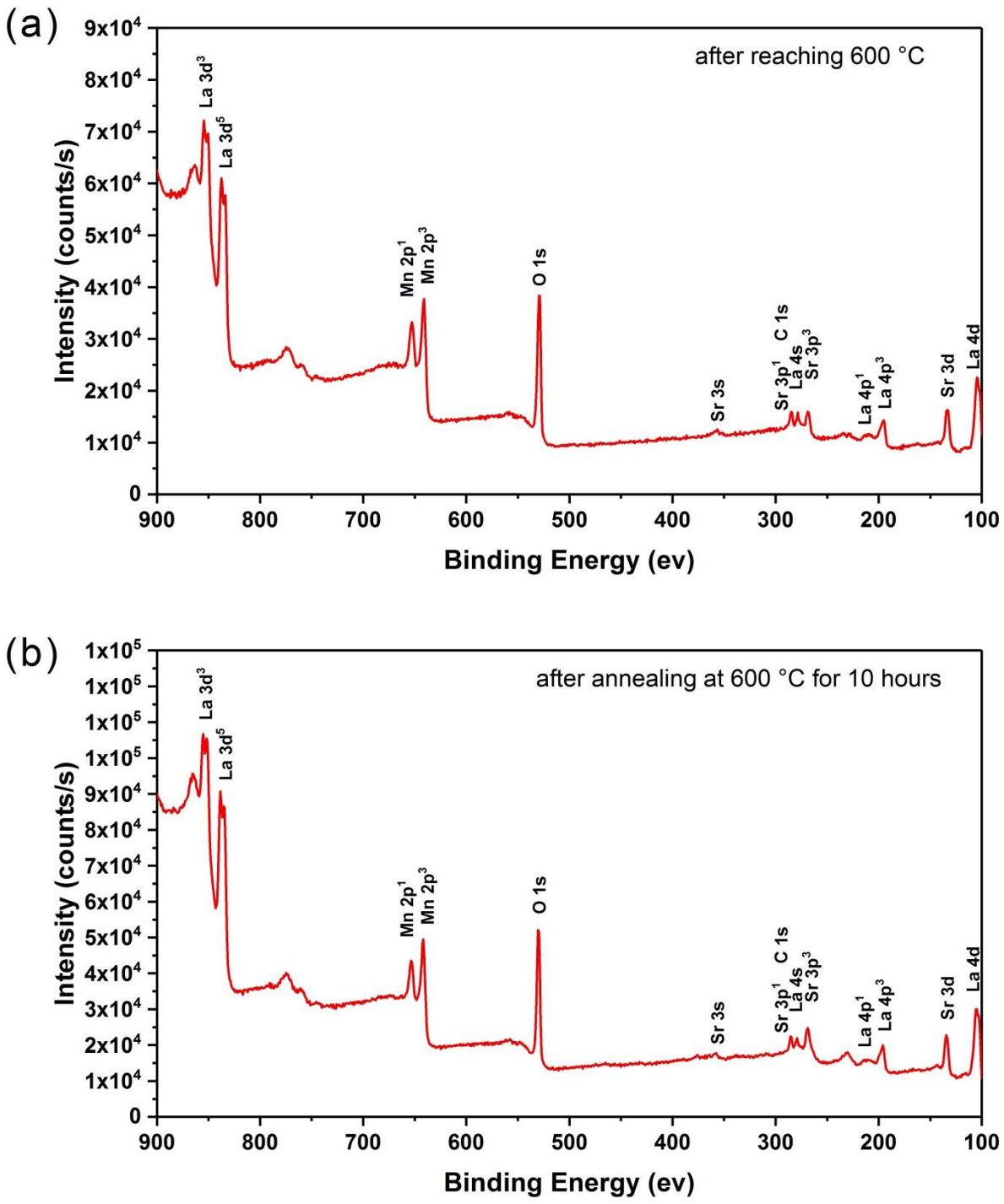

Figure 5.25: In-situ X-ray photoelectron survey scans of $La_{0.7}Sr_{0.3}MnO_3$ film grown on STO substrate. (a) XPS spectrum measured after reaching at 600°C; (b) XPS spectrum measured after annealing at 600°C for 10 hours.

After annealing for 10 hours, the surface La/Sr ratio increase from 0.88 to 1.14, while the Sr/Mn has not changed. Taken the relative error into account, this increase of the La proportion is credible. On the other hand, the decrease of the surface Mn/(La+Sr+Mn) ratio from 0.66 to 0.63 is also found. These effects could be correlated with the variation of the Mn valence state induced by the oxygen vacancies generated during annealing. One can expect that due to oxygen loss from the surface, the Mn oxidation state is changed, as more Mn ions are converted to a lower valence state while annealing.

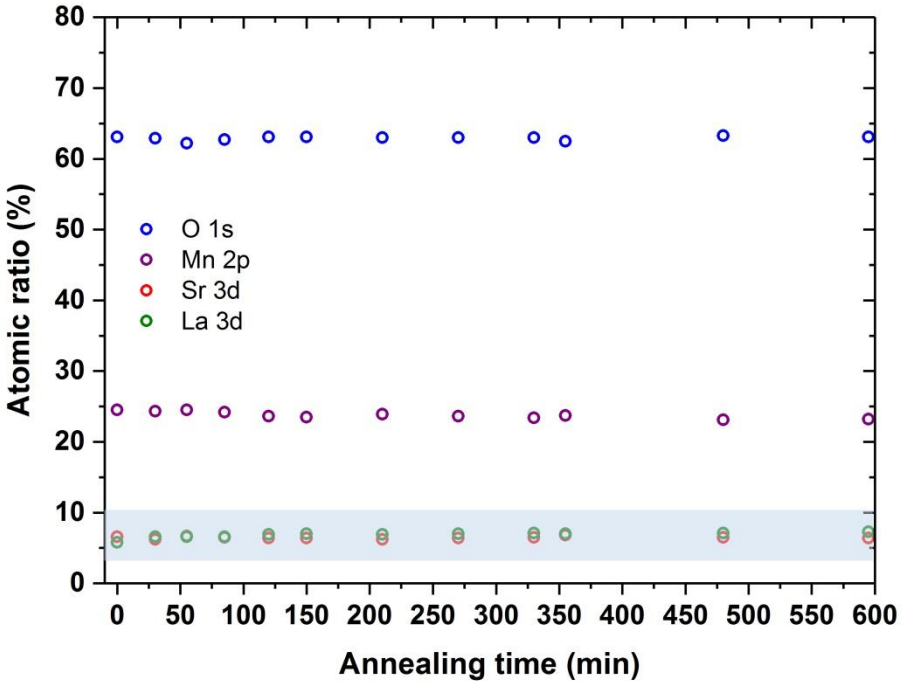

Figure 5.26: Quantified analysis of surface atomic elemental percentage at various annealing time based on the cross-section-normalized intensity from the XPS spectrum. The obtained values of atomic ratio have a relative error of 15 %.

Shown in **Figure 5.27** are the XPS narrow scans focusing on the peaks of the surface oxygen ions. Multiple splitting is found at the O 1s spectra, including three main peaks for all the annealing states. The asymmetric nature of the O 1s peak is attributed to the presence of a number of different chemical environments at the surface. The lower binding energy peak at ca. 539.5 eV is generally assigned to the lattice oxygen components in LSMO [104–109]. The peak at ca. 531.9 eV can be assigned to the adsorbed oxygen species such as carbonate and possibly hydroxide [110–114]. The deconvolution of the O 1s peak shows an intermediate binding energy for the third peak. Similar O 1s spectra over $La_{1-x}Sr_xMnO_3$ oxides have been also observed by Gunasekaran [115,116]. It is possible that the introduction of oxygen vacancies lead to an increase in the adsorbed/absorbed oxygen concentration at the surface with a distinct peak separation.

After annealing at 600 °C for 10 hours, the intensity of the high-energy component (~532.2 eV) for adsorbed oxygen species is attenuated, while the intensity of the intermediate-energy peak (~531.1 eV) for the oxygen vacancies is enhanced. This hints toward the interpretation that the “vacancy” oxygen is increased slightly relative to the ‘‘surface’’ component upon annealing.

The changes in the relative contributions of ‘‘lattice’’, “vacancy” and ‘‘surface’’ components are more distinct in the atomic ratio, as shown in the **Figure 5.27** (c) and (d). The corresponding amount of different oxygen species are compared as a function of annealing time. The atomic ratio of adsorbed oxygen species decreases, while oxygen vacancy components increase with annealing. This indicates that at the active surface area, the adsorbed oxygen atoms are captured by carbon oxidation or react with other oxygen atoms. The resultant O_2 or CO_2 can then desorb from the surface, leading to an increase of the ratio of oxygen vacancies in the film. Concurrently, the atom ratio of “lattice” oxygen components decrease with increasing annealing time, which is consistent with the observation that oxygen desorbs from the lattice during annealing in vacuum.

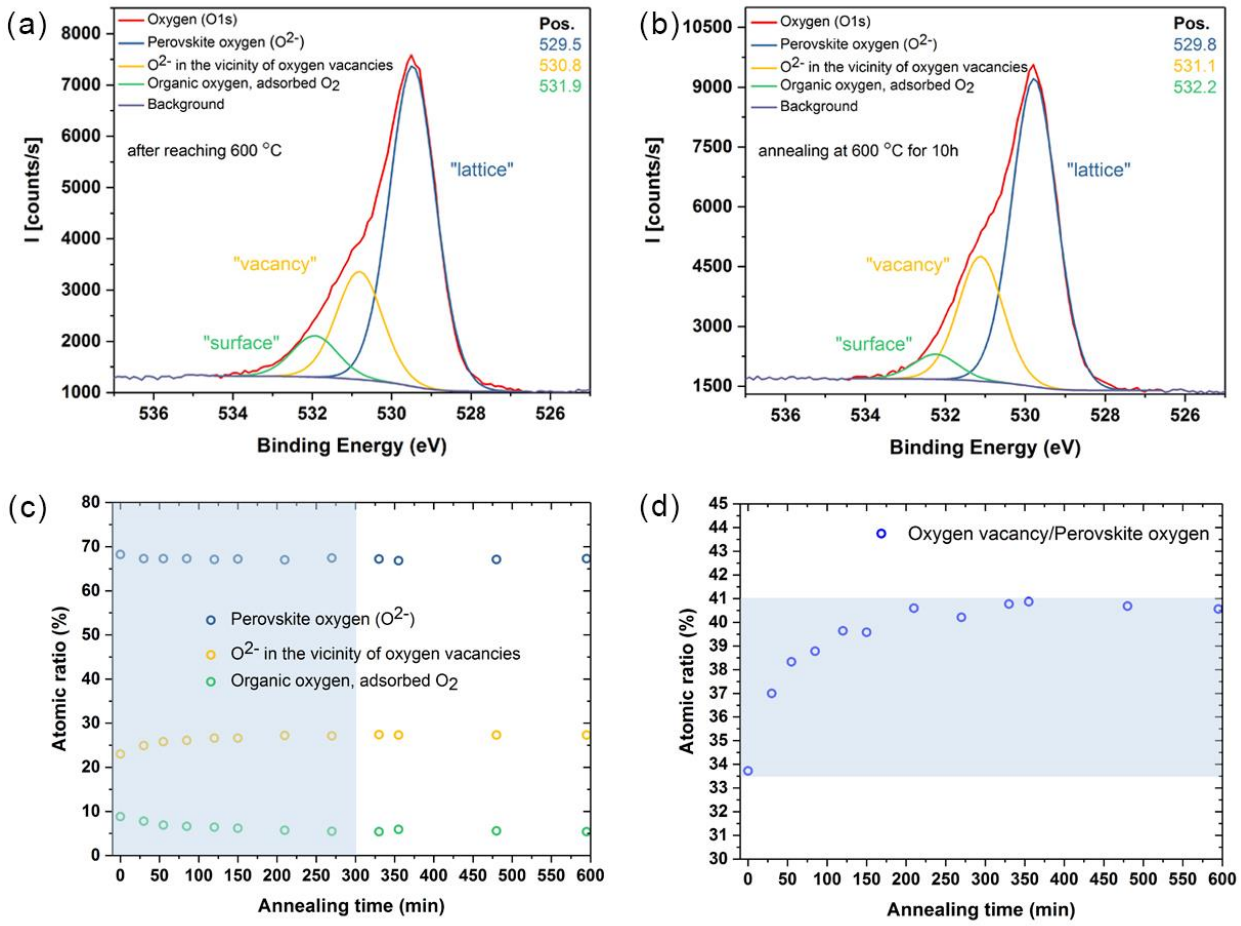

Figure 5.27: (a) In-situ O(1s) XPS spectra of $La_{0.7}Sr_{0.3}MnO_3$ film measured after reaching 600 °C. (b) in-situ O(1s) XPS spectra measured after annealing at 600 °C for 10 hours. (c) Quantified analysis of the surface atomic ratio for different oxygen species at various annealing times. (d) Time-dependent atomic ratio of vacancy oxygen over perovskite lattic oxygen.

After 4 hours of annealing, the atomic ratio of vacancy oxygen over perovskite lattice oxygen reaches a plateau, suggesting that the oxygen cannot be further reduced in the film. This time scale is in a good agreement with the real-time XRD results measured at the same annealing temperature (**Figure 5.12**). At this point, the final BM phase is formed, where the oxygen loss process terminates at an oxygen composition of $La_{0.7}Sr_{0.3}MnO_{2.5}$.

5.3.4 Structural determination of the surface phase in LSMO

As discussed in the XPS measurements, the surface La/Sr ratio reaches 0.7:0.797 due to Sr enrichment, which is far away from stoichiometric La/Sr ratio of 0.7:0.3. The observed stoichiometry at the surface is close to the Ruddlesden-Popper phase of $La_{0.7}Sr_{0.8}MnO_{3.5,}$ which exists in bulk LSMO. Both XRR and PNR measurements for the annealing states reveals a top layer with increased NSLD, which does not belong to a PV phase of LSMO. The increased NSLD is found 10~15 nm beneath the surface.

To elucidate the crystal structure of the surface phases in more detail, scanning transmission electron microscopy (STEM) was conducted using high-angle annular dark field (HAADF) contrast and annular bright-field (ABF) contrast, respectively. The sample selected for the STEM measurement was post-annealed in vacuum at 600 °C for more than 5 hours to achieve the same annealing state. The cross sections in Figure 5.28 are taken in the region 10~15 nm from the film surface. The cross-sectional STEM specimens are prepared in the form of a thin lamella using focused ion beam (FIB) milling and a lift-out method.

Figure 5.28 (a) shows the HAADF images along the [110] zone axis of the LSMO film. In this imaging mode, the intensity of atomic columns is approximately proportional to Z^2, [117,118] where Z is the atomic number (i.e. bright contrast indicates La/Sr columns, fainter contrast denotes Mn), and columns containing oxygen hardly contribute to the image intensity. In the image, a shift of La/Sr atoms is found along the out-of-plane direction in every three La/Sr columns. The lattice thus shows additional stacking of shifted octahedra, which also exhibits a larger unit cell than the PV structure. In the ABF imaging mode, an identical periodic sublattice is also observed. In this mode, the contrast shows a smaller dependence on the atomic number Z, approximately as $\sim Z^{1/3}$. Compared to HAADF, the resulting images enable one to visualize the light element columns [119,120].

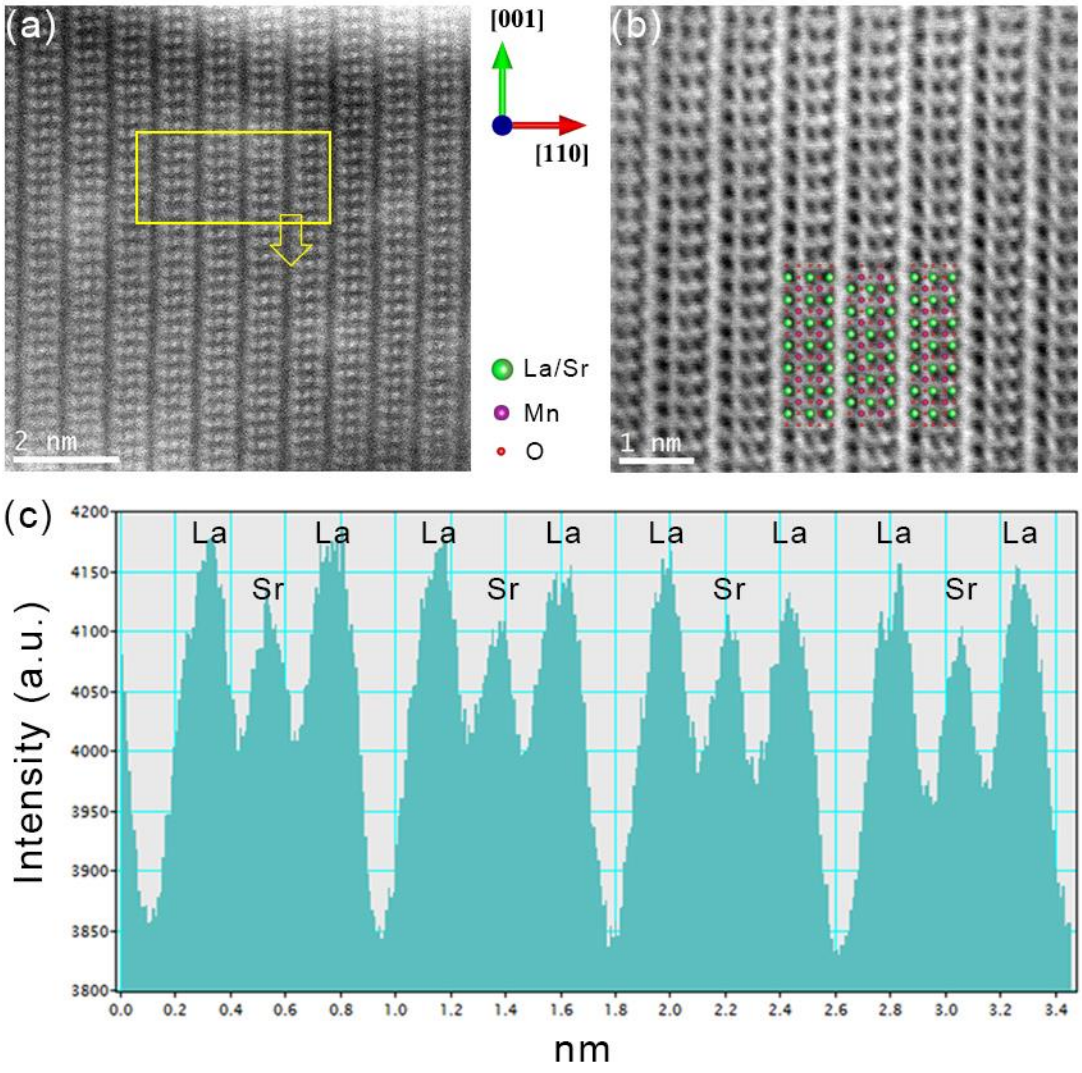

Figure 5.28: (a) HAADF image of the surface regime of the LSMO film. (b) ABF image of the surface regime of the LSMO film. The images were recorded along the [110] zone axis with respect to the LSMO film. The upward vector is along the out-of-plane direction of the film. (c) HAADF line-scan of the intensity of neighboring atomic columns.

On the other hand, a cation ordering of this structure type is observed in LSMO film, as shown in **Figure 5.28** (c). In the line profile of the neighboring A-site cation columns, the La cations and Sr cations are not randomly distributed, which is facilitated by the stacking sequence of LaO-SrO-LaO-LaO-SrO-LaO. However it is still unclear whether it

is formed during the annealing process or whether it already existed in the as-prepared state. Thus further investigations on the surface structure for the other annealing states needs to be done.

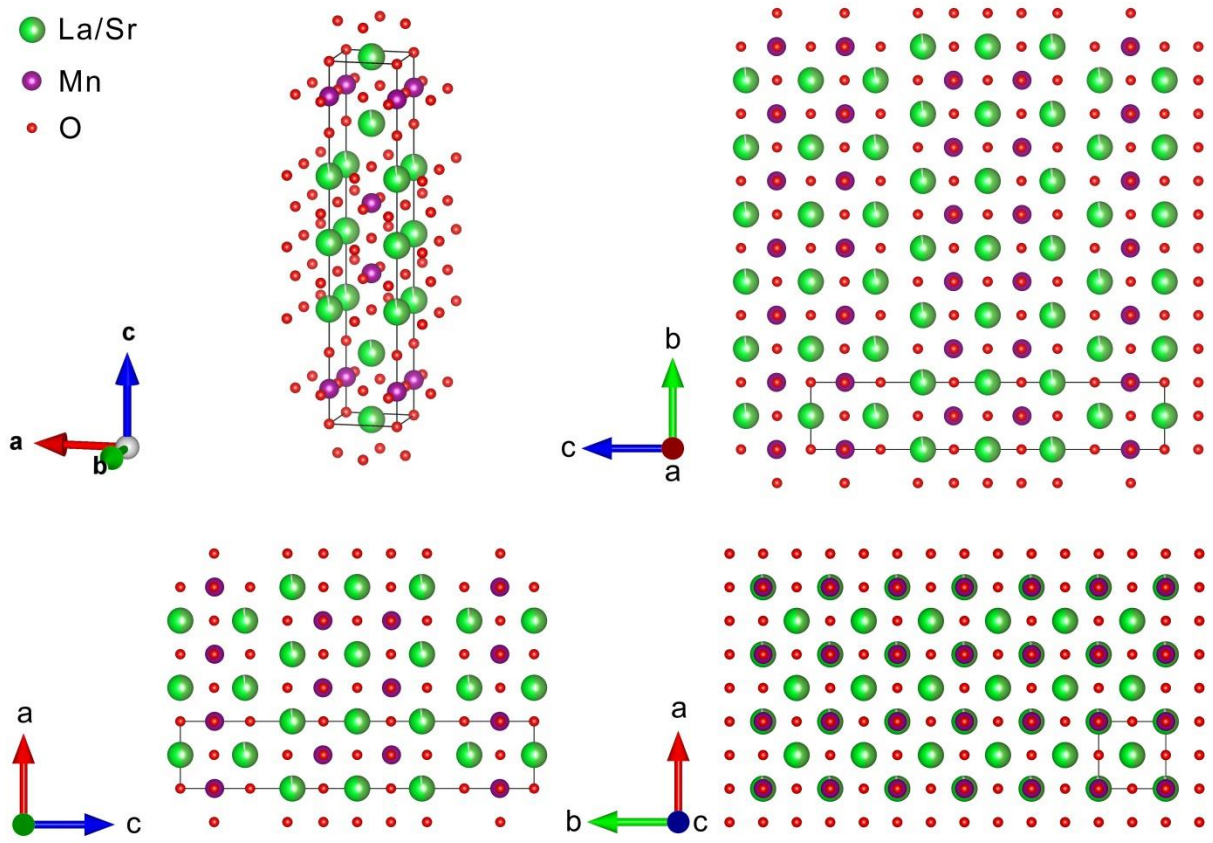

Figure 5.29: Crystal structure of $La_{0.7}Sr_{0.8}MnO_{3.5}$ ($La_{1.4}Sr_{1.6}Mn_2O_7$) with Ruddlesden-Popper phase. The space group is I 4/m m m (No. 139). The projections from three different viewing directions (100), (010), (001) are shown, respectively. The general formula of Ruddlesden-Popper phases is $A_{n+1}B_nO_{3n+1}$, where A and B are cations, O is the oxygen anion, and n is the number of the layers of octahedra in the perovskite-like stack [121–124]. In our case, n=2. The single unit cell is denoted with solid lines. The figure is drawn using the VESTA software [22,23].

Figure 5.29 shows the crystal structure of the Ruddlesden-Popper phase $La_{0.7}Sr_{0.8}MnO_{3.5.}$ The configurations of A-site cations show very good agreement with

the observed structure at the surface. The distance between neighboring atoms corresponds well to the results by STEM. In addition, the atomic ratio of La/Sr is consistent with the XPS results, as discussed above. Thus the presence of a surface Ruddlesden-Popper phase seems confirmed at the surface of the LSMO film. Considering the size of the unit cell adopted, the structure type corresponds to n=2. The ideal stoichiometry of an n=2 Ruddlesden-Popper phase is $A_3B_2O_7$, where the structure contains two ABO_3 perovskite layers that alternate with single AO rock-salt layers. Ruddlesden–Popper phases are considered as promising candidates for cathode materials in intermediate temperature solid oxide fuel cells as they can exhibit high mixed oxide-ion and electronic conductivities [125–133]. Our findings demonstrate that LSMO can be considered as a novel model system for studying how Ruddlesden–Popper phases are formed and tailored after preparation.

5.4 Summary

In this chapter, a full map between the dynamic control of the oxygen content and the correlated physical properties is achieved. This is essential for the design of oxides based artificial materials. In multivalent transition metal oxides, the oxidation states of transition metals dominate a multitude of physical properties and emergent phenomena. In our study La,Sr-doped manganites (LSMO) were demonstrated to be a new platform for the study of topotactic transitions, where the $Mn^{3+/4+}$ PV phase is transformed to the the BM $Mn^{2+/3+}$ phase by introducing oxygen vacancies.

During the structural evolution, in-situ x-ray measurements directly reveal the transition process. Not only an intermediate phase is observed for the first time, but also the accompanying lattice expansion is characterized quantitatively in real-time.

Furthermore, the LSMO film as pure BM phase is obtained as the final stage of the annealing process. The magnetic and electric properties are characterized for the first time for this stoichiometry, adding further information to the rich phase diagram of LSMO systems.

Also, the reversible switching back from BM to PV in LSMO is a new approach. Not only the temperature, but also the oxygen partial pressure needs to be taken into account in the restoration of the film from BM to PV. A restoration of ferromagnetism and metallic properties is achieved at room temperature in 1.0 bar of O_2 within one week. A strikingly good crystal quality nearly identical to the as-grown one is observed in the restored film when the restoration temperature is 100 °C, with an oxygen pressure and conversion time remarkably reduced to 1.5 mbar and 30 min, respectively. This could attract interest in the research of catalysts and oxygen migration related techniques.

In addition, the direct quantitative determination of the oxygen content in a thin film is extremely difficult. Our study provides a very promising approach using polarized neutron scattering to achieve a layer-resolved oxygen stoichiometry map. This provides a new path for the quantification of oxygen vacancies in thin film systems. Thus a full map of the structure-property relationship in dependence of the oxygen content is drawn at each oxygen deficient state not only qualitatively but also quantitatively.

A Ruddlesden-Popper phase is formed at the surface of the LSMO film, which is evidenced by STEM. XPS measurements show a surface La/Sr ratio close to La:Sr=0.7:0.8. The time dependent oxygen stoichiometry change at the surface show consistent results with the in-situ XRD measurements at the same temperature.

Chapter 6

Design and construction of the controlled oxygen absorption/ desorption chamber

In the previous chapters we have discussed the release of oxygen atoms from LSMO films during post-annealing at a particular temperature and pressure range. By in-situ XRD, we can quantitatively measure the out-of-plane lattice expansion of the films as a function of annealing time. We performed such measurements using a reflectometer and a dedicated vacuum chamber with heating stage and x-ray windows. However, to perform also in-situ measurements of the in-plane lattice parameter, one requires a much more complex setup mounted on a 4-circle X-ray diffractometer. Such a setup needs a heating stage and a specific design of the vacuum chamber for incoming and outgoing x-rays for a much wider range of angles. Such a setup is of large interest but beyond present capabilities. In this chapter we will introduce the design and construction of such an oxide chamber, which will allow us to measure, in-situ, the crystallographic properties by x-ray scattering.

In addition, the release of oxygen atoms from the LSMO film will lead to a pressure change in the vacuum chamber. Since the fraction of the total mass of oxygen atoms in a thin film is much too small to measure accurately, an alternative method is to correlate the oxygen loss with the increase of the oxygen partial pressure in a vacuum system. By the precise measurement of the pressure change during the annealing process, one would be able to quantitatively determine the oxygen loss within the thin film.

6.1 Outline of the oxide chamber

The chamber system is designed to be horizontally-mounted on the goniometer stage of 4-circle X-ray diffractometer, which is shown and described in detail in **Figure 6.1**.

The setup of the chamber system contains: i) an evacuated dome space for high temperature XRD measurements, ii) a pressure gauge, which is used for monitoring the pressure, iii) a turbo pump for pre-pumping to a base pressure of 10^{-5}~10^{-6} mbar, iv) a sample stage with linear motion, which can be heated to 1200 °C, v) an ion pump for further pumping to 10^{-7}~10^{-8} mbar range.

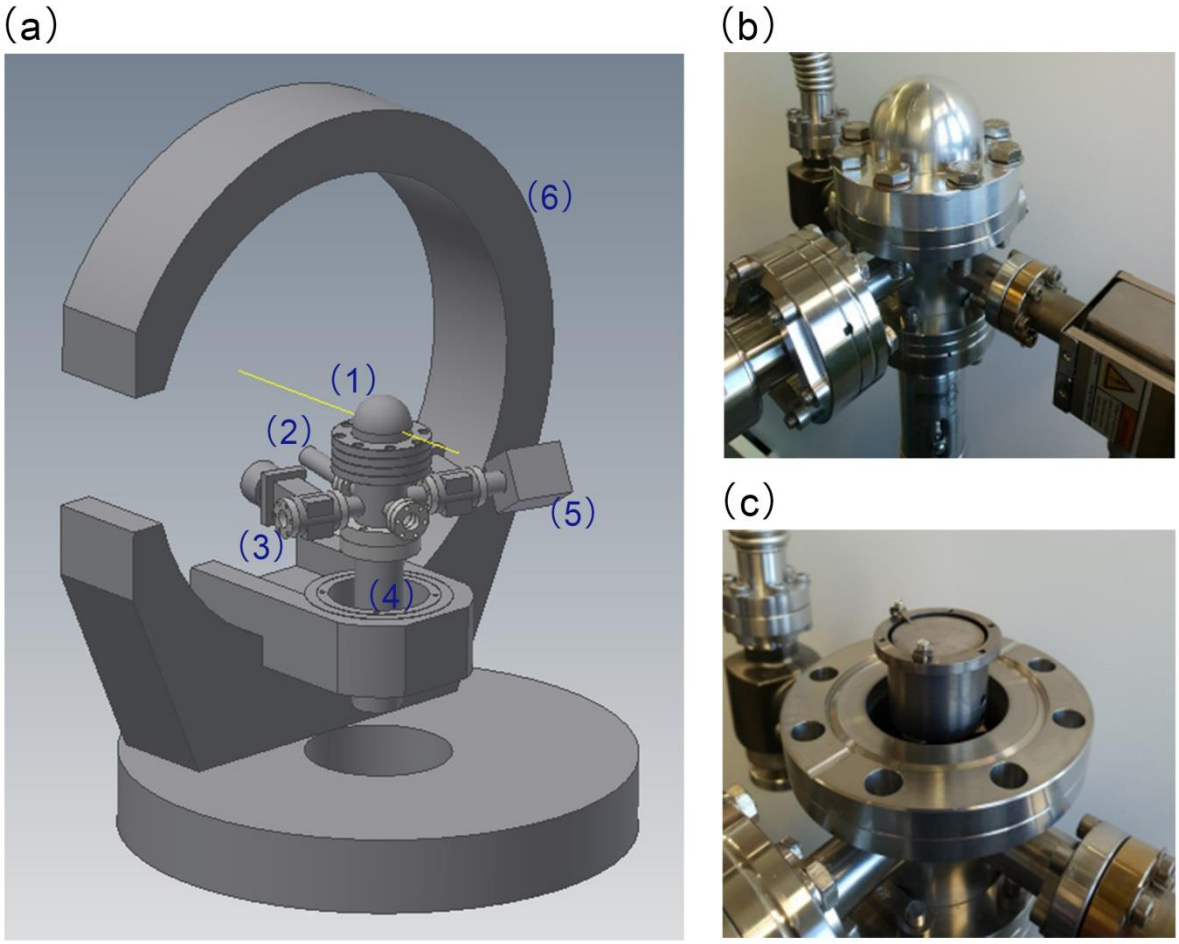

Figure 6.1: (a) A sketch of the complete setup of the dedicated vacuum chamber, showing the chamber attached on the 4-circle X-ray diffractometer. The vacuum chamber is placed on the goniometer stage of the diffractometer. (1) aluminum dome, (2) pressure gauge, (3) connection to the turbo pump through a gatevalve, (4) integrated Z-adjustment and heater, (5) ion pump, (6) arc of the chi-axis. (b) An overview photograph of the chamber with aluminum dome. c) An inner view of the sample holder with heater stage.

As a novel aluminum dome is employed in the chamber system, its performance at ultrahigh vacuum needs to be studied at first. Aluminum has seven orders of magnitude less hydrogen than stainless steel. In addition, it has very low levels of Carbon, resulting in significantly less H_2O, CO, C_2 and CH_4 than stainless steel. The surface properties of aluminum allow full bakeout at 150 °C [134]. A baked aluminum chamber has an outgassing rate of less than 1×10^{-13} Torr liter/sec cm^2 compared to stainless steel, showing 6.3×10^{-11} Torr liter/sec cm^2 [134–136]. Therefore aluminum is demonstrated to be UHV compatible.

On the other hand, the aluminum dome is manufactured together with an aluminum flange from one piece of aluminum bulk. This method is adopted to achieve a perfect dome shape and a clean surface. It can avoid virtual leaks caused by welding, where small volumes of gas or contaminants can be trapped in the pockets at the weld joints.

As is the case for using both aluminum and stainless-steel in one vacuum system, one important point is the sealing between an aluminum flange and a stainless-steel flange. To solve this problem, softer materials are used for the flange system, e.g. silver plated copper gaskets and aluminum gaskets.

In the pumping test after the aluminum dome is assembled, the base pressure of the chamber can reach 10^{-6} mbar only using the turbo pump without bakeout. With further help of the ion pump, the chamber can reach 10^{-8} mbar.

The design of the sample holder inside the chamber is also a challenge due to the limited dimensions on the 4-circle X-ray diffractometer. Before measurement, the position of the thin film sample needs to be aligned in order to move the sample to the center of the x-ray beam. Thus an integrated linear positioner is required to control the height of the sample. During measurements performed on the diffractometer, the rotary phi-axis stage provides an additional degree of freedom to access reflections from different lattice planes. However, it reduces the remaining space for mounting the accessories at the side. Therefore the only plausible solution is to remove the plate of the phi-stage to utilize the bottom space through the rotary O-ring. The diameter of the O-ring hole is 86.10 mm, which is suitable for the linear motion feedthroughs.

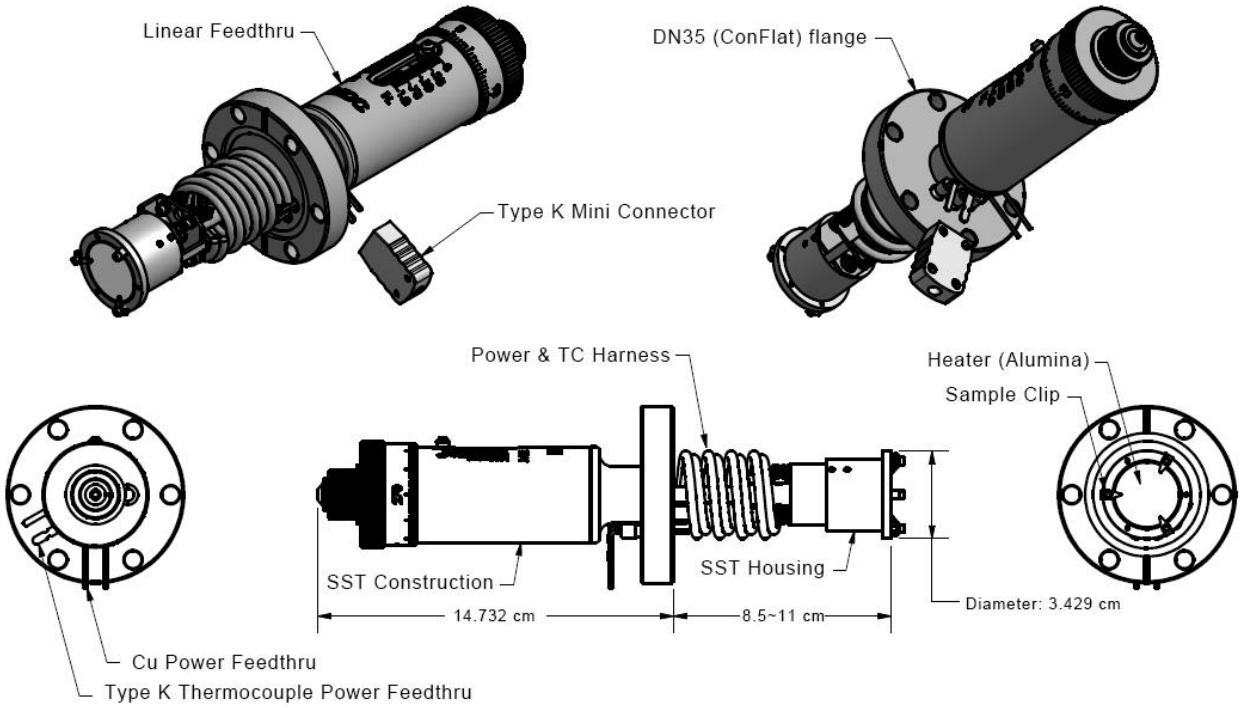

Figure 6.2: Assembly of the sample manipulator with heater stage designed by HeatWave Labs. At the vacuum side, a custom UHV substrate heater is integrated at the end of the linear positioner. The sample height can be adjusted manually. At the air side, a linear scale on the body of the positioner is imprinted in metric units. Linear position is measured along a laser etched black-anodized barrel graduated in 0.025 mm increments. The UHV parts are bakeable to 230 °C with the actuator removed.

Figure 6.2 displays the detailed sketch of the integrated sample manipulator with the heater stage. The heater is capable of 1200 °C operation in UHV. Furthermore, the heater is made of Al_2O_3, which is designed to operate up to 1000 °C in O_2 and other reactive gas environments including air.

In test runs, the samples were annealed in this chamber at temperatures of 700 °C. The aluminum dome is heated up to 60~70 °C due to thermal radiation from the heater. After annealing at 700 °C for 1 hour in a vacuum of 10^{-8} mbar, the Bragg reflections in the out-of-plane direction were checked by ex-situ XRD measurements. The same

transition from PV phase to the BM phase is observed in the LSMO film, as shown in **Figure 6.3**. This demonstrates the successful operation of the heater in vacuum conditions.

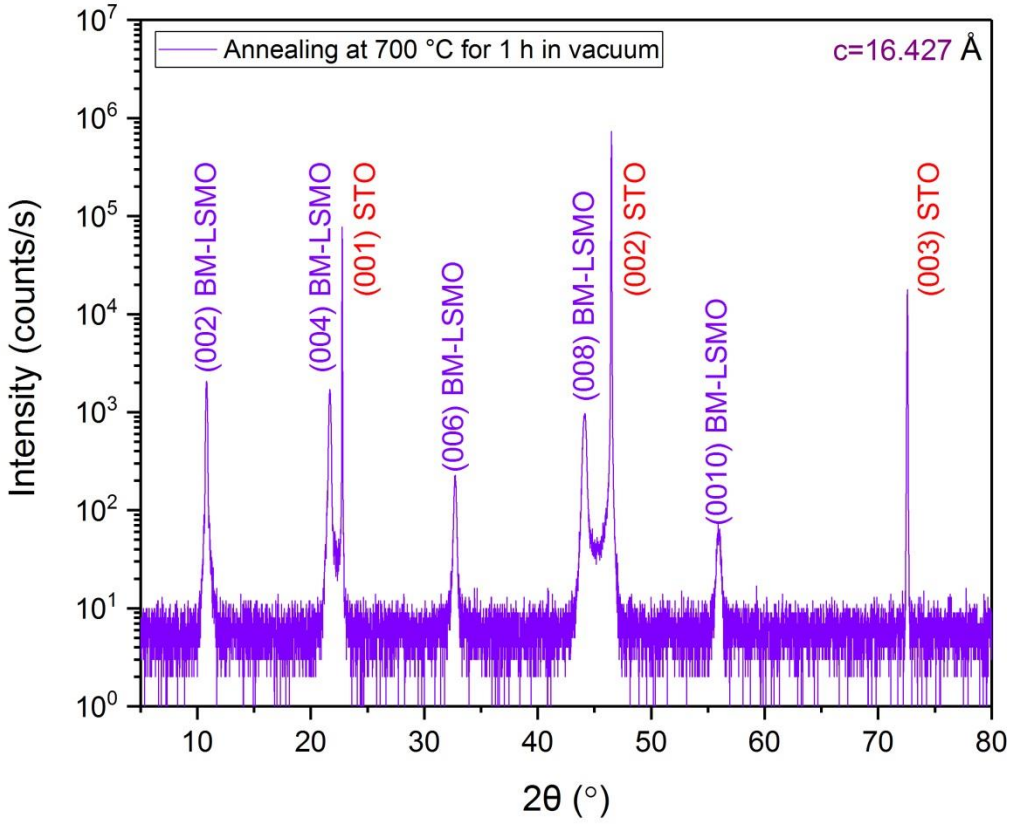

Figure 6.3: Full range diffraction patterns for the LSMO film after annealing in the self-designed oxide chamber at 700 °C for 1 hour in a vacuum of 10^{-8} mbar.

6.2 Selection and tests of the dome materials

The primary aim of the oxide chamber is to achieve insight into the structural changes during oxygen desorption, where not only the out-of-plane lattice parameter, but also in-situ measurements of the in-plane lattice parameter are required. In general, vacuum

chambers are made of stainless steel. However transmission of steel for x-rays is very low [137]. Thus suitable materials need to be selected carefully.

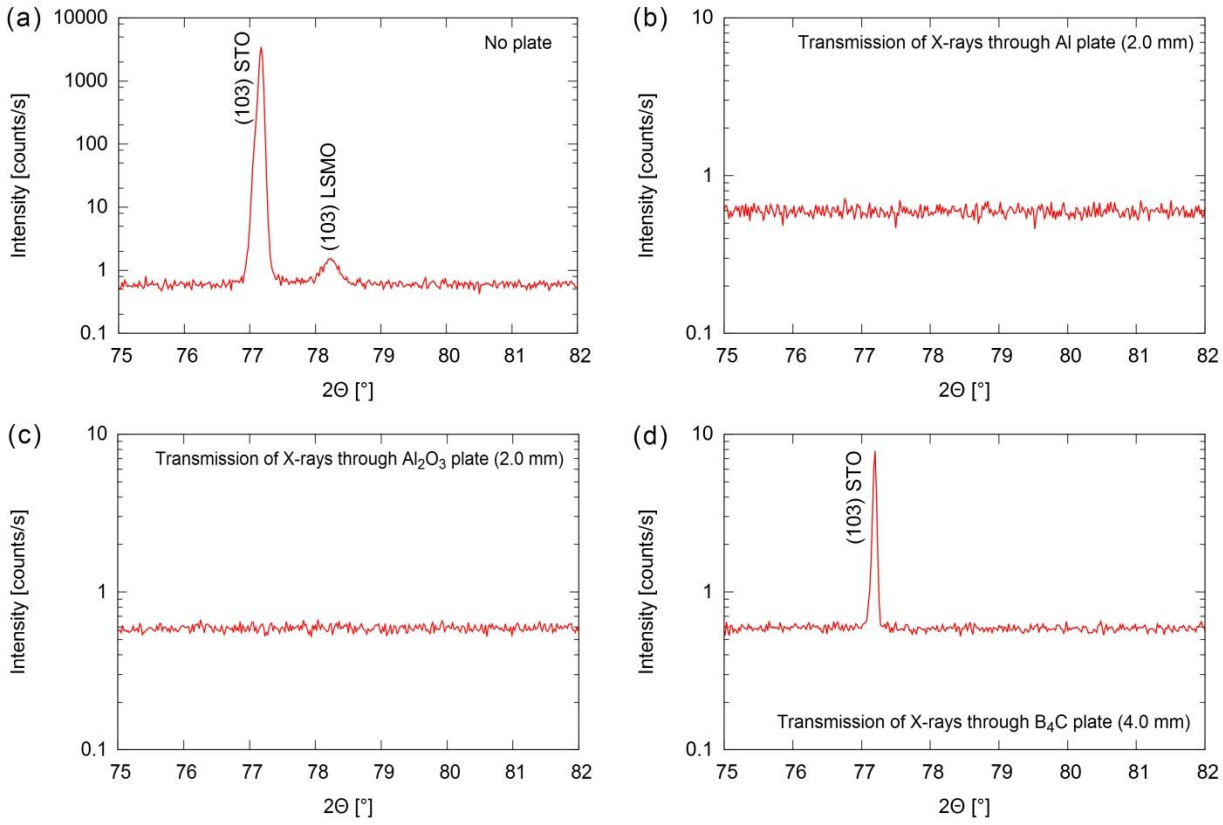

Figure 6.4: XRD scans around the (103) Bragg reflection for the as-prepared state measured with different types of materials as a plate placed before the detector to compare the transmission of x-rays from a Cu source. a) without any plate, b) with an Al plate, c) with an Al_2O_3 plate, d) with an B_4C plate.

In **Figure 6.4,** the transmissions of X-rays through different materials are compared. The data were collected on the Brucker “D8 Advanced” X-ray reflectometer using the copper X-ray source. In the experiments, the XRD scans around the (103) Bragg peak of the as-prepared LSMO film was measured first. Afterwards a plate made of different

materials (e.g. Al, Al_2O_3, B_4C) was placed in the path of the x-ray beam. Then the intensity of the diffracted x-ray beam was recorded with triple the exposure time.

As shown in the figure, for Al and Al_2O_3, both Bragg peaks from the LSMO film and the STO substrate disappear after placing the plate with the thickness of 2 mm in the beam path. This suggests that the transmission of Cu X-rays through these two materials is very low, which is consistent with the calculation results for the X-ray transmission as shown in **Table 6.1**. The X-ray transmission is calculated using the following equation:

$$I = I_0 \cdot exp(-k \cdot d) \tag{6.1}$$

Here, k is the absorption coefficient and d is the thickness. I_0 is the intensity of the incoming beam and I is the intensity of the outgoing beam.

Table 6.1: X-ray transmission for different materials with thickness of 1 mm

X-ray source	Al	Al_2O_3	B_4C
Cu radiation (1.54 Å)	0.0024 %	0.61 %	80.68 %
Ag radiation (0.56 Å)	60.94 %	79.29 %	99.21 %

For B_4C, which also consists of only light elements, the calculation shows very promising results. In the real test, we find that the (103) Bragg peak of the STO substrate is visible after placing a 4 mm B_4C plate in the beam, while the film Bragg peak is too weak to detect. As the transmission decreases exponentially with the increase of thickness, a thinner B_4C plate would exhibit less absorption for X-rays, making it a promising candidate. For measurements on the 4-circle diffractometer, a dome-shaped X-ray window is more ideal since one needs to cover a wider range of angles if the rotation of the sample is considered. However B_4C, is one of the hardest known ceramics with a Vickers Hardness of >30 GPa, which is very difficult to machine for shaping a dome.

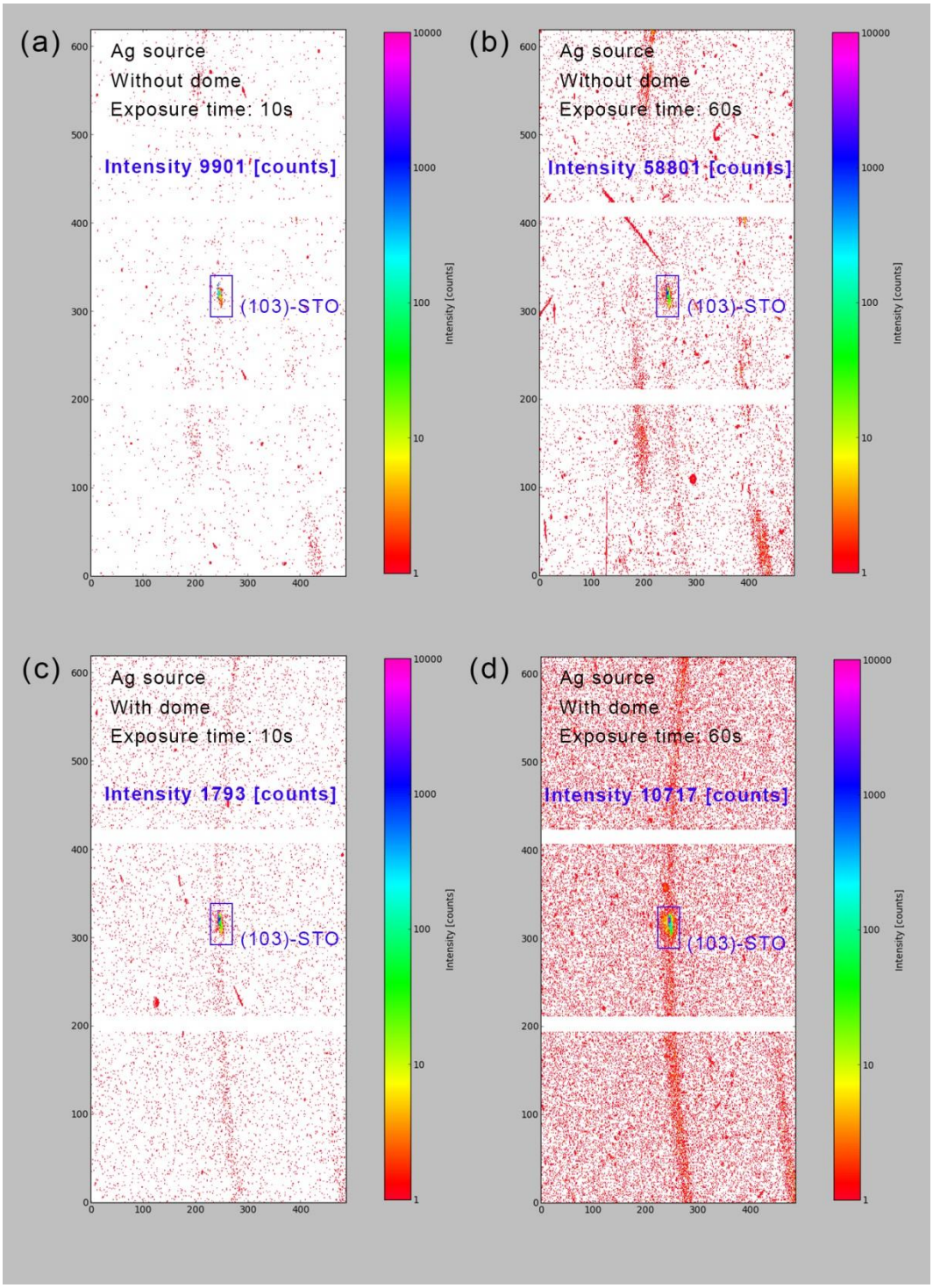

Figure 6.5: Intensity of the (103) Bragg peak measured by the two-dimensional (2D) area detector on the 4-circle diffractometer with the silver X-ray source: a) without Al dome, exposure time: 10s, b) without Al dome, exposure time: 60s, c) with Al dome, exposure time: 10s, d) with Al dome, exposure time: 60s.

Another option is to fabricate a beryllium dome, considering the low atomic order number, high mechanical strength, and gas tight nature. However, the toxicity of beryllium poses a health risk that requires safety procedures during the manufacturing and manipulation of the beryllium. In addition, Beryllium reacts readily with numerous chemicals including water vapor and oxygen, increasing the risk during annealing at high temperatures. Therefore, a protective coating for passivation is needed if using beryllium as dome material, which would further reduce the transmission.

Since no alternative material is available for the copper x-ray source without severe drawbacks, one plausible solution is to use another source (e.g. Ag source) to generate the x-ray beam. The wavelength for a silver X-ray source is 0.56 Å. The thickness of the dome wall is 1 mm so that the x-ray beam has to penetrate a total thickness of 2 mm. The calculation shows that the transmission rate of X-ray beam through aluminum is 30.31 % at the thickness of 2 mm. This is very promising. **Figure 6.5** shows the comparison of diffracted intensities for the aluminum dome using an Ag source. With mounting the aluminum dome, the (103) peak is visible and still has 18.23 % of the intensity compare with the measurements without the dome mounted. This suggests that with prolonging five times the measuring time, aluminum is suitable as a dome material provided one uses an Ag X-ray source.

However, the Ag source is not equipped with a monochromator, resulting in a XRD spectrum containing Bremsstrahlung and the Ag $K_{\alpha 2}$ line. Therefore further test measurements on the LSMO film at different states were performed using the Ag source, as shown in **Figure 6.6**. Here the pure STO substrate was measured at first for comparison. A splitting of the (002) peak is observed as expected due to the presence of Ag $K_{\alpha 2}$. By narrowing the counting region on the 2D detector, the separation of Ag $K_{\alpha 1}$ and Ag $K_{\alpha 2}$ becomes clearer in the XRD scans of the LSMO samples. For the as-prepared state, the film peak can be well observed at higher diffraction angles. After annealing for 3 hours, the film peak shift towards lower angles, which is consistent with the observation in the measurements using the XRR chamber. However, with increasing the annealing time, the film peak will become more difficult to probe as it buries in the large background due to Bremsstrahlung. This is because the intensity of

the film Bragg peak is 2 to 3 orders of magnitude lower than the substrate peak, which is unfortunately at the same order of magnitude for the Bremsstrahlung background. Therefore monochromatic X-radiation is critical for quantitative measurements of the lattice parameter change during oxygen desorption.

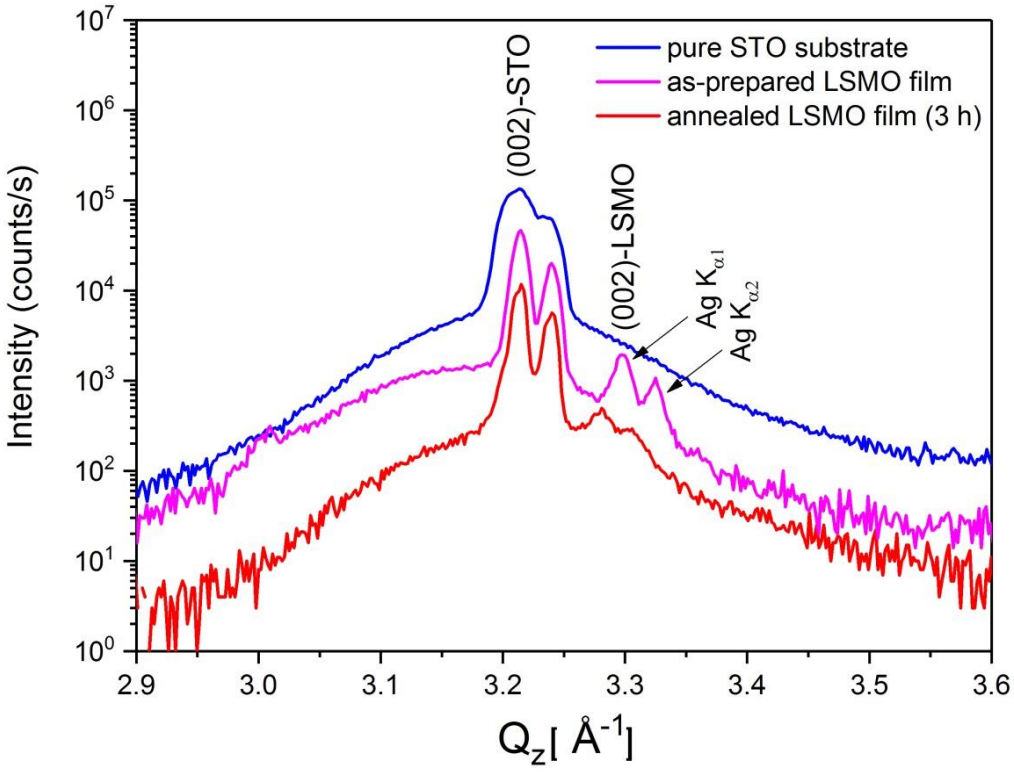

Figure 6.6: XRD scans around (002) Bragg reflection measured on the 4-circle diffractometer with the silver X-ray source.

6.3 Outlook for the quantitative determination of oxygen desorption

The second goal of the oxide chamber is to quantitatively study the release of oxygen atoms during the post-annealing process. According to the discussion in the last chapter,

LSMO films will lose oxygen atoms at a particular temperature range in vacuum. In bulk system, by measuring the change in mass of the sample, the total amount of lost oxygen atoms can be calculated and used to determine the relative change in oxygen stoichiometry. However, this method is not feasible in thin film systems due to the small amount of mass. In order to quantitatively determine the change of oxygen content in the thin film systems, we came up with another solution, i.e. a precise measurement of the pressure change during annealing. The outline of this idea is described below.

As discussed in the previous chapter, oxygen desorption induces a phase transition from the PV to BM structure while annealing above 300 °C. Therefore the oxygen stoichiometry changes from $La_{0.7}Sr_{0.3}MnO_3$ to $La_{0.7}Sr_{0.3}MnO_{2.5}$ during the entire transformation, which means that 16.7 % of oxygen will be released from the LSMO film into the vacuum chamber. Since oxygen desorption occurs in vacuum, it is a good approximation of the behavior for the oxygen gas using the ideal gas law:

$$PV = nRT \tag{6.2}$$

$$n = \frac{N_{O_2}}{N_A} \tag{6.3}$$

Here, P is the pressure of the gas and V is volume of the gas. n is the number of moles. R is the universal gas constant, equal to the product of the Boltzmann constant and the Avogadro constant. T is the absolute temperature of the gas. N_{O_2} is the number of oxygen gas molecules. N_A is the Avogadro constant.

On the other hand, the total amount of oxygen atoms within the LSMO film can be determined considering its structure. Employing in-situ XRD measurements, the lattice parameters of the LSMO film can be measured. Once the thickness of the film is measured by XRR, the amount of unit cells in a single crystalline LSMO film can be determined. Thus the number of oxygen molecules released in the vacuum chamber is correlated with the percentage of oxygen loss (x)in the film, according to equation (6.4).

$$No_2 = x \times \frac{1}{2} \times 3 \times \frac{A \times B \times C}{a \times b \times c} \tag{6.4}$$

Here, A is the length, B the width, and C is the thickness of the LSMO thin film. a, b, c are the lattice parameters of LSMO. Factor 3 is derived from the oxygen stoichiometry of LSMO. Factor ½ is introduced because one oxygen molecule contains two oxygen atoms.

Thus the percentage of oxygen loss (x)in the film can be written as

$$x = \frac{P \cdot V \cdot N_A}{R \cdot T} \times \frac{2}{3} \times \frac{a \cdot b \cdot c}{A \cdot B \cdot C} \tag{6.5}$$

The corresponding error can be determined by:

$$\Delta x = \frac{2 \cdot N_A}{3 \cdot R}\left[\Delta p \cdot \left(\frac{V \cdot a \cdot b \cdot c}{T \cdot A \cdot B \cdot C}\right) + \Delta V \cdot \left(\frac{p \cdot a \cdot b \cdot c}{T \cdot A \cdot B \cdot C}\right) + \Delta T \cdot \left(-\frac{P \cdot V \cdot a \cdot b \cdot c}{T^2 \cdot A \cdot B \cdot C}\right) + \Delta a \cdot \left(\frac{p \cdot V \cdot b \cdot c}{T \cdot A \cdot B \cdot C}\right) + \Delta b \cdot \left(\frac{p \cdot V \cdot a \cdot c}{T \cdot A \cdot B \cdot C}\right) + \Delta c \cdot \left(\frac{p \cdot V \cdot a \cdot b}{T \cdot A \cdot B \cdot C}\right) + \Delta A \cdot \left(-\frac{P \cdot V \cdot a \cdot b \cdot c}{T \cdot A^2 \cdot B \cdot C}\right) + \Delta B \cdot \left(-\frac{P \cdot V \cdot a \cdot b \cdot c}{T \cdot A \cdot B^2 \cdot C}\right) + \Delta C \cdot \left(-\frac{P \cdot V \cdot a \cdot b \cdot c}{T \cdot A \cdot B \cdot C^2}\right)\right] \tag{6.6}$$

By calculation, if we assume the volume of the chamber is 1 liter., the release of oxygen from a 10 mm × 10 mm LSMO film (thickness: 100 nm) will result in an increase of pressure to 10^{-5}~10^{-6} mbar in an isolated vacuum chamber. If the base pressure of the chamber reaches 10^{-8} mbar, the pressure rise after annealing will be detectable by the high resolution pressure gauge. The pressure change can be measured with a relative error less than 1 %. As discussed above, the thickness of LSMO film can be precisely determined by XRR measurements with small errors. The variation of oxygen stoichiometry during annealing can thus be determined with an estimated error of 2~3 %.

In the next step, a precise determination of the inner volume of the oxide chamber will be needed. Two promising solution would be: i) Gravimetric method by weighing the vessel filled with a liquid of known density, ii) Gas expansion methods which is based on a measurement of rate of pressure rise in a vacuum chamber at a constant flow of an inert gas. When the accurate volume of the chamber is known, such an oxide chamber would provide an alternative approach to quantitatively investigate the oxygen content change during the topotactic transitions in complex oxides.

6.4 Summary

This chapter comprises the design, construction and test of the self-built oxygen absorption/ desorption chamber. The chamber will be mounted on the 4-circle diffractometer to perform in-situ XRD measurements on the oxide systems (e.g. LSMO thin films). The detailed knowledge emerging from such a study will achieve insight into the in-plane lattice parameter changes during post-annealing processes.

The base pressure of the chamber can reach 10^{-8} mbar without bakeout. With mounting an aluminum dome, such a setup allows us to measure the crystallographic properties at varying temperatures up to 1000 °C.

Another part of this chapter illustrates an alternative approach to determine the oxygen content in oxide thin film systems. By in-situ analysis of lattice parameter changes and simultaneous pressure measurements, one can perform a quantitative determination of the oxygen loss during post-annealing processes in future studies. While the chamber could be designed and built during the thesis, the application was hampered by the lack of a suitable monochromator for Ag radiation.

Chapter 7

Summary and Outlook

The main task of this thesis is to investigate the role of the oxygen content in the crystallographic lattice onto the physical properties in complex oxide thin films.

In this work, we succeed in the epitaxial growth of $La_{0.7}Sr_{0.3}MnO_3$ (LSMO) thin films by High Oxygen Pressure Sputter Deposition (HOPSD). The stoichiometry of the LSMO films is confirmed by Rutherford Backscattering Spectrometry (RBS) measurements. Structural analysis by X-ray scattering methods indicates a good crystalline structure and a smooth surface. During preparation, the out-of-plane lattice parameter of the LSMO films can be varied by tuning the oxygen partial pressure in the HOPSD chamber. This effect is attributed to oxygen defects formed during preparation. The magnetic and electric transport properties are characterized for various as-prepared LSMO samples. Both the Curie temperature and the shape of hysteresis loops are found to be highly dependent on the oxygen content variation. On the other hand, all the as-prepared samples exhibit a metal-insulator transition and show colossal magnetoresistance (CMR) effect, where the T_{MI} corresponds well to its Curie temperature. A stronger CMR effect is evidenced in the films grown at a lower oxygen partial pressure.

Furthermore, a remarkable observation is the reversible control of the physical properties via an oxygen vacancy-driven topotactic transition during a post-annealing process. By heating the sample in vacuum, a structural transformation from PV to BM is induced and directly monitored by in-situ X-ray diffraction. Not only an intermediate phase is observed for the first time, but also the accompanying lattice expansion is characterized quantitatively in real-time. Huge changes of the physical properties from ferromagnetic metal to an antiferromagnetic insulator are found with only altering the oxygen content. The reverse switching from BM to PV is observed at significantly lower conditions (temperatures below 100 °C and conversion time less than 30 min)

compared to other studies, where a restoration of ferromagnetism and metallic properties is also achieved.

Even more fascinating is the direct and precise determination of the oxygen content in a thin film by neutron scattering. Since the oxygen content is a parameter hard to determine and to control in oxide thin films, our study provides a promising approach using polarized neutron reflectometry to achieve a layer-resolved oxygen stoichiometry. Thus a full map of the structure-property relationship is established in dependence of the oxygen content in LSMO thin films.

In addition, an in-situ x-ray diffraction chamber is constructed for the 4-circle diffractometer. This will allow us to measure, in-situ, the crystallographic properties by X-ray scattering. Furthermore, by the precise measurement of the pressure change during an annealing process, one will be able to quantitatively determine the oxygen loss within LSMO films and in general within any oxide samples. Such a method will provide an alternative approach to determine the oxygen content variation.

Part of the work in this thesis is published in the journal Advanced Materials. A second manuscript is in the stage of concrete preparation.

Acknowledgments

This work would not have been possible without the support of numerous people. Here I would to express my sincere gratitude to the following people:

Prof. Dr. Thomas Brückel for providing me the opportunity to work at JCNS-2, and for his great support and guidance in this fascinating project. I would like to especially thank him for providing me the opportunities to travel to various places to participate at conferences and beamtimes.

Prof. Dr. Matthias Wuttig for agreeing to take the second revision of this work.

Especially, I would like to thank my supervisor **PD Dr. Oleg Petracic** for all the support and the discussions we had during the last four years. I am very grateful for his encouragement, kindness and constructive suggestions throughout my thesis work. I am also extremely thankful for his advices about the scientific career.

Dr. Alexander Weber for fruitful discussions about the oxide chamber.

Dr. Paul Zakalek, **Dr. Markus Waschk** and **Dr. Ulrich Rücker** for their help during the sample preparation, reflectivity measurements and data treatments.

Dr. Yinguo Xiao, Dr. Xiao Sun and **Dr. Liming Wang** for their help and support at MPMS, PPMS and Dynacool.

Dr. Karen Frise, **Dr. Erxi Feng**, **Paul Hering** and **Markus Herrmann** for the fruitful discussions about the XRD results.

Dr. Stefan Mattauch and **Dr. Alexandros Koutsioumpas** for the scientific support during and after the neutron reflectivity measurements performed at the MLZ.

Dr. Yixi Su and **Dr. Thomas Müller** for their support during the measurements at DNS.

Dr. Jürgen Schubert for his help in the sample preparation and RBS measurements.

Dr. XianKui Wei for the help with STEM measurements at ER-C.

Dr. Heinrich Hartmann for his support and data analyses during XPS measurements.

Dr. Jörg Perßon for his help with the target preparation.

Frank Gossen, Micha Hölzle and **Berthold Schmitz** for technical assistance in all ways.

Annika Stellhorn, **Patrick Schöffmann**, the MBE Team, for supporting my sample treatments and fruitful discussions.

I would like to thank **Dr. Xiao Sun**, **Dr. Liming Wang**, **Dr. Erxi Feng**, **Dr. Cheng Li**, **Wenhai Ji** and **Can Cheng** for all the pleased moments we had together at work and in leisure time.

I want to thank all the members at JCNS-2 not only for the scientific discussions, but also for creating a lovely atmosphere.

Financial support from China Scholarship Council (CSC) is gratefully acknowledged.

Last but not least I would like to especially thank my wife and parents for their support and encouragement.

Bibliography

[1] Adler, S. B. Factors Governing Oxygen Reduction in Solid Oxide Fuel Cell Cathodes. *Chem. Rev.* 104, 4791–4844 (2004).

[2] Petrie, J. R., Jeen, H., Barron, S. C., Meyer, T. L. & Lee, H. N. Enhancing Perovskite Electrocatalysis through Strain Tuning of the Oxygen Deficiency. *J. Am. Chem. Soc.* 138, 7252–7255 (2016).

[3] la O', G. J. *et al.* Catalytic Activity Enhancement for Oxygen Reduction on Epitaxial Perovskite Thin Films for Solid-Oxide Fuel Cells. *Angew. Chemie Int. Ed.* 49, 5344–5347 (2010).

[4] Crumlin, E. J. *et al.* Oxygen Reduction Kinetics Enhancement on a Heterostructured Oxide Surface for Solid Oxide Fuel Cells. *J. Phys. Chem. Lett.* 1, 3149–3155 (2010).

[5] Hwang, J. *et al.* Perovskites in catalysis and electrocatalysis. *Science.* 358, 751–756 (2017).

[6] Sawa, A. Resistive switching in transition metal oxides. *Mater. Today* 11, 28–36 (2008).

[7] Waser, R., Dittmann, R., Staikov, C. & Szot, K. Redox-based resistive switching memories nanoionic mechanisms, prospects, and challenges. *Adv. Mater.* 21, 2632–2663 (2009).

[8] Acharya, S. K. *et al.* Epitaxial Brownmillerite Oxide Thin Films for Reliable Switching Memory. *ACS Appl. Mater. Interfaces* 8, 7902–7911 (2016).

[9] Yao, L., Inkinen, S. & van Dijken, S. Direct observation of oxygen vacancy-driven structural and resistive phase transitions in La2/3Sr1/3MnO3. *Nat. Commun.* 8, 14544 (2017).

[10] Kalinin, S. V & Spaldin, N. A. Functional Ion Defects in Transition Metal Oxides.

Science. 341, 858–859 (2013).

[11] Huijben, M. *et al.* Structure-Property Relation of SrTiO3 /LaAlO3 Interfaces. *Adv. Mater.* 21, 1665–1677 (2009).

[12] Jeen, H. *et al.* Topotactic Phase Transformation of the Brownmillerite SrCoO2.5 to the Perovskite SrCoO3-δ. *Adv. Mater.* 25, 3651–3656 (2013).

[13] Jang, J. H. *et al.* In Situ Observation of Oxygen Vacancy Dynamics and Ordering in the Epitaxial LaCoO 3 System. *ACS Nano* 11, 6942–6949 (2017).

[14] Khare, A. *et al.* Topotactic Metal-Insulator Transition in Epitaxial SrFeOx Thin Films. *Adv. Mater.* 29, 1606566 (2017).

[15] Kendrick, E., Kendrick, J., Knight, K. S., Islam, M. S. & Slater, P. R. Cooperative mechanisms of fast-ion conduction in gallium-based oxides with tetrahedral moieties. *Nat. Mater.* 6, 871–875 (2007).

[16] Inoue, S. *et al.* Anisotropic oxygen diffusion at low temperature in perovskite-structure iron oxides. *Nat. Chem.* 2, 213–217 (2010).

[17] Kim, Y.-M. *et al.* Probing oxygen vacancy concentration and homogeneity in solid-oxide fuel-cell cathode materials on the subunit-cell level. *Nat. Mater.* 11, 888–894 (2012).

[18] Hemberger, J. *et al.* Structural, magnetic, and electrical properties of single-crystalline La1-xSrxMnO3 (0.4<x<0.85). *Phys. Rev. B* 66, 094410 (2002).

[19] Horiba, K. *et al.* Pressure-induced change in the electronic structure of epitaxially strained La1−xSrxMnO3 thin films. *Phys. Rev. B* 80, 132406 (2009).

[20] Peña, M. A. & Fierro, J. L. G. Chemical Structures and Performance of Perovskite Oxides. *Chem. Rev.* 101, 1981–2018 (2001).

[21] Rose, G. Beschreibung einiger neuen Mineralien des Urals. *Ann. der Phys. und Chemie* 126, 652–656 (1840).

[22] Momma, K. & Izumi, F. VESTA 3 for three-dimensional visualization of crystal, volumetric and morphology data. *J. Appl. Crystallogr.* 44, 1272–1276 (2011).

[23] Momma, K. & Izumi, F. VESTA : a three-dimensional visualization system for electronic and structural analysis. *J. Appl. Crystallogr.* 41, 653–658 (2008).

[24] Fiebig, M. Revival of the magnetoelectric effect. *J. Phys. D. Appl. Phys.* 38, R123–R152 (2005).

[25] Matsukura, F., Tokura, Y. & Ohno, H. Control of magnetism by electric fields. *Nat. Nanotechnol.* 10, 209–220 (2015).

[26] Gajek, M. *et al.* Tunnel junctions with multiferroic barriers. *Nat. Mater.* 6, 296–302 (2007).

[27] Haghiri-Gosnet, A.-M. & Renard, J.-P. CMR manganites: physics, thin films and devices. *J. Phys. D. Appl. Phys.* 36, R127–R150 (2003).

[28] Hwang, H. Y. *et al.* Emergent phenomena at oxide interfaces. *Nat. Mater.* 11, 103–113 (2012).

[29] Brinkman, A. *et al.* Magnetic effects at the interface between non-magnetic oxides. *Nat. Mater.* 6, 493–496 (2007).

[30] Howard, C. J. & Stokes, H. T. Group-Theoretical Analysis of Octahedral Tilting in Perovskites. Erratum. *Acta Crystallogr. Sect. B Struct. Sci.* 58, 565–565 (2002).

[31] Woodward, P. M. *et al.* Influence of Cation Size on the Structural Features of Ln1/2A1/2MnO3 Perovskites at Room Temperature. *Chem. Mater.* 10, 3652–3665 (1998).

[32] Jahn, H. A. & Teller, E. Stability of polyatomic molecules in degenerate electronic states - I—Orbital degeneracy. *Proc. R. Soc. London. Ser. A - Math. Phys. Sci.* 161, 220–235 (1937).

[33] Anderson, P. W. Antiferromagnetism. Theory of Superexchange Interaction. *Phys. Rev.* 79, 350–356 (1950).

[34] Goodneough, J. B. Theory of the Role of Covalence in the Perovskite-Type Manganites [La,M(II)]MnO3. *Phys. Rev.* 100, 564–573 (1955).

[35] Goodenough, J. B. An interpretation of the magnetic properties of the perovskite-type mixed crystals La1−xSrxCoO3−λ. *J. Phys. Chem. Solids* 6, 287–297 (1958).

[36] Kanamori, J. Superexchange interaction and symmetry properties of electron orbitals. *J. Phys. Chem. Solids* 10, 87–98 (1959).

[37] Zener, C. Interaction between the d-Shells in the Transition Metals. II. Ferromagnetic Compounds of Manganese with Perovskite Structure. *Phys. Rev.* 82, 403–405 (1951).

[38] Coey, J. M. D. *Magnetism and Magnetic Materials*. (Cambridge University Press, 2010). doi:10.1017/CBO9780511845000

[39] Petracic, O. Superparamagnetic nanoparticle ensembles. *Superlattices Microstruct.* 47, 569–578 (2010).

[40] Bedanta, S. & Kleemann, W. Supermagnetism. *J. Phys. D. Appl. Phys.* 42, 013001 (2009).

[41] Néel, L. Anisotropie magnétique superficielle et surstructures d'orientation. *J. Phys. le Radium* 15, 225–239 (1954).

[42] Garanin, D. A. & Kachkachi, H. Surface Contribution to the Anisotropy of Magnetic Nanoparticles. *Phys. Rev. Lett.* 90, 065504 (2003).

[43] Respaud, M. *et al.* Surface effects on the magnetic properties of ultrafine cobalt particles. *Phys. Rev. B* 57, 2925–2935 (1998).

[44] Cullity, B. D. & Graham, C. D. *Introduction to Magnetic Materials*. (John Wiley & Sons, Inc., 2008). doi:10.1002/9780470386323

[45] Akimoto, T. *et al.* Antiferromagnetic metallic state in doped manganites. *Phys. Rev. B* 57, R5594–R5597 (1998).

[46] Moritomo, Y., Akimoto, T., Nakamura, A., Ohoyama, K. & Ohashi, M. Antiferromagnetic metallic state in the heavily doped region of perovskite manganites. *Phys. Rev. B* 58, 5544–5549 (1998).

[47] Wollan, E. O. & Koehler, W. C. Neutron Diffraction Study of the Magnetic Properties of the Series of Perovskite-Type Compounds [(1-x)la,xCa]MnO3. *Phys. Rev.* 100, 545–563 (1955).

[48] Li, H. F. *et al.* Correlation between structural and magnetic properties of La 7/8 Sr 1/8 Mn 1−γ O 3+δ with controlled nonstoichiometry. *J. Phys. Condens. Matter* 19, 016003 (2007).

[49] Li, H. Synthesis of CMR manganites and ordering phenomena in complex transition metal oxides. PhD thesis. (RWTH Aachen, 2008).

[50] Tilley, R. J. D. *Perovskites : structure-property relationships*. (John Wiley & Sons, 2016).

[51] Dréau, L. Le. Phase transitions and oxygen ordering in La2CoO4+ δ and (T, T')-La2CuO4: single crystal growth and structural studies using synchrotron and neutron diffraction methods. PhD thesis. (Université Rennes, 2011).

[52] Young, J. & Rondinelli, J. M. Crystal Structure and Electronic Properties of Bulk and Thin Film Brownmillerite Oxides. 174111, 1–10 (2015).

[53] Milton, O. *Materials Science of Thin Films*. (Elsevier, 1992).

[54] Seshan, K. & Dominic, S. *Handbook of thin film deposition*. (William Andrew, 2018).

[55] Knoll, W. & Advincula, R. C. *Functional Polymer Films, 2 Volume Set.* (John Wiley & Sons, 2013).

[56] Venables, J. A. Atomic processes in crystal growth. *Surf. Sci.* 299–300, 798–817 (1994).

[57] Venables, J. A., Spiller, G. D. T. & Hanbucken, M. Nucleation and growth of thin

films. *Reports Prog. Phys.* 47, 399–459 (1984).

[58] Brückel, T., Richter, D., Roth, G., Wischnewski, A. & Zorn, R. *Neutron Scattering*. (Forschungszentrum Jülich GmbH, 2015).

[59] Sivia, D. S. *Elementary Scattering Theory*. (Oxford University Press, 2011).

[60] Birkholz, M. *Thin film analysis by X-ray scattering*. (John Wiley & Sons, 2006).

[61] Zabel, H. X-ray and neutron reflectivity analysis of thin films and superlattices. *Appl. Phys. A Solids Surfaces* 58, 159–168 (1994).

[62] Poppe, U. *et al.* Low-resistivity epitaxial YBa2Cu3O7 thin films with improved microstructure and reduced microwave losses. *J. Appl. Phys.* 71, 5572–5578 (1992).

[63] Waschk, M. Interface phenomena in La1/3Sr2/3FeO3 /La2/3Sr1/3MnO3 heterostructures and a quest for p-electron magnetism. PhD Thesis. (RWTH Aachen, 2017).

[64] Schmitz, M. Strain and electric field mediated manipulation of magnetism in La(1-x)SrxMnO3 /BaTiO3 heterostructures. PhD Thesis. (RWTH Aachen, 2015).

[65] Cushman, C. V. *et al.* Trends in Advanced XPS Instrumentation. 1. Overview of the Technique, Automation, High Sensitivity, Imaging, Snapshot Spectroscopy, Gas Cluster Ion Beams, and Multiple Analytical Techniques on the Instrument. *Vac. Technol. Coat.* 1–9 (2016).

[66] Doolittle, L. R. Algorithms for the rapid simulation of Rutherford backscattering spectra. *Nucl. Instruments Methods Phys. Res. Sect. B Beam Interact. with Mater. Atoms* 9, 344–351 (1985).

[67] Doolittle, L. R. A semiautomatic algorithm for rutherford backscattering analysis. *Nucl. Instruments Methods Phys. Res. Sect. B Beam Interact. with Mater. Atoms* 15, 227–231 (1986).

[68] Stroppa, D. G., Zagonel, L. F., Montoro, L. A., Leite, E. R. & Ramirez, A. J. High-

Resolution Scanning Transmission Electron Microscopy (HRSTEM) Techniques: High-Resolution Imaging and Spectroscopy Side by Side. *ChemPhysChem* 13, 437–443 (2012).

[69] Zakalek, P. Magnetic Interface Effects in Thin Film Heterostructures. PhD Thesis. (RWTH Aachen, 2015).

[70] Mattauch, S., Koutsioubas, A. & Pütter, S. MARIA: Magnetic reflectometer with high incident angle. *J. large-scale Res. Facil. JLSRF* 1, A8 (2015).

[71] Mattauch, S. *et al.* The high-intensity reflectometer of the Jülich Centre for Neutron Science: MARIA. *J. Appl. Crystallogr.* 51, 646–654 (2018).

[72] Björck, M. & Andersson, G. GenX : an extensible X-ray reflectivity refinement program utilizing differential evolution. *J. Appl. Crystallogr.* 40, 1174–1178 (2007).

[73] Dong, K. *et al.* Large lattice mismatch effects on the epitaxial growth and magnetic properties of FePt films. *J. Magn. Magn. Mater.* 446, 125–134 (2017).

[74] Adamo, C. *et al.* Enhanced electrical and magnetic properties in La0.7Sr0.3MnO3 thin films deposited on CaTiO3-buffered silicon substrates. *APL Mater.* 3, 062504 (2015).

[75] Kawasaki, M. *et al.* Atomic Control of the SrTiO3 Crystal Surface. *Science.* 266, 1540–1542 (1994).

[76] Katsiev, K., Yildiz, B., Balasubramaniam, K. & Salvador, P. A. Electron tunneling characteristics on La0.7Sr0.3MnO3 thin-film surfaces at high temperature. *Appl. Phys. Lett.* 95, 092106 (2009).

[77] Fister, T. T. *et al.* In situ characterization of strontium surface segregation in epitaxial La0.7Sr0.3MnO3 thin films as a function of oxygen partial pressure. *Appl. Phys. Lett.* 93, 151904 (2008).

[78] Xie, Y. *et al.* Control of Functional Responses Via Reversible Oxygen Loss in La1- xSrxFeO3-δ Films. *Adv. Mater.* 26, 1434–1438 (2014).

[79] Orgiani, P. *et al.* Evidence of direct correlation between out-of-plane lattice parameter and metal-insulator transition temperature in oxygen-depleted manganite thin films. *Appl. Phys. Lett.* 100, 042404 (2012).

[80] Petrisor, T. *et al.* Oxygen incorporation effects in annealed epitaxial La(1−x)SrxMnO3 thin films. *J. Appl. Phys.* 109, 123913 (2011).

[81] Yin, L., Wang, C., Shen, Q. & Zhang, L. Strain-induced Curie temperature variation in La 0.9 Sr 0.1 MnO 3 thin films. *RSC Adv.* 6, 96093–96102 (2016).

[82] Tokura, Y. *et al.* Giant Magnetotransport Phenomena in Filling-Controlled Kondo Lattice System: La 1- x Sr x MnO 3. *J. Phys. Soc. Japan* 63, 3931–3935 (1994).

[83] Jeen, H. *et al.* Reversible redox reactions in an epitaxially stabilized SrCoOx oxygen sponge. *Nat. Mater.* 12, 1057–1063 (2013).

[84] Molinari, A., Hahn, H. & Kruk, R. Voltage-Controlled On/Off Switching of Ferromagnetism in Manganite Supercapacitors. *Adv. Mater.* 30, 1703908 (2018).

[85] Molinari, A. *et al.* Hybrid supercapacitors for reversible control of magnetism. *Nat. Commun.* 8, 15339 (2017).

[86] Seo, S. H., Kang, H. C., Jang, H. W. & Noh, D. Y. Effects of oxygen incorporation in tensile La0.84Sr0.16MnO3-δ thin films during ex situ annealing. *Phys. Rev. B* 71, 012412 (2005).

[87] Hu, S., Wang, Y., Cazorla, C. & Seidel, J. Strain-Enhanced Oxygen Dynamics and Redox Reversibility in Topotactic SrCoO3-δ ($0 < \delta \leq 0.5$). *Chem. Mater.* 29, 708–717 (2017).

[88] Ferguson, J. D. *et al.* Epitaxial Oxygen Getter for a Brownmillerite Phase Transformation in Manganite Films. *Adv. Mater.* 23, 1226–1230 (2011).

[89] Casey, P. S., Barker, D. & Hayward, M. A. Charge and structural ordering in the brownmillerite phases: La1−xSrxMnO2.5 ($0.2<x<0.4$). *J. Solid State Chem.* 179, 1375–1382 (2006).

[90] Parsons, T. G., D'Hondt, H., Hadermann, J. & Hayward, M. A. Synthesis and Structural Characterization of La1−xAxMnO2.5 (A = Ba, Sr, Ca) Phases: Mapping the Variants of the Brownmillerite Structure. *Chem. Mater.* 21, 5527–5538 (2009).

[91] Dixon, E., Hadermann, J. & Hayward, M. A. Structures and Magnetism of La1–xSrxMnO3–(0.5+ x)/2 (0.67 ≤ x ≤ 1) Phases. *Chem. Mater.* 24, 1486–1495 (2012).

[92] Cazorla, C. Lattice Effects on the Formation of Oxygen Vacancies in Perovskite Thin Films. *Phys. Rev. Appl.* 7, 044025 (2017).

[93] Suescun, L. *et al.* Oxygen Ordered Phases in LaxSr1−xMnOy (0 ≤ x ≤ 0.2, 2.5 ≤ y ≤ 3): An In situ Neutron Powder Diffraction Study. *Chem. Mater.* 20, 1636–1645 (2008).

[94] Suescun, L., Chmaissem, O., Mais, J., Dabrowski, B. & Jorgensen, J. D. Crystal structures, charge and oxygen-vacancy ordering in oxygen deficient perovskites SrMnOx (x<2.7). *J. Solid State Chem.* 180, 1698–1707 (2007).

[95] Suescun, L. & Dabrowski, B. Sr4+nMn4MnnO10+3n : a new homologous series of oxygen-vacancy-ordered perovskites built from Mn3+O5 pyramids and Mn4+O6octahedra. *Acta Crystallogr. Sect. B Struct. Sci.* 64, 177–186 (2008).

[96] Roh, S. *et al.* Oxygen vacancy induced structural evolution of SrFeO3-x epitaxial thin film from brownmillerite to perovskite. *Phys. Rev. B* 97, 075104 (2018).

[97] Tsujimoto, Y. *et al.* Infinite-layer iron oxide with a square-planar coordination. 450, (2007).

[98] Yao, L. *et al.* Electron-Beam-Induced Perovskite-Brownmillerite-Perovskite Structural Phase Transitions in Epitaxial La2/3Sr1/3MnO3 Films. *Adv. Mater.* 26, 2789–2793 (2014).

[99] Li, Z. *et al.* Interface and Surface Cation Stoichiometry Modified by Oxygen Vacancies in Epitaxial Manganite Films. *Adv. Funct. Mater.* 22, 4312–4321 (2012).

[100] Bertacco, R., Contour, J. ., Barthélemy, A. & Olivier, J. Evidence for strontium

segregation in La0.7Sr0.3MnO3 thin films grown by pulsed laser deposition: consequences for tunnelling junctions. *Surf. Sci.* 511, 366–372 (2002).

[101] Fister, T. T. *et al.* In situ characterization of strontium surface segregation in epitaxial La0.7Sr0.3MnO3 thin films as a function of oxygen partial pressure. *Appl. Phys. Lett.* 93, 151904 (2008).

[102] Zheng, F. Phase Behavior of Lanthanum Strontium Manganites. *J. Electrochem. Soc.* 146, 2810 (1999).

[103] Jalili, H., Chen, Y. & Yildiz, B. Structural Chemical, and electronic state on La0.7Sr0.3MnO3 Dense Thin-film surfaces at High-Temperature-Surface Segregation. *J. Phys. Condens. Matter* 28, 060301 (2016).

[104] Dowben, P. A., Langell, M. A., Dulli, H., Liou, S.-H. & Choi, J. The Influence of Surface Terminal Layer and Surface Defects on the Electronic Structure of CMR Perovskites: La0.65A0.35MnO3 (A = Ca, Sr, Ba). *Phys. Status Solidi* 214, 45–57 (2002).

[105] Crumlin, E. J. *et al.* Surface strontium enrichment on highly active perovskites for oxygen electrocatalysis in solid oxide fuel cells. *Energy Environ. Sci.* 5, 6081–6088 (2012).

[106] Royer, S., Duprez, D. & Kaliaguine, S. Role of bulk and grain boundary oxygen mobility in the catalytic oxidation activity of LaCo1-xFexO3. *J. Catal.* 234, 364–375 (2005).

[107] Fierro, J. L. G. & Tejuca, L. G. Non-stoichiometric surface behaviour of LaMO3 oxides as evidenced by XPS. *Appl. Surf. Sci.* 27, 453–457 (1987).

[108] Li, F. *et al.* Modified surface electronic and magnetic properties of La 0.6Sr0.4MnO3 thin films for spintronics applications. *J. Phys. Chem. C* 115, 16947–16953 (2011).

[109] Vovk, G., Chen, X. & Mims, C. A. In situ XPS studies of perovskite oxide surfaces under electrochemical polarization. *J. Phys. Chem. B* 109, 2445–2454 (2005).

[110] Carson, G. A., Nassir, M. H. & Langell, M. A. Epitaxial growth of Co 3 O 4 on CoO(100) . *J. Vac. Sci. Technol. A Vacuum, Surfaces, Film.* 14, 1637–1642 (2002).

[111] Choi, J., Dowben, P. A. & Plummer, E. W. Surfaces of the perovskite manganites La 1-x Ca x MnO 3. *Phys. Rev. B* 59, 13453–13459 (1999).

[112] de Jong, M. P., Dediu, V. A., Taliani, C. & Salaneck, W. R. Electronic structure of La0.7Sr0.3MnO3 thin films for hybrid organic/inorganic spintronics applications. *J. Appl. Phys.* 94, 7292–7296 (2003).

[113] Deng, J. *et al.* Effect of hydrothermal treatment temperature on the catalytic performance of single-crystalline La0.5Sr0.5MnO3-δ microcubes for the combustion of toluene. *Catal. Today* 139, 82–87 (2008).

[114] Liang, J. J. & Weng, H. S. Catalytic Properties of La1−xSrxBO3 (B = Mn, Fe, Co, Ni) for Toluene Oxidation. *Ind. Eng. Chem. Res.* 32, 2563–2572 (1993).

[115] Gunasekaran, N., Rajadurai, S., Carberry, J. J., Bakshi, N. & Alcock, C. B. Surface characterization and catalytic properties of La1-xAxMO3 perovskite type oxides. Part I. Studies on La0.95Ba0.05MO3 (M = Mn, Fe or Co) oxides. *Solid State Ionics* 73, 289–295 (1994).

[116] Gunasekaran, N. Surface characterization and catalytic properties of perovskite type solid oxide solutions, La0.8Sr0.2BO3 (B = Cr, Mn, Fe, Co or Y). *Solid State Ionics* 83, 145–150 (1996).

[117] Hillebrand, R., Pippel, E., Hesse, D. & Vrejoiu, I. A study of intermixing in perovskite superlattices by simulation-supported cs-corrected HAADF-STEM. *Phys. status solidi* 208, 2144–2149 (2011).

[118] Garcia, V. *et al.* Ferroelectric Control of Spin Polarization. *Science.* 327, 1106–1110 (2010).

[119] Zhou, D., Sigle, W., Kelsch, M., Habermeier, H.-U. & van Aken, P. A. Electron-Beam-Induced Antiphase Boundary Reconstructions in a ZrO 2 -LSMO Pillar-

Matrix System. *ACS Appl. Mater. Interfaces* 8, 24177–24185 (2016).

[120] Li, X., Vrejoiu, I., Ziese, M. & van Aken, P. Direct observation of interfacial coupling of oxygen octahedra and its impact on ferromagnetic order in La0.7Sr0.3MnO3/SrTiO3 epitaxial heterostructures. in *European Microscopy Congress 2016: Proceedings* 106, 968–969 (Wiley-VCH Verlag GmbH & Co. KGaA, 2016).

[121] Battle, P. D. *et al.* Layered Ruddlesden-Popper Manganese Oxides: Synthesis and Cation Ordering. *Chem. Mater.* 9, 552–559 (1997).

[122] Dulli, H., Dowben, P. A., Liou, S.-H. & Plummer, E. W. Surface segregation and restructuring of colossal-magnetoresistant manganese perovskites La0.65Sr0.35MnO3. *Phys. Rev. B* 62, R14629–R14632 (2000).

[123] Grins, J. *et al.* A structural study of Ruddlesden–Popper phases Sr3−xYx (Fe 1.25 Ni 0.75) O7−δ with x ≤ 0.75 by neutron powder diffraction and EXAFS/XANES spectroscopy. *J. Mater. Chem. A* 6, 5313–5323 (2018).

[124] Sharma, I. B. & Singh, D. Solid state chemistry of Ruddlesden-Popper type complex oxides. *Bull. Mater. Sci.* 21, 363–374 (1998).

[125] Cooper, D. *et al.* Anomalous Resistance Hysteresis in Oxide ReRAM: Oxygen Evolution and Reincorporation Revealed by In Situ TEM. *Adv. Mater.* 29, 1–8 (2017).

[126] Gries, U. N. *et al.* A SIMS study of cation and anion diffusion in tantalum oxide. *Phys. Chem. Chem. Phys.* 20, 989–996 (2018).

[127] Heisig, T. *et al.* Oxygen Exchange Processes between Oxide Memristive Devices and Water Molecules. *Adv. Mater.* 30, 1–7 (2018).

[128] Rodenbücher, C. *et al.* Stability and Decomposition of Perovskite-Type Titanates upon High-Temperature Reduction. *Phys. Status Solidi - Rapid Res. Lett.* 11, 1–4 (2017).

[129] Szot, K. *et al.* Formation of micro-crystals on the (100) surface of SrTiO3 at elevated temperatures. *Surf. Sci.* 460, 112–128 (2000).

[130] Szot, K. *et al.* Nature of the surface layer in ABO3-type perovskites at elevated temperatures. *Appl. Phys. A Mater. Sci. Process.* 62, 335–343 (1996).

[131] Szot, K., Speier, W., Bihlmayer, G. & Waser, R. Switching the electrical resistance of individual dislocations in single-crystalline SrTiO3. *Nat. Mater.* 5, 312–320 (2006).

[132] Szot, K. & Speier, W. Surfaces of reduced and oxidized SrTiO3from atomic force microscopy. *Phys. Rev. B - Condens. Matter Mater. Phys.* 60, 5909–5926 (1999).

[133] Szot, K., Speier, W., Herion, J. & Freiburg, C. Restructuring of the surface region in SrTiO3. *Appl. Phys. A Mater. Sci. Process.* 64, 55–59 (1996).

[134] Ishimaru, H., Horikoshi, G. & Minoda, K. Bakeable Aluminium Vacuum Chamber and Bellows with an Aluminium Flange and Metal Seal for Ultrahigh Vacuum. *IEEE Trans. Nucl. Sci.* 26, 4000–4002 (1979).

[135] Suemitsu, M., Kaneko, T. & Miyamoto, N. Aluminum alloy ultrahigh vacuum chamber for molecular beam epitaxy. *J. Vac. Sci. Technol. A Vacuum, Surfaces, Film.* 5, 37–43 (1987).

[136] Ishimaru, H. All-aluminum-alloy ultrahigh vacuum system for a large-scale electron–positron collider. *J. Vac. Sci. Technol. A Vacuum, Surfaces, Film.* 2, 1170–1175 (1984).

[137] Huebner, S., Miyakawa, N., Kapser, S., Pahlke, A. & Kreupl, F. High Performance X-Ray Transmission Windows Based on Graphenic Carbon. *IEEE Trans. Nucl. Sci.* 62, 588–593 (2015).

[138] Valdes, L. B. Resistivity Measurements on Germanium for Transistors. *Proc. IRE* 42, 420–427 (1954).

Appendix A Acronyms

STO $SrTiO_3$.

LSMO $La_{0.7}Sr_{0.3}MnO_3$.

PV Perovskite.

BM Brownmillerite.

FM Ferromagnetic.

AFM Antiferromagnetic.

HOPSD High Oxygen Pressure Sputtering Deposition.

MFC Mass Flow Controller.

PVD Physical Vapor Deposition.

CVD Chemical Vapor Deposition.

XRD X-Ray Diffraction.

XRR X-Ray Reflectometry.

KEC Knife-Edge.

PNR Polarized Neutron Reflectometry.

SLD Scattering Length Density.

XPS X-ray Photoelectron Spectroscopy.

RBS Rutherford Backscattering Spectrometry.

STEM Scanning Transmission Electron Microscopy.

FIB Focused Ion Beam.

EDX Energy Dispersive X-ray Spectroscopy.

HAADF High-Angle Annular Dark-Field imaging.

BF Bright-Field imaging.

ABF Annular Bright-Field imaging.

ADF Annular Dark Field imaging.

EELS Electron Energy Loss.

MPMS Magnetic Property Measurement System.

SQUID Superconducting Quantum Interference Device.

PPMS Physical Property Measurement System.

VSM Vibrating Sample Magnetometer.

CMR Colossal magnetoresistance.

FC Field Cooling.

ZFC Zero Field Cooling.

HV High Vacuum.

UHV Ultra High Vacuum.

MLZ Heinz Maier-Leibnitz Zentrum.

ER-C Ernst Ruska-Centre.

Appendix B Physical constants

$c = 299792458\ \mathrm{m \cdot s^{-1}}$	speed of light in vacuum
$N_A = 6.022140857(74) \cdot 10^{23}\ \mathrm{mol^{-1}}$	Avogadro constant
$k_B = 1.38064852(79) \cdot 10^{23}\ \mathrm{J \cdot K^{-1}}$	Boltzmann constant
$R = N_A \cdot k_B = 8.3144598(48)\ \mathrm{J \cdot mol^{-1} \cdot K^{-1}}$	gas constant
$h = 6.626070040(81) \cdot 10^{-34}\ \mathrm{J \cdot s}$	Planck constant
$\hbar = h/2\pi$	reduced Planck constant
$m_n = m_p = 1.{:}672621898(21) \cdot 10^{-27}\ \mathrm{kg}$	proton and neutron mass
$m_e = 9.10938356(11) \cdot 10^{-31}\ \mathrm{kg}$	electron mass
$e = 1.6021766208(98) \cdot 10^{-19}\ \mathrm{C}$	elementary charge
$\mu_0 = 4\pi \cdot 10^{-7}\ N \cdot A^{-2}$	magnetic constant
$\epsilon_0 = \frac{1}{\mu_0 c^2}$	electric constant
$\mu_B = \frac{e\hbar}{2m_e}$	Bohr magneton
$\mu_n = \frac{e\hbar}{2m_n}$	nuclear magneton

Appendix C Supplementary information

C.1 Fit parameter

XRR fit parameters for sample SP01 are presented in the following tables.

Room temperature	FOM log: 2.555e-2	
Parameter	Value	asymmetric errors
top layer thickness [Å]	11.0020	(-1.051e+00, 1.174e+00)
top layer density [$Å^{-3}$]	0.01782	(-2.215e-04, 2.375e-04)
suface roughness [Å]	10.2605	(-1.655e-01, 1.902e-01)
LSMO layer thickness [Å]	598.1745	(-1.641e+00, 2.202e+00)
LSMO layer density [$Å^{-3}$]	0.01653	(-1.856e-04, 1.918e-04)
LSMO layer roughness [Å]	2.6380	(-2.424e-01, 1.340e+00)
substrate roughness [Å]	9.7803	(-9.745e-01, 1.072e+00)

XRR fit parameters for sample SP07 are presented in the following tables.

Room temperature	FOM log: 2.459e-2	
Parameter	Value	asymmetric errors
top layer thickness [Å]	14.1846	(-1.325e+00, 9.755e-01)
top layer density [$Å^{-3}$]	0.01702	(-2.167e-04, 2.270e-04)
top layer roughness [Å]	20.0000	(-3.024e-01, 3.659e-13)
LSMO layer thickness [Å]	397.5513	(-3.554e+00, 3.405e+00)
LSMO layer density [$Å^{-3}$]	0.01529	(-2.164e-04, 1.804e-04)
LSMO layer roughness [Å]	2.6568	(-1.110e+00, 1.202e+00)
substrate roughness [Å]	11.6936	(-1.469e+00, 1.474e+00)

PNR fit parameters for the intermediate phase are presented in the following tables.

10 K	FOM log: 6.7235e-2	
Parameter	Value	asymmetric errors
top layer thickness [Å]	78.7515	(-3.961e+00, 4.578e+00)
top layer density [$Å^{-3}$]	0.01660	(-1.776e-04, 2.445e-04)
magnetization for top layer [μ_B/uc]	0.9516	(-1.397e-01, 1.477e-01)
suface roughness [Å]	33.1385	(-8.782e-01, 2.015e+00)
LSMO layer thickness [Å]	254.3359	(-7.646e+00, 7.833e+00)
LSMO layer density [$Å^{-3}$]	0.01715	(-7.344e-04, 5.431e-05)
magnetization for LSMO layer [μ_B/uc]	1.6894	(-2.195e-01, 1.614e-01)
LSMO layer roughness [Å]	5.0657	(-1.448e-01, 7.708e-02)
bottom layer thickness [Å]	25.3036	(-2.115e+00, 5.240e+00)
bottom layer density [$Å^{-3}$]	0.01686	(-8.631e-04, 1.358e-04)
magnetization for bottom layer [μ_B/uc]	3.9314	(-1.474e+00, 6.851e-02)
Bottom layer roughness [Å]	24.7618	(-5.201e+00, 3.286e+00)
substrate roughness [Å]	29.3869	(-7.841e+00, 6.131e-01)
oxygen stoichiometry (top layer)	3.715282	(-4.312e-02, 1.106e-01)
oxygen stoichiometry (LSMO layer)	2.646298	(-7.136e-02, 1.468e-01)
oxygen stoichiometry (bottom layer)	2.712936	(-2.358e-01, 1.601e-01)
150 K		
magnetization for top layer [μ_B/uc]	0.5982	(-1.074e-01, 1.126e-01)
magnetization for LSMO layer [μ_B/uc]	1.0985	(-8.093e-02, 9.802e-02)
magnetization for bottom layer [μ_B/uc]	1.4439	(-2.891e-01, 2.672e-01)

C.2 Normalization

Magnetization

In the magnetization curve plotted in the thesis, the Bohr magneton μ_B is used instead of the unit (emu). Here the conversion from emu to μB is illustrated. The normalization to μ_B per Mn atom (μ_B/Mn) is given.

1 emu = 10^{-3} J · T^{-1}

1 $\mu_B = e\hbar/m_e$ = 9.27402×10^{-24} J · T^{-1}

=> 1 emu = 1.0783×10^{-20} μ_B

Since the thickness of the LSMO film can be measured by the XRR, the volume of the film is known. By XRD measurements, the lattice parameters can also be determined. The volume of unit cell is known as well. Therefore the total amount of Mn atoms within the LSMO film can be determined. In the end, the normalized magnetization (μ_B/Mn) is the total magnetic moment of the sample divided by the total number of Mn atoms.

Resistivity

In the thesis, the resistance of LSMO film is measured by four point method [138]. The equivalent circuit for a four point measurement is shown below:

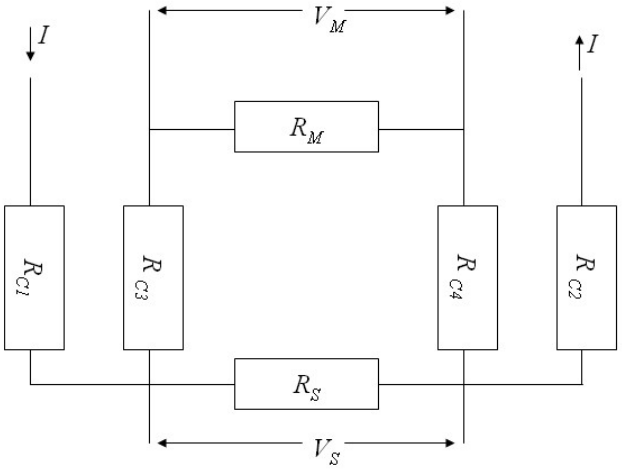

A current is passed through the two outer contacts while the voltage is measured between the two inner contacts. Here R_{C1} is the cable resistance and contact resistance of contact 1. Usually the contact resistance dominates over the cable resistance. R_S is the sample resistance and R_M is the equivalent resistance of the voltmeter. V_S is the voltage across the sample and V_M is the voltage measured by the voltmeter. When a current contact is placed on a thin conducting film with a uniform resistivity ρ and a current I is injected into this contact, the current density around the contact is:

$$\vec{j} = \frac{I}{2\pi t r}\hat{r}$$

Here t is the thickness of the film. A current I_{12} is injected into the surface at position r_1 while it is extracted from position r_2. The thin film approximation is valid if the distance between the contacts is much larger than the thickness of the film. The current density is given by:

$$\vec{j} = \frac{I_{12}}{2\pi t}\left(\frac{\vec{r}-\vec{r}_1}{|\vec{r}-\vec{r}_1|^2} - \frac{\vec{r}-\vec{r}_2}{|\vec{r}-\vec{r}_2|^2}\right)$$

The electric field is the resistivity ρ times the current density:

$$\vec{E} = \rho \cdot \vec{j} = \frac{\rho \cdot I_{12}}{2\pi t}\left(\frac{\vec{r}-\vec{r}_1}{|\vec{r}-\vec{r}_1|^2} - \frac{\vec{r}-\vec{r}_2}{|\vec{r}-\vec{r}_2|^2}\right)$$

The voltage between position r_3 and position r_4 on the surface is minus the integral of the electric field from one position to the other. The potential at r_4 measured with respect to the potential at r_3 is:

$$V_{43} = -\frac{\rho I}{2\pi t}\int_{r_3}^{r_4}\left(\frac{\vec{r}-\vec{r}_1}{|\vec{r}-\vec{r}_1|^2} - \frac{\vec{r}-\vec{r}_2}{|\vec{r}-\vec{r}_2|^2}\right)\cdot d\vec{r}$$

After performing the integration, the expression for the resistivity is:

$$\rho = -\frac{4\pi t V_{43}}{I_{12}}(l_{31} - l_{32} - l_{41} + l_{42})$$

where

$$l_{mn} = \ln((x_m - x_n)^2 + (y_m - y_n)^2)$$

List of Figures

List of Tables